Advancements in Kinetic Inductance Detector, Spectrometer, and Amplifier Technologies for Millimeter-Wave Astronomy

by

George Che

A Dissertation Presented in Partial Fulfillment
of the Requirements for the Degree
Doctor of Philosophy

Approved January 2018 by the
Graduate Supervisory Committee:

Philip Mauskopf, Chair
James Aberle
Christopher Groppi
Steven Semken
Georgios Trichopoulos

ARIZONA STATE UNIVERSITY

May 2018

ABSTRACT

The inductance of a conductor expresses its tendency to oppose a change in current flowing through it. For superconductors, in addition to the familiar magnetic inductance due to energy stored in the magnetic field generated by this current, kinetic inductance due to inertia of charge carriers is a significant and often dominant contribution to total inductance. Devices based on modifying the kinetic inductance of thin film superconductors have widespread application to millimeter-wave astronomy. Lithographically patterning such a film into a high quality factor resonator produces a high sensitivity photodetector known as a kinetic inductance detector (KID), which is sensitive to frequencies above the superconducting energy gap of the chosen material. Inherently multiplexable in the frequency domain and relatively simple to fabricate, KIDs pave the way to the large format focal plane array instruments necessary to conduct the next generation of cosmic microwave background (CMB), star formation, and galaxy evolution studies. In addition, non-linear kinetic inductance can be exploited to develop traveling wave kinetic inductance parametric amplifiers (TKIPs) based on superconducting delay lines to read out these instruments.

I present my contributions to both large and small scale collaborative efforts to develop KID arrays, spectrometers integrated with KIDs, and TKIPs. I optimize a dual polarization TiN KID absorber for the next generation Balloon-borne Large Aperture Submillimeter Telescope for Polarimetry, which is designed to investigate the role magnetic fields play in star formation. As part of an effort to demonstrate aluminum KIDs on sky for CMB polarimetry, I fabricate devices for three design variants. SuperSpec and WSpec are respectively the on-chip and waveguide implementations of a filter bank spectrometer concept designed for survey spectroscopy of high redshift galaxies. I provide a robust tool for characterizing the performance of all

SuperSpec devices and demonstrate basic functionality of the first WSpec prototype. As part of an effort to develop the first W-Band ($75 - 110$ GHz) TKIP, I construct a cryogenic waveguide feedthrough, which enhances the Astronomical Instrumentation Laboratory's capability to test W-Band devices in general. These efforts contribute to the continued maturation of these kinetic inductance technologies, which will usher in a new era of millimeter-wave astronomy.

DEDICATION

To my dear wife Cailin for your love and encouragement throughout this long journey.

ACKNOWLEDGMENTS

First and foremost, I would like to express my gratitude for my adviser Philip Mauskopf. When we first met in the basement of the Memorial Union back in August 2012, the first question you asked me was "What do you know about superconductivity?" to which I responded "not much..." Instead of being discouraged by my lack of knowledge about your primary area of research, you still accepted me as your first PhD student at ASU and gave me the opportunity to learn about and contribute to some of the most cutting edge research in superconducting devices for astronomical applications. Over the past six years, you have always encouraged me to be an independent thinker while at the same time never hesitating to share both your theoretical and practical knowledge, the depth of which has never ceased to amaze me.

In addition to my adviser, I am also sincerely grateful to every faculty member who has served on my comprehensive exam and supervisory committees. I especially want to recognize Chris Groppi for recruiting me to the School of Earth and Space Exploration (SESE), welcoming me into the community, and pointing me in the right direction whenever I felt lost. I am very grateful to know you not only as a mentor, but also a friend (and fellow lover of good food). Steven Semken, thank you for guiding me every step of the way to successfully complete my second project. I really appreciate your mentorship and confidence in me to conduct research in STEM education, a field that was completely new to me. Georgios Trichopoulos, Jim Aberle, Judd Bowman, and Nat Butler, you have all been essential to my growth as a scientist and engineer over the duration of my time at ASU. In addition, Jim, your exceptionally well-taught courses on microwave circuits and signal integrity greatly facilitated not only my graduate work, but also my job search.

I spent a substantial part of my time at ASU fabricating superconducting integrated circuits in the NanoFab facility on campus. These devices were the bread and butter of my work and I could not have made them without the exceptional ASU NanoFab staff. Kevin Hilgers, Kevin Nordquist, Todd Eller, Carrie Sinclair, and Scott Ageno, thank you for all of your time and effort training me on the tools and working with me every step of the way to develop and implement my fabrication processes.

One of the main reasons I chose ASU for graduate school was how welcoming everyone had been during recruitment weekend. The extraordinarily close-knit community of graduate students and research staff in SESE was essential to successfully navigating this challenging journey and resulted in many strong bonds of friendship. Caleb Wheeler, when I first started, never could I have imagined a better friend and professional role model. Your work ethic, attention to detail, and personal integrity will never cease to amaze me. Thank you for always being there for me, especially on the most important day of my life, when you officiated my wedding. Ed Schroeder, thank you for introducing me to the wonders of powerlifting, which definitely reduced my stress during these past few years. I also greatly enjoyed our many lively lunchtime discussions and adventures in the UK and Japan. I would consider Hamdi Mani to have almost superhuman knowledge of electronics. Thank you for always going the extra mile to help me out in the lab and displaying unbelievable patience. Sean Bryan, Kay Davis, Sam Gordon, Natalie Hinkle, Duho Kim, Becky Jackson, Boom Kittiwisit, Alex Miller, Tom Mozdzen, Gena Pilyavsky, Luke Probst, Alex Spacek, Amanda Truitt, Matt Underhill, and Kim Ward-Duong, thank you all for so many wonderful memories both in and out of ISTB4.

My graduate school experience was greatly enriched by summer internships at the Jet Propulsion Laboratory (JPL) and Air Force Research Laboratory (AFRL).

Matt Bradford, I am very grateful to have had the opportunity to spend a summer in Pasadena working on SuperSpec. Thank you Steve Hailey-Dunsheath for your continued support for my work on SuperSpec as it developed into a major part of my dissertation research over the past few years. Another member of the SuperSpec team I need to especially thank is Jordan Wheeler for providing a crucial improvement and addendum to my Python code. After JPL, I spent the following summer at AFRL at Kirtland Air Force Base in Albuquerque conducting non-academic research for the first time. Eachan Landreth and Julie Lawrance, thank you for broadening my horizons and introducing me to research in electromagnetic effects. Other than SuperSpec, the two major collaborations in which I participated were BLAST-TNG and the Columbia-led effort to develop dual-polarization CMB KIDs, both of which also constitute significant portions of this work. It was greatly rewarding to be a part of both of these teams.

Outside of the lab, my most meaningful experience at ASU was serving as director of Earth & Space Open House, SESE's monthly public outreach event. Successfully leading this program would not have been possible without the extraordinary efforts of Meg Hufford, Ric Alling, Stephanee Germaine, Karin Valentine, and my co-director of two years, Kelley Liebst. I would also like to thank former director Teresa Ashcraft for teaching me the ropes and all of the undergraduate, graduate, and staff who volunteered over the years.

I am immensely grateful to my high school physics teacher Clark Neily, undergraduate mentor Lyman Page, and undergraduate thesis adviser Jeremy Kasdin for guiding me through each stage of my scientific training before ASU. I also owe much thanks to Kevin Vasquez, Jon Surany, Ian Wong, Matt Cramer, and Dario Sava for endless amounts of camaraderie, inside jokes, and jolly good times. You guys have truly been

like brothers to me. One can never overstate the importance of family to personal success. I have not only my family by blood, but also my family be marriage to thank for so much love and support. While seldom nearby in person, my mathematically gifted and genuinely kindhearted brother, Charlie, has always been here for me as an academic and personal role model. I would like to extend my deepest gratitude to my parents Lucy and Yuhu for all their sacrifices to give me the opportunity to succeed. They have not only instilled in me a thirst for knowledge that has driven me throughout my academic career, but also taught me the importance of hard work, responsibility, and personal integrity, which has made me not just a good student, but a good person. I am also very thankful to have such a wonderful relationship with my mother and father-in-law, Terry and Jim Fogerty, who have been nothing but welcoming and supportive.

To my amazing wife Cailin, five years ago our common love of music brought us together. Since then, you have always stood by me throughout this long journey. You have accepted my long and often irregular work hours, months-long periods away for internships, and endless amounts of technical jargon that I was not always good about explaining. Words cannot express how grateful I am that you came into my life. I am also grateful for your insistence that I maintain at least a semi-regular sleep schedule and wear clothes that actually fit me. While making the final push to write this dissertation, life became an emotional roller coaster at times, but you were always there to bring the ride to a safe stop. I could not have completed this work without you and I am a better person because you are by my side. I love you with all my heart and look forward to spending the rest of my life with you.

TABLE OF CONTENTS

LIST OF TABLES

LIST OF FIGURES

Chapter 1

INTRODUCTION

As taught in any introductory electricity and magnetism course, the inductance of a conductor expresses its tendency to oppose a change in the current flowing through it. This is due to energy stored in the magnetic field generated by this current and the phenomenon is governed by Faraday's law of induction. For normal metals, this effectively tells the whole story, but for superconductors, another source of inductance is significant and often dominant due to the high mobility of superconducting charge carriers. This is kinetic inductance, which is due to the inertia of the charge carriers themselves. For normal metals, kinetic inductance exists, but is generally a negligible contribution to the total inductance. Kinetic inductance in superconductors is the phenomenon that underlies all technologies to be discussed in this dissertation.

1.1 Early History of Kinetic Inductance Detectors

When a thin superconducting film is lithographically patterned into a high quality factor resonator, photons incident on its inductive section with energy greater than the film material's superconducting gap energy will break Cooper pairs, which are superconducting electrons bound together by the electron-phonon interaction. The gap energy is given by $2\Delta \approx 3.5 k_B T_c$, where T_c is the superconducting transition temperature. Optical pair-breaking generates quasiparticles, which behave like electrons in a normal metal, thus modifying both the surface kinetic inductance and resistance of the film. This change in surface impedance manifests as a simultaneous shift in

resonant frequency and degradation of quality factor. Due to the capability of such resonators to achieve extremely high internal quality factors ($> 10^6$), they are highly suitable to use as extremely sensitive photodetectors for millimeter-wave astronomy, which we can broadly define as astronomical studies at wavelengths between 3 mm (100 GHz) and 300 μm (1 THz). Specific observation bands are defined by selecting an appropriate superconductor and filtering scheme. Known as kinetic inductance detectors (KIDs), these photodetectors were first demonstrated in the laboratory in 2003 (Day et al. 2003) and on sky in 2008 (Schlaerth et al. 2008). Since this first on-sky demonstration, KID technology has matured considerably (Zmuidzinas 2012; Mauskopf 2017) and the astronomical community is now on the cusp of deploying multiple large format KID array instruments with focal planes populated by thousands to eventually tens of thousands of detectors. Observing sources ranging from the cosmic microwave background (CMB) to high redshift galaxies to molecular clouds using these powerful instruments will undoubtedly usher in a new era of millimeter-wave astronomy. This dissertation presents our contributions to both large and small-scale efforts to develop KID array instruments, filter bank spectrometers integrated with KIDs, and kinetic inductance parametric amplifiers.

Even before the first laboratory demonstration of KIDs, state-of-the-art bolometers were already approaching photon-noise limited performance, defined as exhibiting internal noise comparable to or less than that arising from the randomness in the arrival of incident photons (Day et al. 2003). Therefore, further improvement of instrument sensitivity requires increasing the number of detectors. The instrument fielding the largest bolometer array is the Submillimetre Common-User Bolometer Array 2 (SCUBA-2), which simultaneously observes in the 450 μm and 850 μm atmospheric windows with a total of 10,000 transition edge sensors (TESs) (Holland et

al. 2013). This is close to the upper limit of array size for TESs because the SCUBA-2 detectors are multiplexed using time-domain multiplexing, which allows 40 detectors to be read out with a single readout set. As high quality factor resonators, KIDs naturally enable frequency domain multiplexing with multiplexing ratios estimated to be as high as $\sim 10^3$. High multiplexing ratios combined with a relatively simple fabrication process make KIDs a suitable detector for many future millimeter-wave astronomical instruments.

1.2 Interstellar Magnetic Field and Cosmic Microwave Background Polarimetry

To fully understand star formation, we need to develop a theory that includes all processes governing star formation rate in interstellar clouds. Observed star formation rates are up to an order of magnitude lower than what is predicted by gravitational collapse of interstellar clouds alone. The mechanism that supports these clouds against collapse is still poorly understood. The two prevailing theories for this mechanism are turbulence and interstellar magnetic fields (Elmegreen and Scalo 2004; McKee and Ostriker 2007). To determine the relative importance of these two mechanisms, we need to produce detailed maps of velocity dispersions and magnetic fields within clouds. Mapping magnetic field strength and orientation inside star forming molecular clouds requires millimeter-wave polarimetry to trace linearly-polarized thermal emission from dust grains aligned to the direction of local magnetic fields.

Employing a 1.8 m primary mirror that directs light onto 280 bolometers in three arrays operating in bands centered on 250 μm, 350 μm, and 500 μm, the Balloon-borne Large Aperture Submillimeter Telescope (BLAST) made many groundbreaking observations of molecular clouds (Devlin et al. 2009; Netterfield et al. 2009). Inserting

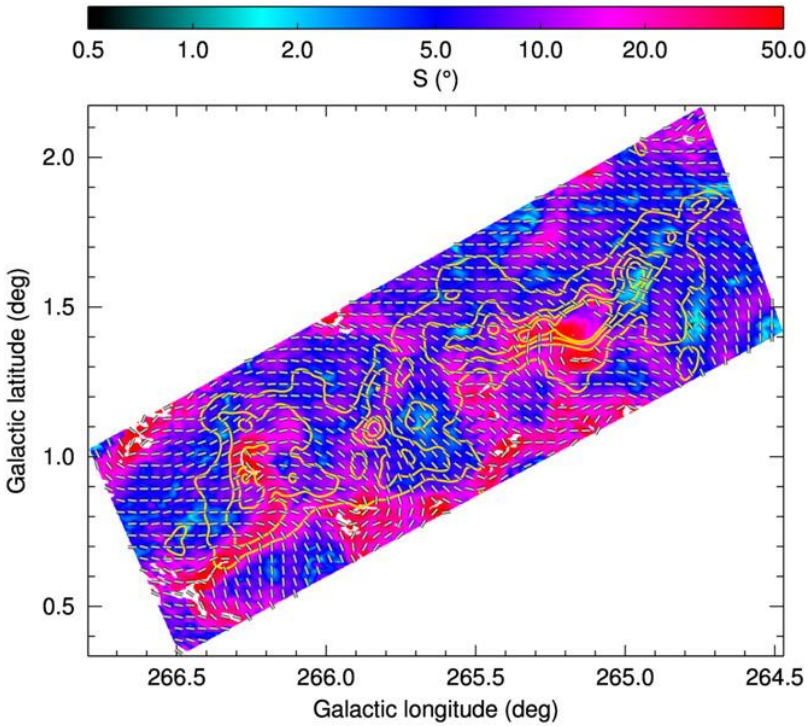

Figure 1: Map of magnetic field polarization angle S in degrees in Vela C star forming region produced by BLASTPol observations at 500 μm. Superimposed line segments represent magnetic field orientation projected into plane of sky derived from observations. Figure from (Fissel et al. 2015).

polarizing grids immediately before its horn apertures and incorporating an achromatic half wave plate (AHWP) in its optics upgraded BLAST to the polarimeter BLASTPol, which produced some of the first degree-scale polarization maps of star forming regions such as the map of Vela C shown in Fig. 1 (Fissel et al. 2015). Other millimeter-wave polarimeters provide mapping capability over either large or small areas of the sky. Planck provides capability to produce maps of the entire sky, but at coarse resolution with FWHM $\sim 5'$ (Lamarre et al. 2003). Meanwhile, the Atacama Large Millimeter Array (ALMA) provides fine resolution with FWHM $< 0.01''$, but can only feasibly map areas of the sky on the order of $\sim 10''$ in size. Therefore, BLASTPol

bridges the technological gap between between large-scale low-resolution and small-scale high-resolution mapping capability by providing $30''$ resolution at 250 μm to map areas of the sky $\sim 1^\circ$ in size. Serving as a pathfinder for balloon-borne KID arrays, the next generation BLASTPol (BLAST-TNG) improves upon BLASTPol by increasing the size of the primary to 2.5 m and replacing the 280 bolometers with ~ 3000 KIDs, resulting in better resolution, four times the field of view, and up to 16 times the mapping speed (Galitzki et al. 2014; Dober et al. 2016). We describe our contribution to detector development for BLAST-TNG in Section 3.1. Combining BLAST-TNG with Planck and ALMA enable unprecedented capability to study the role of magnetic fields in star formation. In addition, using BLAST-TNG to observe areas of the sky targeted for cosmic microwave background (CMB) polarimetry helps characterize galactic foregrounds, which are significant sources of contamination for these experiments.

The CMB is a nearly isotropic thermal image of the universe 380,000 years after the Big Bang. Measurements of intensity and polarization anisotropies in the CMB have played an essential role in developing and constraining the Lambda Cold Dark Matter (ΛCDM) cosmological model, which entails a 13.8 Gyr-old flat universe that is composed primarily of dark matter ($\sim 24\%$) and dark energy ($\sim 70\%$) (Frieman, Turner, and Huterer 2008). Further studies of the CMB are focused on detecting the faint B-mode polarization anisotropy from primordial gravitational waves, which would corroborate the theory of inflation (Guth, Kaiser, and Nomura 2014). A plethora of ground-based and balloon-borne instruments employing thousands of TESs (Niemack et al. 2010; Bryan 2014; Essinger-Hileman 2011; Carlstrom et al. 2011; Grayson et al. 2016) have already been deployed for such studies with the second iteration of the Background Imaging of Cosmic Extragalactic Polarization experiment

(BICEP2) yielding a detection of B-modes that was originally thought to be from gravitational waves (Ade et al. 2014), but ultimately attributed to dust emission (Cowen 2015). These instruments approach the upper limit for TES array size due to readout complexity, so a different detector is needed to further increase array size and thus sensitivity since the individual detectors are already photon-noise limited. Inherently multiplexable in the frequency domain with high multiplexing ratios, KIDs provide a promising candidate for the future of CMB polarimetry. We present our contribution to detector fabrication for the inaugural effort to demonstrate dual-polarization KID arrays operating in the 150 GHz band on-sky for ground-based CMB studies (H. McCarrick et al. 2017) in Section 3.2.

1.3 Galactic and Extragalactic Survey Spectroscopy

The previous section describes instruments employing large arrays of KIDs to observe continuum emission over bandwidths defined by filters preceding the focal plane. The millimeter-wave regime also contains a wealth of important spectral information. Fig. 2 provides an overview of the spectral content for a typical star forming cloud within our own galaxy superimposed on the CMB spectrum. Since such a cloud is nearby, this is a rest frame depiction. Optical and ultraviolet light from stars heat the interstellar gas within these clouds to $10 - 100$ K, which excites numerous atomic fine-structure and molecular rotational lines. These lines provide powerful probes of the star formation process in both nearby and distant galaxies, for which the lines are redshifted to longer wavelengths. A current topic of interest in millimeter-wave astronomy is the birth and subsequent evolution of galaxies from the Epoch of Reionization (EoR) ($6 \lesssim z \lesssim 20$) (Loeb and Barkana 2001; Zaroubi 2012) to

today. Broadband spectral surveys over large areas of the sky at these wavelengths provide the means to both investigate a statistically large sample of individual galaxies and perform wide-field tomographic intensity mapping. SuperSpec (Kovács et al. 2012; Barry et al. 2012; Hailey-Dunsheath et al. 2016; Wheeler et al. 2016) is a novel on-chip spectrometer technology that integrates a superconducting transmission line filterbank with hundreds of KIDs on a single chip only ~ 1 cm^2 in size. Its compactness, $\mathcal{R} \sim 500$ spectral resolving power, $\sim 70\%$ instantaneous bandwidth, and extremely sensitive detectors enable construction of powerful focal plane spectrometer arrays optimized for the aforementioned survey studies. We present a microwave network model we developed to serve as a general purpose tool for characterizing all SuperSpec devices and initial prototyping for WSpec, a rectangular waveguide implementation of the same filter bank concept in Chapter 4.

1.4 Signal Amplification

All instruments employing KIDs require amplification of microwave probe tones for readout. In addition, some millimeter-wave instruments require front end amplification of signals from the sky before encountering their detectors. The figures of merit for an amplifier are gain, bandwidth, dynamic range, and noise performance. An ideal amplifier produces high, uniform gain over the entire observation band while exhibiting both high dynamic range and quantum-limited noise performance. Solid state low noise amplifiers represent the current state-of-the-art (Weinreb et al. 2009), but the traveling wave kinetic inductance parametric amplifier (TKIP) is an emerging technology that offers both wide instantaneous bandwidth and quantum-limited noise performance. Parametric amplifiers produce gain through four wave or three wave

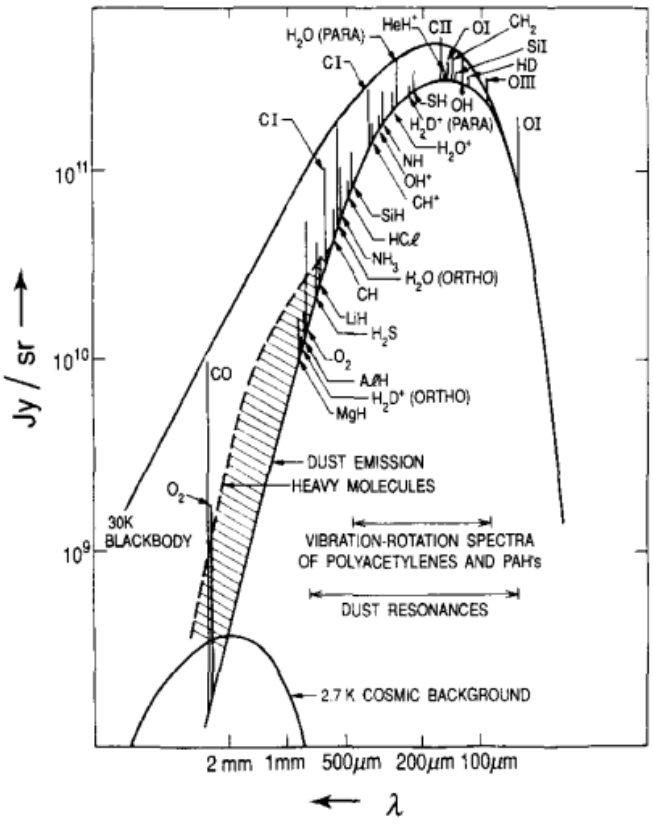

Figure 2: Schematic representation of spectral content contained in 2 mm − 100 μm band for typical star forming cloud within our galaxy superimposed on CMB spectrum. Figure from (Phillips and Keene 1992).

mixing (FWM/TWM) during which a strong pump mixes with a weak signal through a non-linear medium. For millimeter-wave applications, TKIPs exploit the non-linear kinetic inductance of superconductors for FWM/TWM. Realized in superconducting transmission lines, which are inherently wideband, TKIPs achieve a maximum gain that depends on two parameters: I_*, the characteristic current parameter that sets the scale for non-linearity and $\Delta\phi_{\max}$ and the maximum non-linear phase shift that can be induced by applying DC bias to a STL (Ho Eom, Day, LeDuc, et al. 2012). (Bockstiegel et al. 2014; Adamyan et al. 2016; Vissers et al. 2016; Chaudhuri et al. 2017)

have investigated TKIPs operating in the 10 GHz range that achieve ~ 15 dB gain over ~ 4 GHz of bandwidth and noise temperature as low as 0.5 ± 0.3 K, which approaches the quantum limit. We present the design, fabrication, and characterization of a dual-purpose phase shifter and TKIP circuit operating in W-Band in Chapter 5.

Chapter 2

KINETIC INDUCTANCE DETECTORS

This chapter is a review of superconductivity, kinetic inductance, and the operation of kinetic inductance detectors from both a device physics and microwave circuit perspective. We provide an overview of the methods to characterize detector response, sensitivity, and anomalous behavior not explained by established superconductivity theory. We finish with a brief summary of methods to efficiently couple incident radiation from telescope optics onto the detectors in the focal plane.

2.1 Superconductivity and Kinetic Inductance

2.1.1 Fundamentals of Superconductor Electrodynamics

The two-fluid model intuitively describes the behavior of a superconductor in a time-varying electromagnetic field. The charge carriers in a superconductor can be divided into two groups: superconducting electrons, which conduct current without dissipation, and quasiparticles, which behave like electrons in a normal metal. Therefore, there are two paths through which current is conducted in a superconductor. According to Bardeen-Cooper-Schrieffer (BCS) theory, superconducting electrons are bound together through electron-phonon interaction into boson-like Cooper pairs (Bardeen, Cooper, and Schrieffer 1957). Defining the density of Cooper pairs and quasiparticles to be n_s and n_{qp}, respectively, the total density of charge carriers $n = n_s + n_{qp}$ is conserved, but the relative proportions of these two fluids depend on temperature. At

the critical temperature of the superconductor $T = T_c$, there is no superconducting fluid, so $n = n_{qp}$ and $n_s = 0$. At $T = 0$, all charge carriers are superconducting, so $n = n_s$ and $n_{qp} = 0$. As we decrease the temperature from T_c to 0, n_s gradually increases from 0 to n and vice versa for n_{qp}.

The London equations provide the simplest description of fundamental electromagnetic properties of superconductors. We make the assumptions that n_s is uniform throughout the superconductor and unchanged by the electric and magnetic fields to derive relationships between current, electric field, and magnetic field. The equation of motion for Cooper pairs in an electric field $\mathbf{E}$ is

$$n_s m_e \frac{d\mathbf{v_s}}{dt} = -n_s e\mathbf{E}, \tag{2.1}$$

where m_e and e are the electron mass and charge, respectively, and $\mathbf{v_s}$ is the velocity of the superconducting fluid. Introducing the superconducting current density $\mathbf{j_s} = -n_s e\mathbf{v_s}$, Eq. 2.1 can be written as

$$\mathbf{E} = \frac{m_e}{n_s e^2}\frac{d\mathbf{j_s}}{dt}, \tag{2.2}$$

which is known as the first London equation. We obtain the second London equation by substituting Maxwell's equations

$$\nabla \times \mathbf{E} = -\mu_0 \frac{\partial \mathbf{H}}{\partial t} \tag{2.3}$$

$$\nabla \times \mathbf{H} = \mathbf{j_s} \tag{2.4}$$

into Eq. 2.2, which yields

$$\nabla^2 \mathbf{H} = \frac{\mathbf{H}}{\lambda_L^2}, \tag{2.5}$$

where

$$\lambda_L = \sqrt{\frac{m_e}{\mu_0 n_s e^2}} \tag{2.6}$$

is the London penetration depth. Eq. 2.5 implies that a magnetic field decays exponentially inside a superconductor with a characteristic decay length of λ_L, a fundamental phenomenon of superconductors known as the Meissner effect. Since n_s is temperature-dependent, λ_L is also temperature-dependent and an empirical formula for this temperature dependence is given by

$$\lambda_L(T) = \frac{\lambda_{L,0}}{\sqrt{1-(T/T_c)^4}}, \tag{2.7}$$

where $\lambda_{L,0}$ is the penetration depth at $T = 0$.

We can write the second London equation in a different form by introducing the vector potential $\mathbf{A}(\mathbf{r})$ and using the London gauge, namely

$$\begin{aligned} \nabla \cdot \mathbf{A} &= 0 \\ \mathbf{A} \cdot \mathbf{n} &= 0, \end{aligned} \tag{2.8}$$

where $\mathbf{n}$ is the unit vector normal to the surface of the superconductor. Since $\mathbf{H} = \nabla \times \mathbf{A}/\mu_0$, substituting Eq. 2.4 into Eq. 2.5 yields

$$\mathbf{j_s}(\mathbf{r}) = -\frac{1}{\mu_0 \lambda_L^2}\mathbf{A}(\mathbf{r}), \tag{2.9}$$

where we have explicitly expressed dependence on position. According to Eq. 2.9, the superconducting current density at each position $\mathbf{r}$ depends only on the vector potential at the same position. Therefore, the London equations are only valid when the vector potential does not vary appreciable over the characteristic size of a Cooper pair, a distance known as the coherence length. (Pippard 1953) developed a non-local generalization of Eq. 2.9, namely

$$\mathbf{j_s}(\mathbf{r}) = -\frac{3}{4\pi\mu_0\lambda_L^2\xi_0}\iiint \frac{\mathbf{R}\cdot\mathbf{A}(\mathbf{r}')}{R^4}\mathbf{R}e^{-R/\xi_0}d^3r', \tag{2.10}$$

which takes into account the fact that $\mathbf{j_s}$ depends on $\mathbf{E}(\mathbf{r}')$ throughout a spherical volume of radius ℓ centered around $\mathbf{r}$, $\mathbf{R} = \mathbf{r} - \mathbf{r}'$, and ξ is the coherence length in the

presence of impurities, which is related to that for a pure material ξ_0 by

$$\frac{1}{\xi} = \frac{1}{\xi_0} + \frac{1}{\ell}. \tag{2.11}$$

From uncertainty principle arguments, the pure material coherence length is

$$\xi_0 = \alpha \frac{\hbar v_F}{k_B T_c} \tag{2.12}$$

where v_F is the Fermi velocity, k_B is Boltzmann's constant, and α is a constant of order unity. Using Eq. 2.10, Pippard fit experimental data for tin and aluminum to obtain $\alpha = 0.15$, which was corroborated by BCS theory. When $\xi \ll \lambda_L$, we are in the local limit, and Eq. 2.10 becomes

$$\mathbf{j_s} = -\frac{1}{\mu_0 \lambda_{\text{eff}}} \mathbf{A}, \tag{2.13}$$

which has the same form as Eq. 2.9, but the penetration depth is now

$$\lambda_{\text{eff}} = \lambda_L \left(1 + \frac{\xi_0}{\ell}\right)^{1/2}. \tag{2.14}$$

For $\xi \gg \lambda_L$, we are in the anomalous limit, and the penetration depth becomes

$$\lambda_{\text{eff}} = \left[\frac{\sqrt{3}\lambda_L^2 \xi_0}{2\pi}\right]^2, \tag{2.15}$$

as derived in (Faber and Pippard 1955)

2.1.2 Two Types of Inductance

We derive expressions for the magnetic and kinetic inductance of a perfectly conducting wire of length l and cross sectional area A. The inductance in this wire is the coefficient of proportionality between the rate of change in current through and voltage across the perfect conductor. Fundamentally, inductance is due to the

fact that current cannot respond instantaneously to an applied voltage even if the resistance is zero due to energy stored in the magnetic field and inertia of the charge carriers. How the current responds is described by the conductivity of the material. The equation of motion for a charge carrier in a material with finite conductivity is

$$m_e \frac{d\mathbf{v}}{dt} = e\mathbf{E} - \frac{m_e \mathbf{v}}{\tau} \tag{2.16}$$

where $\mathbf{v}$ is the velocity of the charge carrier, $\mathbf{E}$ is the electric field due to the applied voltage, and τ is the characteristic scattering time. The second term in Eq. 2.16 describes damping due to the scattering of charge carriers inside the material. The current density is given by $\mathbf{j} = en_e v$, where n_e is the carrier density. Combining this definition of current density with Ohm's law in the form of $\mathbf{j} = \sigma_0 \mathbf{E}$ and Eq. 2.16, the DC conductivity is $\sigma_0 = e^2 n_e \tau / m_e$. Also according to Eq. 2.16, the linear response to an AC field of the form $\mathbf{E} = Ee^{j\omega t}$ is given by the complex Drude conductivity

$$\sigma_d(\omega) = \sigma_{d,\mathrm{re}}(\omega) - j\sigma_{d,\mathrm{im}}(\omega) = \frac{\sigma_0}{1 + j\omega\tau}, \tag{2.17}$$

where the real and imaginary parts are

$$\sigma_{d,\mathrm{re}}(\omega) = \frac{\sigma_0}{1 + \omega^2\tau^2} \tag{2.18a}$$

$$\sigma_{d,\mathrm{im}}(\omega) = \frac{\sigma_0 \omega\tau}{1 + \omega^2\tau^2}. \tag{2.18b}$$

To account for the effect of energy stored in the magnetic field, we relate energy to current at the microscopic scale. Applying a voltage V to our perfectly conducting wire results in a force $F = eV/l$ on each charge carrier. Therefore, the rate of change of energy for a single charge carrier is

$$P = \frac{dW_e}{dt} = Fv = \frac{eVv}{l}. \tag{2.19}$$

The total number of charge carriers in the wire is $N = n_e A l$, so the total power is

$$P_{tot} = \frac{dW}{dt} = NP = n_e AeVv = IV, \tag{2.20}$$

where $I = jA = en_e vA$ is the current in the wire and we have arrived at the familiar relationship between power, current, and voltage. Ampère's law $\nabla \times \mathbf{H} = \mathbf{j}$ tells us that every current is associated with a magnetic field with energy density $w_m = \mu H^2/2$, where μ is the permeability of the material. The total magnetic energy stored in a volume $\mathcal{V}$ is

$$W_m = \frac{\mu}{2} \int H^2 d\mathcal{V} = \frac{1}{2} L_m I^2, \tag{2.21}$$

where L_m is the magnetic inductance. L_m is interchangeably referred to as the geometric inductance because it depends solely on the conductor's geometry and not on charge carrier density. Substituting Eq. 2.21 into Eq. 2.20, we obtain

$$V = L_m \frac{dI}{dt}, \tag{2.22}$$

which is the familiar definition of inductance.

A change in current is also opposed by the inertia of the charge carriers, which is described by the kinetic energy. The analogous equation to Eq. 2.21 is

$$W_k = \int \frac{n_e m_e v^2}{2} d\mathcal{V} = \frac{1}{2} L_k I^2, \tag{2.23}$$

where L_k is the kinetic inductance. For our wire, Eq. 2.23 becomes

$$\frac{n_e m_e v^2}{2} Al = \frac{1}{2} L_k \left(e n_e v A\right)^2, \tag{2.24}$$

so the kinetic inductance per unit length is

$$\mathcal{L}_k = \frac{m_e}{e^2 n_e A}. \tag{2.25}$$

The imaginary part of the Drude conductivity in Eq. 2.18b can be understood as a consequence of kinetic inductance. For normal metals at low frequencies, $\omega\tau \ll 1$, so the imaginary part of σ_d and thus kinetic inductance is negligible. However, for superconductors, $\tau \to \infty$, so kinetic inductance becomes appreciable and in many

cases dominant. The kinetic inductance of superconducting films is the phenomenon that underlies every technology we describe in this dissertation.

2.2 Physics of Superconducting Films

2.2.1 Mattis-Bardeen Theory

Superconductors have a temperature dependent energy gap $2\Delta(T)$, which defines the binding energy of a Cooper pair. For $T \ll T_c$, $2\Delta_0 \approx 3.5 k_B T_c$. The Mattis-Bardeen equations (Mattis and Bardeen 1958),

$$\frac{\sigma_1(\omega)}{\sigma_n} = \frac{2}{\hbar\omega}\int_{\Delta}^{\infty} [f(E) - f(E+\hbar\omega)]\, g(E,\hbar\omega)\, dE + \frac{1}{\hbar\omega}\int_{\Delta-\hbar\omega}^{-\Delta} [1-2f(E+\hbar\omega)]\, g(E,\hbar\omega)\, dE, \quad (2.26)$$

where

$$g(E,\hbar\omega) = \frac{E^2+\Delta^2+\hbar\omega E}{\sqrt{E^2-\Delta^2}\sqrt{(E+\hbar\omega)^2-\Delta^2}} \quad (2.27)$$

and

$$\frac{\sigma_2(\omega)}{\sigma_n} = \frac{1}{\hbar\omega}\int_{\max(\Delta-\hbar\omega,-\Delta)}^{-\Delta} [1-2f(E+\hbar\omega)]\, \frac{E^2+\Delta^2+\hbar\omega E}{\sqrt{\Delta^2-E^2}\sqrt{(E+\hbar\omega)^2-\Delta^2}} dE, \quad (2.28)$$

relate the complex conductivity of the superconductor $\sigma(\omega) = \sigma_1(\omega) - j\sigma_2(\omega)$ to the normal state conductivity σ_n. $f(E)$ is the distribution function for quasiparticles and in thermal equilibrium, $f(E) = 1/\left(1+e^{E/k_BT}\right)$, the Fermi-Dirac distribution.

As mentioned in Section 2.1.1, the quasiparticle density decreases with decreasing temperature below T_c. This dependence is described by

$$n_{qp}(T) = 4\int_{\Delta}^{\infty} \frac{N(E)\,E}{\sqrt{E^2-\Delta^2}} f(E)\, dE, \quad (2.29)$$

where $N(E)$ is the superconductor's single-spin density of states. At $T = T_c$, all charge carriers are quasiparticles and Eq. 2.29 becomes

$$n_{qp}(T = T_c) = 4N_0 \int_0^\infty \frac{dE}{1 + e^{E/k_B T_c}} = 4N_0 k_B T_c \ln(2), \tag{2.30}$$

which represents total number of charge carriers available to form Cooper pairs. $N_0 = N(E = 0)$ is the single spin density of states at the Fermi energy. For $k_B T \ll \Delta$ and $\hbar\omega \ll \Delta$, Eq. 2.29 can be approximated by

$$n_{qp}(T) \simeq 2N_0 \sqrt{2\pi k_B T \Delta_0}\, e^{-\Delta/k_B T}. \tag{2.31}$$

We relate the quasiparticle density to the Mattis-Bardeen conductivity using the approximations provided in (Gao 2008), namely

$$\frac{\sigma_1(n_{qp}, T)}{\sigma_n} = \frac{2\Delta_0}{\hbar\omega} \frac{n_{qp}}{N_0\sqrt{2\pi k_B T \Delta_0}} \sinh(\chi) K_0(\chi) \tag{2.32a}$$

$$\frac{\sigma_2(n_{qp}, T)}{\sigma_n} = \frac{\pi\Delta_0}{\hbar\omega} \left[1 - \frac{n_{qp}}{2N_0\Delta_0} \left(1 + \sqrt{\frac{2\Delta_0}{\pi k_B T}} e^{-\chi} I_0(\chi)\right)\right] \tag{2.32b}$$

$$\frac{d\sigma_1}{dn_{qp}} = \frac{\sigma_n}{N_0\hbar\omega} \sqrt{\frac{2\Delta_0}{\pi k_B T}} \sinh(\chi) K_0(\chi) \tag{2.32c}$$

$$\frac{d\sigma_2}{dn_{qp}} = -\frac{\pi\sigma_n}{2N_0\hbar\omega} \left(1 + \sqrt{\frac{2\Delta_0}{\pi k_B T}} e^{-\chi} I_0(\chi)\right) \tag{2.32d}$$

where I_0 and J_0 are the zeroth order modified Bessel functions of the first and second kind, respectively, $\chi = \hbar\omega/2k_B T$, and final two equations are the derivatives of σ_1 and σ_2 with respect to n_{qp}. It is clear from Eqs. 2.32a and 2.32b that a change in quasiparticle density changes a superconductor's response to an incident signal. In the superconducting state, Cooper pairs can be broken to produce quasiparticles either thermally or through an external pair-breaking event. As shown in (Gao 2008), these two mechanisms that change n_{qp} have an equivalent effect on the complex conductivity for $T < 500$ mK, so Eqs. 2.32a-2.32d are valid in both cases under the aforementioned

conditions. Pair-breaking due to absorption of photons with energy $\hbar\omega > 2\Delta$ is the fundamental detection mechanism for kinetic inductance detectors.

2.2.2 Surface Impedance

We usually cannot directly access the complex conductivity of a superconductor through experiment, so we probe its surface impedance $Z_s = R_s + jX_s$ instead. For a superconducting film with thickness $t \gg \lambda_{\text{eff}}$ in the local limit, we relate surface impedance to conductivity with

$$Z_s(\omega, T) = \sqrt{\frac{j\omega\mu_0}{\sigma(\omega, T)}} = \frac{Z_s(\omega, 0)}{\sqrt{1 + \dfrac{j\delta\sigma(\omega, T)}{\sigma_2(\omega, 0)}}}, \tag{2.33}$$

where $\delta\sigma(\omega, 0) = \sigma(\omega, T) - \sigma(\omega, 0) = \sigma_1(\omega, T) - j\delta\sigma_2(\omega, T)$ and

$$Z_s(\omega, 0) = j\omega\mu_0\lambda_{\text{eff}}. \tag{2.34}$$

We can now write the effective penetration depth in terms of the normal state conductivity σ_n and energy gap δ as

$$\lambda_{\text{eff}} = \sqrt{\frac{\hbar}{\pi\Delta\mu_0\sigma_n}}. \tag{2.35}$$

For a thin film with $t \ll \lambda_{\text{eff}}$, the current density becomes approximately uniform throughout the film and the expression for surface impedance is

$$Z_s(\omega, T) = \frac{j\mu_0\omega\lambda_{\text{thin}}}{1 + \dfrac{j\delta\sigma(\omega, T)}{\sigma_2(\omega, 0)}}, \tag{2.36}$$

where $\lambda_{\text{thin}} = \lambda_{\text{eff}}/t$. For most of the Al and TiN devices we describe in this dissertation, films are thin enough such that $t \ll \ell$, where ℓ is the mean free path. Under this

additional condition, (Gao 2008) shows that the surface impedance becomes

$$Z_s = \frac{1}{\sigma t} = \frac{1}{(\sigma_1 - j\sigma_2)\, t} \approx \frac{1}{t\sigma_2^2} (\sigma_1 + j\sigma_2), \tag{2.37}$$

where we make the approximation by assuming $\sigma_2 \gg \sigma_1$. Therefore, the surface resistance and reactance are $R_s = \sigma_1/\sigma_2^2 t$ and $X_s = \omega L_k = 1/\sigma_2 t$, respectively. For $T \ll T_c$, we use Eq. 2.34 to obtain

$$L_k = \frac{1}{\omega \sigma_2 t} = \mu_0 \lambda_{\text{thin}}. \tag{2.38}$$

From Eq. 2.37, we can relate a change in surface impedance to a change in conductivity by

$$\frac{\delta Z_s(\omega, T)}{Z_s(\omega, 0)} \approx -\gamma \frac{\delta\sigma(\omega, T)}{\sigma(\omega, 0)}, \tag{2.39}$$

where $\delta Z_s(\omega, T) = Z_s(\omega, T) - Z_s(\omega, 0)$ and $\gamma = 1$ for thin films (Zmuidzinas 2012). From Eq. 2.39, changes in surface resistance and reactance are given by

$$\frac{\delta R_s}{X_s(\omega, 0)} = \frac{\delta\sigma_1}{\sigma_2(\omega, 0)} \tag{2.40a}$$

$$\frac{\delta X_s}{X_s(\omega, 0)} = -\frac{\delta\sigma_2}{\sigma_2(\omega, 0)}. \tag{2.40b}$$

The final step is to determine the response of the surface impedance to a change in quasiparticle density. Combining Eqs. 2.32c and 2.32d with Eqs. 2.40a and 2.40b, we obtain

$$\frac{\delta R_s}{X_s(\omega, 0)} = \frac{S_1(\omega)}{2\Delta_0 N_0} \delta n_{qp} \tag{2.41a}$$

$$\frac{\delta X_s}{X_s(\omega, 0)} = \frac{S_2(\omega)}{2\Delta_0 N_0} \delta n_{qp} \tag{2.41b}$$

where

$$S_1(\omega) = \frac{2}{\pi} \sqrt{\frac{2\Delta_0}{\pi k_B T}} \sinh(\chi) \tag{2.42a}$$

$$S_2(\omega) = 1 + \sqrt{\frac{2\Delta_0}{\pi k_B T}} e^{-\chi} I_0(\chi) \tag{2.42b}$$

when $\hbar\omega \ll \Delta_0$ and $k_B T \ll \Delta_0$. The ratio

$$\beta(\omega) = \frac{S_2(\omega)}{S_1(\omega)} = \frac{|\delta X_s|}{\delta R_s} = \frac{\delta\sigma_2}{\delta\sigma_1} \tag{2.43}$$

reveals the relative strength of these two responses. Kinetic inductance detectors are microresonators lithographically-patterned in thin superconducting film. Quasiparticle generation due absorption of photons with energy $\hbar\omega > 2\Delta$ changes the film's surface impedance according to Eqs. 2.41a and 2.41b. These resonators are sensitive photodetectors because changes in Z_s can be measured with extremely high sensitivity.

2.3 Kinetic Inductance Detector Operation and Performance

2.3.1 Basic Principle

Now that we have reviewed the physics of superconducting films, we formally introduce the detection mechanism of the kinetic inductance detector (KID). We limit our discussion to lumped element KIDs, which were first demonstrated in (Doyle 2008). As shown in Fig. 3a, we model this type of KID as a parallel resonator consisting of an inductor $L = L_m + L_k$ and capacitor C with a resistor R, which represents dissipation, in series with the inductor. The resonator is capacitively coupled to a microwave feedline with characteristic impedance Z_0 through a coupling capacitor C_c, which can either be an interdigital capacitor as shown in Fig. 3b or just a gap. The closeup in Fig. 3a illustrates the two-fluid model, explicitly showing the two paths through which current flows in a superconductor. Current can either be conducted by quasiparticles, which behave like normal electrons with dissipation, or by Cooper pairs with no dissipation. These two current paths are represented by a resistor and inductor, respectively. A typical KID pixel is shown in Fig. 3b. The resonant circuit

is implemented as an interdigital capacitor and inductive meander lithographically patterned in a thin superconducting film with either coplanar waveguide or microstrip geometry. In the absence of pair-breaking, its resonant frequency and internal quality factor are

$$\omega_r = 2\pi f_r = \frac{1}{\sqrt{L\,(C + C_c)}} \tag{2.44}$$

and

$$Q_i = \frac{\omega_r L}{R}, \tag{2.45}$$

respectively. Incident Photons with energy $\hbar\omega > 2\Delta$ will break Cooper pairs in the inductive meander portion of the circuit, simultaneously altering both n_s and n_{qp}. The change in density of the two conducting fluids changes both the reactive and resistive parts of the superconducting film's surface impedance, which manifests in the circuit as a shift in resonant frequency δf_r and reduction in quality factor as shown in Fig. 4. To measure KID response to optical loading, we send a microwave probe tone tuned to the KID's resonant frequency down the feedline and observe changes in the amplitude and phase of S_{21} as photons are absorbed by the inductive meander. KIDs have inherently high multiplexing ratios, which enable large focal plane arrays to improve instrument sensitivity. Fig. 3c shows a small array of 20 KIDs that share a common feedline. These KIDs are simultaneously read out by sending a comb of probe tones with frequencies corresponding to their resonant frequencies. A single feedline can read out up to 10^3 KIDs.

The fundamental limit to the sensitivity of a KID is generation-recombination noise due to random pair-breaking by thermal phonons. From Eq. 2.31, we see that generation-recombination noise is reduced by a factor of $e^{-\Delta/k_B T}$ at low temperatures, but we are still limited by noise due to the readout amplifier and fluctuations in the

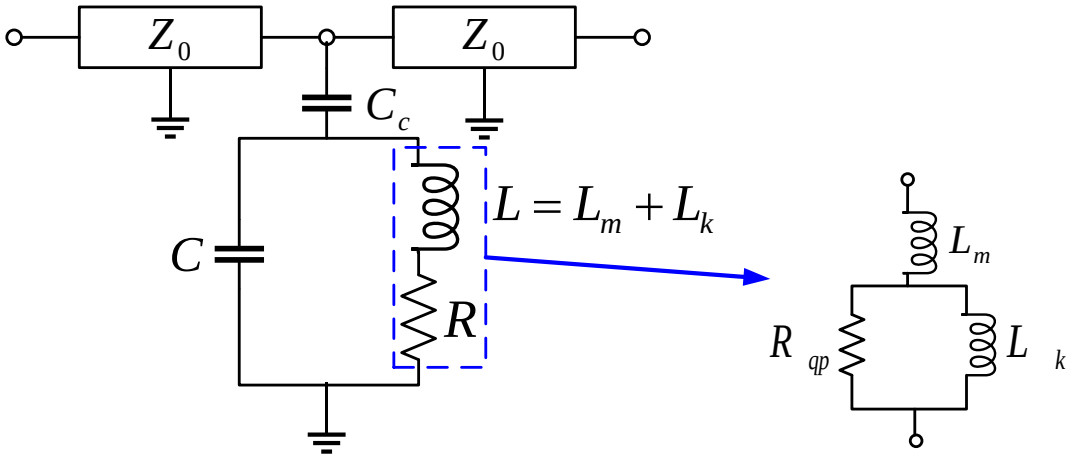

(a)

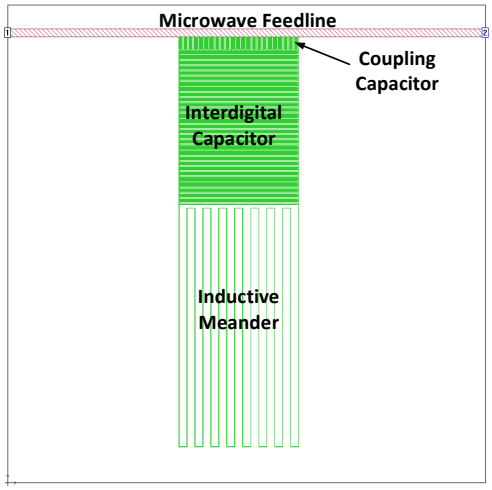

(b)

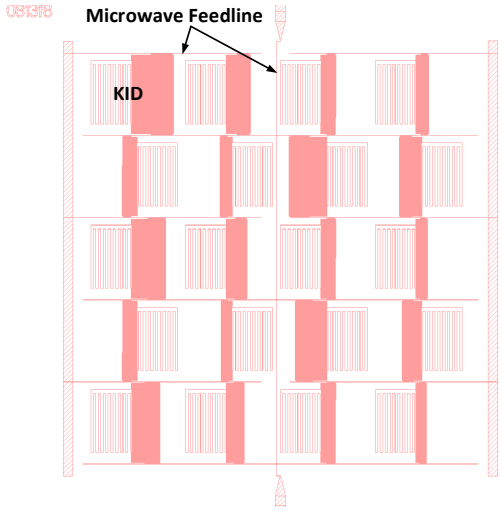

(c)

Figure 3: Lumped element circuit model of a single KID with closeup that illustrates the two-fluid model of superconductivity (a). Single KID pixel design with microstrip geometry (b). 20-element array of KIDs sharing a common feedline (c).

complex dielectric constant of amorphous dielectrics known as two-level system (TLS) noise. Continuing improvements to the noise performance of low noise amplifiers (LNAs) (Akgiray et al. 2013; Bardin, Montazeri, and Chang 2017; Chaudhuri, Gao,

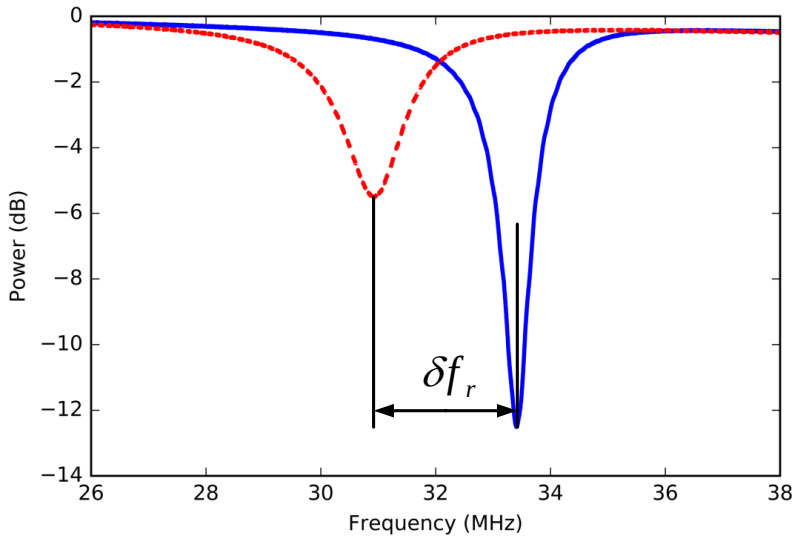

Figure 4: Response of a low frequency KID measured in our laboratory. The red and blue curves are magnitude of S_{21} curves with and without optical loading, respectively. Pair-breaking due to photon absorption increases both L_s and R_s of the superconducting film, which shifts the resonant frequency downward and produces a broader and shallower resonant feature due to the decreased quality factor.

and Irwin 2015; Vissers et al. 2016) combined with concerted efforts to reduce TLS noise (Noroozian 2012) have enabled KIDs to achieve NEP $\simeq 3 \times 10^{-19}$ W/$\sqrt{\text{Hz}}$ (Baselmans et al. 2016; J. Bueno et al. 2017), which rivals ultra-low NEP transition edge sensors (TESs) in sensitivity (Suzuki et al. 2016; Audley et al. 2016).

The key advantages of KIDs over state-of-the-art TESs are two-fold. First, KIDs are naturally multiplexable in the frequency domain, enabling thousands of detectors to be read out on a single transmission line instead of requiring complex circuitry based on superconducting quantum interference devices (SQUIDs) to read out each individual TES. Since both TES and KID technology for millimeter-wave astronomy have already achieved photon-limited performance (Juan Bueno et al. 2016; Hubmayr et al. 2015; Mauskopf et al. 2014; Beyer et al. 2012; Kenyon et al. 2006) for individual

detectors, significant improvement to instrument sensitivity requires large focal plane arrays with $\sim 10^4 - 10^6$ pixels. The inherently high multiplexing ratio for KIDs facilitates the development of these large arrays, which are required to advance the science described in Chapter 1. Substantial efforts have been dedicated to developing field programmable gate array (FPGA)-based readout systems to generate and process a comb of tones corresponding to the resonant frequencies of all KIDs weakly coupled to the microwave feedline down which the tones will propagate to probe the response of each detector. A multiplexing ratio of 1024 has recently been demonstrated for the next generation of the Balloon-borne Large Aperture Submillimeter Telescope (BLAST-TNG) (Gordon et al. 2016). Second, fabrication is significantly simpler for KIDs than for TESs. Most KID designs require only a single photolithography step compared to > 10 such steps for recent TES designs (Posada et al. 2015)

2.3.2 Microwave Resonator Circuit

The previous sections have described the physics of superconductors in general and KIDs in particular. We now provide a detailed description of the KID as a microwave resonator circuit. A signal on the feedline in Fig. 3a sees the KID as a shunt impedance to ground given by

$$\begin{aligned} Z_{\rm res}(\omega) &= \frac{1}{j\omega C_c} + \frac{1}{j\omega C + \dfrac{1}{j\omega L + R}} \\ &= \frac{1}{j\omega C_c}\left[\frac{1-\omega^2 L\left(C+C_c\right)+j\omega R\left(C+C_c\right)}{1-\omega^2 LC + j\omega RC}\right]. \end{aligned} \tag{2.46}$$

Using Eq. 2.44, Eq. 2.46 becomes

$$Z_{\rm res}\left(\omega_r\right) = R\left(\frac{C+C_c}{C_c}\right)^2 \frac{1}{1+j\omega_r RC\left(\frac{C+C_c}{C_c}\right)}$$
$$= \frac{Z_0}{2}\frac{Q_c}{Q_i}\frac{1}{1+j\epsilon}, \tag{2.47}$$

where

$$Q_c = \frac{2\left(C+C_c\right)}{\omega_r C_c^2 Z_0} \tag{2.48}$$

is the quality factor describing coupling to the feedline (Göppl et al. 2008) and

$$\epsilon = \omega_r RC\left(\frac{C+C_c}{C_c}\right) = \frac{C}{Q_i C_c}. \tag{2.49}$$

Defining

$$x = \frac{\delta\omega}{\omega_r} = \frac{\omega-\omega_r}{\omega_r}, \tag{2.50}$$

the resonator impedance is approximately

$$Z_{\rm res}\left(\omega\right) \simeq \left(\frac{Z_0}{2}\frac{Q_c}{Q_i} + jZ_0 Q_c x\right)\frac{1}{1+j\epsilon} \tag{2.51}$$

near resonance, where x is known as the fractional detuning of the resonant frequency.

To probe the response of a KID, we measure the insertion and return loss of a signal tuned to its resonant frequency propagating past it on the feedline. For a 2-port network consisting of a shunt impedance to ground,

$$S_{21} = 1 - \frac{1}{1+2Z_{\rm res}/Z_0} \tag{2.52a}$$
$$S_{11} = S_{21} - 1 = -\frac{1}{1+2Z_{\rm res}/Z_0}. \tag{2.52b}$$

Substituting Eq. 2.51 into Eq. 2.52a, we obtain

$$S_{21}\left(x\right) = 1 - \frac{1+j\epsilon}{1+j\epsilon Q_{\rm res}/Q_c}\frac{Q_{\rm res}}{Q_c}\left[\frac{1}{1+2jQ_{\rm res}x/\left(1+j\epsilon Q_{\rm res}/Q_c\right)}\right], \tag{2.53}$$

where $Q_{\rm res}$ is the loaded quality factor of the resonator given by

$$\frac{1}{Q_{\rm res}} = \frac{1}{Q_i} + \frac{1}{Q_c}. \tag{2.54}$$

assuming no additional source of loss. In the limit $\epsilon \ll 1$,

$$S_{21}(x) \simeq 1 - \frac{Q_{\rm res}}{Q_c} \frac{1}{1 + 2jQ_{\rm res}x} \tag{2.55a}$$

$$S_{11}(x) \simeq -\frac{Q_{\rm res}}{Q_c} \frac{1}{1 + 2jQ_{\rm res}x}, \tag{2.55b}$$

which are Lorentzian with location parameter and FWHM described by ω_r and $Q_{\rm res}$, respectively. From Eqs. 2.46 and 2.53, we see that a KID is described by the five circuit parameters (L, C, C_c, R, Z_0), which translate to the four empirical parameters $(\epsilon, \omega_r, Q_{\rm res}, Q_c)$.

We now take a closer look at the circuit representation of the two fluid model in Fig. 3a. The closeup shows the parallel resonator's inductive branch, which consists of the magnetic inductance in series with the parallel combination of the kinetic inductance of Cooper pairs and resistance of quasiparticles. Therefore, the impedance of this branch is

$$\begin{aligned} Z_L(\omega) &= j\omega L_m + \frac{1}{\dfrac{1}{R_{qp}} + \dfrac{1}{j\omega L_k}} \\ &= j\omega L_m + \frac{j\omega L_k R_{qp}^2 + \omega^2 L_k^2 R_{qp}}{R_{qp}^2 + \omega^2 L_k^2}. \end{aligned} \tag{2.56}$$

For $T \ll T_c$, the impedance due to quasiparticles dominates, so Eq. 2.56 becomes

$$Z_L(\omega) = \frac{\omega^2 L_k^2}{R_{qp}} + j\omega(L_m + L_k) \tag{2.57}$$

and the internal quality factor is given by

$$Q_i = \frac{\mathrm{Im}\{Z_L(\omega_r)\}}{\mathrm{Re}\{Z_L(\omega_r)\}} = \frac{L_m + L_k}{L_k} \frac{R_{qp}}{\omega_0 L_k}. \tag{2.58}$$

In general, R_{qp} varies as a function of frequency at a fixed temperature because the conductivity of the quasiparticles varies with frequency according to BCS theory.

2.3.3 Thermal and Optical Responsivity

For KIDs, a change in the quasiparticle density in the superconducting film manifests empirically as changes in resonant frequency f_r and quality factor Q_{res}. Both phonons and photons with energy $> 2\Delta$ break Cooper pairs to generate excess quasiparticles in the superconducting state. We now derive the predicted shift in f_r in response to changes in temperature T and absorbed optical power P_{abs} using Mattis-Bardeen formalism.

We can characterize a KID by its response to changes in temperature under dark conditions. From Eqs. 2.37 and 2.38, we see that a change in surface impedance due to pair breaking changes the kinetic inductance, which changes the total inductance of the circuit. From Eq. 2.44, we relate change in resonant frequency to change in kinetic inductance by

$$\frac{df_r}{dL_k} = -\frac{\alpha}{2}\frac{f_r}{L_k}, \tag{2.59}$$

where $\alpha = L_k/\left(L_m + L_k\right)$ is the kinetic inductance ratio. Using Eq. 2.38,

$$\frac{dL_k}{d\sigma_2} = -\frac{L_k}{\sigma_2}, \tag{2.60}$$

so combining the previous two equations results in

$$\frac{df_r}{d\sigma_2} = \frac{\alpha}{2}\frac{f_r}{\sigma_2}. \tag{2.61}$$

The resonant frequency shift due to a change in temperature is

$$\frac{df_r}{dT} = \frac{df_r}{d\sigma_2}\frac{d\sigma_2}{dn_{qp}}\frac{dn_{qp}}{dT}. \tag{2.62}$$

Using Eq. 2.32b, the middle factor on the right side of Eq. 2.62 is given by

$$\frac{d\sigma_2}{dn_{qp}} = -\frac{\sigma_2}{2N_0\Delta_0}\left(1 + \sqrt{\frac{2\Delta_0}{\pi k_B T}}e^{-\chi}I_0\left(\chi\right)\right) \tag{2.63}$$

and taking the derivative of n_{qp} in Eq. 2.31 with respect to temperature yields

$$\frac{dn_{qp}}{dT} \simeq \frac{n_{qp}}{T}\left(\frac{1}{2}+\frac{\Delta}{k_B T}\right). \tag{2.64}$$

By substituting Eqs. 2.61, 2.63, and 2.64 into Eq. 2.62, we obtain the response of resonant frequency to temperature to be

$$\begin{aligned}\frac{df_r}{dT} &= -\frac{\alpha}{2}\frac{f_r}{\sigma_2}\frac{\sigma_2}{2N_0\Delta_0}\left(1+\sqrt{\frac{2\Delta_0}{\pi k_B T}}e^{-\chi}I_0\left(\chi\right)\right)\frac{n_{qp}}{T}\left(\frac{1}{2}+\frac{\Delta}{k_B T}\right)\\ &= -\frac{\alpha f_r}{2T}\sqrt{\frac{2\pi k_B T}{\Delta_0}}e^{-\Delta/k_B T}\left(\frac{1}{2}+\frac{\Delta}{k_B T}\right)\left(1+\sqrt{\frac{2\Delta_0}{\pi k_B T}}e^{-\chi}I_0\left(\chi\right)\right),\end{aligned} \tag{2.65}$$

where we have used

$$\frac{1}{2N_0} = \frac{\sqrt{2\pi k_B T\Delta_0}}{n_{qp}}e^{-\Delta/k_B T}, \tag{2.66}$$

which is just Eq. 2.31 rearranged.

The primary purpose of a KID is to detect light, so we now derive its response to absorbing pair-breaking photons. Assuming that absorbed optical power is uniformly distributed throughout the inductive meander portion of the KID circuit, Cooper pair breaking increases the average quasiparticle density in the superconducting film. As shown by (Gao 2008), thermally and optically generated quasiparticles have an equivalent effect on the complex conductivity and thus surface impedance of the film at low temperatures. As with the thermal response, optical response also manifests as a change in f_r and Q_{res}. In general, the loaded quality factor of the resonator is

$$\frac{1}{Q_{\mathrm{res}}} = \frac{1}{Q_i}+\frac{1}{Q_c}+\frac{1}{Q_{\mathrm{loss}}} \tag{2.67a}$$

$$= \frac{f_r}{\Delta f}, \tag{2.67b}$$

where we add $1/Q_{\mathrm{loss}}$ to the right side of Eq. 2.54 to parametrize any loss mechanism in addition to quasiparticle dissipation and Δf is the 3-dB bandwidth of the resonant feature. When we probe KID response with a tone tuned to f_r, we directly measure

$Q_{\rm res}$, but changes in surface impedance change Q_i. It is difficult to specifically monitor Q_i, especially at low optical power levels where $Q_{\rm res}$ is dominated by Q_c and/or $Q_{\rm loss}$. Therefore, f_r, which is directly affected by absorption of optical power, is its primary monitor.

The analog to Eq. 2.62 for optical power absorbed is

$$\frac{df_r}{dP_{\rm abs}} = \frac{df_r}{d\sigma_2}\frac{d\sigma_2}{dn_{qp}}\frac{dn_{qp}}{dP_{\rm abs}} \tag{2.68}$$

In the limit $\chi = \hbar\omega_r/2k_BT \ll 1$, the middle factor on the right side of Eq. 2.68 becomes

$$\frac{d\sigma_2}{dn_{qp}} \simeq -\frac{\sigma_2}{2N_0\Delta_0}\left(1+\sqrt{\frac{2\Delta_0}{\pi k_BT}}\right). \tag{2.69}$$

To determine $dn_{qp}/dP_{\rm abs}$, we need to know the total rate of quasiparticle generation due to all mechanisms. For a BCS superconductor, the approximate rate equation is

$$\frac{dn_{qp}}{dt} = \Gamma_{\rm opt} + \Gamma_{\rm ro} + \Gamma_{\rm th} - \Gamma_{\rm rec} \tag{2.70a}$$

$$= \frac{\eta P_{\rm abs}}{\Delta\Sigma} + \frac{\varepsilon P_{\rm ro}}{\Delta\Sigma} + \gamma N_0^2 8\pi k_BT\Delta e^{-2\Delta/k_BT} - \frac{n_{qp}}{\tau_{qp}}, \tag{2.70b}$$

where η and ε are the quasiparticle generation efficiencies for absorbed optical and readout power, respectively, Σ is the superconductor volume, τ is the average quasiparticle recombination time known as the quasiparticle lifetime, and $\gamma = (n_{qp}\tau_{qp})^{-1}$. $\Gamma_{\rm opt}$, $\Gamma_{\rm ro}$, and $\Gamma_{\rm th}$ represent quasiparticle generation due to optical power, readout power, and thermal phonons, respectively. The final term in Eq. 2.70b represents the rate at which quasiparticles recombine into Cooper pairs. At low temperatures, the quasiparticle lifetime takes the form

$$\tau_{qp} = \frac{\tau_0}{\sqrt{\pi}}\left(\frac{k_BT_c}{2\Delta}\right)^{5/2}\sqrt{\frac{T_c}{T}}e^{\Delta/k_BT} \tag{2.71a}$$

$$= \frac{\tau_0}{n_{qp}}\frac{N_0\left(k_BT_c\right)^2}{2\Delta^2} \tag{2.71b}$$

as derived in (Kaplan et al. 1976), where τ_0 is the characteristic electron-phonon interaction time for the material. See (Goldie and Withington 2012) for a more complete description of the rate equation governing quasiparticle generation.

The two main superconducting materials used for KIDs are aluminum and titanium nitride (TiN), which each exhibit a different limiting case of Eq. 2.70b. Aluminum KIDs, for which we will discuss design and fabrication in Section 3.2, have been shown to exhibit Mattis-Bardeen thermal behavior with quasiparticle generation dominated by absorption of optical power (Flanigan et al. 2016). In this limit, Eq 2.70b reduces to

$$\frac{dn_{qp}}{dt} \simeq \frac{\eta P_{\rm abs}}{\Delta\Sigma} - \gamma n_{qp}^2 \tag{2.72}$$

and, as derived in [Mauskopf review paper, ask Phil how to cite],

$$\frac{dn_{qp}}{dP_{\rm abs}} = \frac{1}{2}\sqrt{\frac{\eta}{\gamma P_{\rm abs}\Delta\Sigma}}\frac{1}{1+j\omega\tau_{\rm eff}} \tag{2.73}$$

in the small signal limit, where $\tau_{\rm eff} = \tau_{qp}/2$. Substituting Eqs. 2.61, 2.69, and 2.73 into Eq. 2.68, we obtain the response of resonant frequency to absorbed optical power to be

$$\begin{aligned}\frac{df_r}{dP_{\rm abs}} &= -\frac{\alpha}{2}\frac{f_r}{\sigma_2}\frac{\sigma_2}{2N_0\Delta_0}\left(1+\sqrt{\frac{2\Delta_0}{\pi k_B T}}\right)\frac{1}{2}\sqrt{\frac{\eta}{\gamma P_{\rm abs}\Delta\Sigma}}\frac{1}{1+j\omega\tau_{\rm eff}} \\ &= -\frac{\alpha f_r}{8N_0\Delta_0}\left(1+\sqrt{\frac{2\Delta_0}{\pi k_B T}}\right)\sqrt{\frac{\eta}{\gamma P_{\rm abs}\Delta\Sigma}}\frac{1}{1+j\omega\tau_{\rm eff}} \qquad (2.74) \\ &\propto \frac{1}{\sqrt{P_{\rm abs}\Sigma}} \qquad (2.75)\end{aligned}$$

in this first limiting case. We see that the responsivity is proportional to the inverse square root of both absorbed optical power and detector volume. Therefore, reducing the volume of the inductive meander portion of the KID is a method for increasing its optical responsivity.

TiN KIDs, for which we will discuss optimal geometry in Section 3.1, have generally been observed to exhibit the opposite limit, in which quasiparticle generation is dominated by a constant thermal generation rate (Hailey-Dunsheath et al. 2016; Hubmayr et al. 2015). In this limit, Eq. 2.70b becomes

$$\frac{dn_{qp}}{dt} \simeq \frac{\eta P_{\mathrm{abs}}}{\Delta\Sigma} + \Gamma_{\mathrm{th}} - \frac{n_{qp}}{\tau_{\mathrm{eff}}} \tag{2.76}$$

and applying the small signal approximation again, we obtain

$$\frac{dn_{qp}}{dP_{\mathrm{abs}}} = \frac{\eta\tau_{\mathrm{eff}}}{\Delta\Sigma}\frac{1}{a + j\omega\tau_{\mathrm{eff}}} \tag{2.77}$$

Therefore, the response of resonant frequency to absorbed optical power in this second limiting case is

$$\frac{df_r}{dP_{\mathrm{abs}}} = -\frac{\alpha f_r}{2N_0\Delta_0}\left(1 + \sqrt{\frac{2\Delta_0}{\pi k_B T}}\right)\frac{\eta\tau_{\mathrm{eff}}}{\delta\Sigma} \tag{2.78a}$$

$$\propto \frac{\tau_{\mathrm{eff}}}{\Sigma}. \tag{2.78b}$$

We see that the responsivity is inversely proportional to detector volume and independent of absorbed optical power. Since the responsivity is more sensitive to detector volume than in the first limiting case, reducing detector volume for a TiN KID should increase responsivity more than a comparable volume reduction for an aluminum KID.

We have derived analytical approximations for both the thermal and optical responsivity assuming BCS and Mattis-Bardeen formalism for superconductors. It is important to note that recent devices, especially those fabricated using TiN films, exhibit electromagnetic behavior that deviates significantly from these established theories. These observations have generated a burgeoning new area of research into understanding the anomalous behavior of thin superconducting films. (Gao et al. 2013; J. Bueno et al. 2014) provide a detailed studies of such behavior in TiN resonators and

(Coumou, Zuiddam, et al. 2013; Coumou, Driessen, et al. 2013; Bespalov et al. 2016; Žemlička et al. 2015; Guruswamy et al. 2017) comprise a sampling of recent progress on understanding a variety of anomalous effects.

2.3.4 Sensitivity

In Section 2.3.3, we described how KIDs respond to thermal and optical signals. To complete our description of detector performance, we need to determine the weakest possible signal strength that is able to be detected in the presence of noise. This minimum detectable signal strength characterizes the detector's sensitivity. For KIDs and other photodetectors, the most common measure of sensitivity is noise equivalent power (NEP), which is the signal power necessary to achieve a signal-to-noise ratio of unity in one Hz of output bandwidth[1]. For KIDs, sources of noise include photon noise, generation-recombination (g-r) noise, readout amplifier noise, and two-level system (TLS) noise, each of which contribute an NEP. Even if the entire receiver is internally noiseless, inherent fluctuations in the incident photon stream provide a fundamental limit to sensitivity known as the photon noise limit. The fundamental limit to sensitivity inherent to the detector is due to random generation and recombination of quasiparticles in the superconducting film. So far, efforts to achieve the highest possible sensitivity have focused on reducing amplifier and TLS noise (Akgiray et al. 2013; Bardin, Montazeri, and Chang 2017; Vissers et al. 2016; Noroozian 2012).

We describe photon noise following (Steve Hailey-Dunsheath 2017). Due to the quantized nature of light, the photon flux incident on a detector inherently varies. The

[1] 1 Hz of output bandwidth is equivalent to 0.5 s of integration time.

photon occupation number in a thermal source with temperature T and emissivity $\epsilon(f)$ follows the Bose-Einstein distribution, namely

$$n_0(f) = \frac{1}{e^{hf/k_BT} - 1}. \tag{2.79}$$

For a detector that detects light from the source with efficiency $\eta(f)$, the photon NEP is given by

$$\mathrm{NEP}^2_{\mathrm{ph}} = 2\int_0^\infty (\hbar f)^2 N_{\mathrm{pol}}(f) N_{\mathrm{mode}}(f) n(f) [1 + n(f)] df, \tag{2.80}$$

where $N_{\mathrm{pol}}(f)$ and $N_{\mathrm{mode}}(f)$ are the number of polarizations and modes, respectively, and

$$n(f) = \epsilon(f)\eta(f) n_0(f) \tag{2.81}$$

is the photon occupation number in the detector. The power absorbed by the detector per unit frequency is

$$P_{\mathrm{abs}}(f) = (hf) N_{\mathrm{ph}}(f) N_{\mathrm{mode}}(f), \tag{2.82}$$

so we can write Eq. 2.80 as

$$\mathrm{NEP}^2_{\mathrm{ph}} = 2\left[\int_0^\infty (hf) P_{\mathrm{abs}}(f) df + \int_0^\infty \frac{1}{N_{\mathrm{pol}}(f) N_{\mathrm{mode}}(f)} df\right], \tag{2.83}$$

where the first term represents shot noise and second term represents wave noise.

Random fluctuations in quasiparticle density present the fundamental intrinsic limit to KID sensitivity. These perturbations to n_{qp} may be due to either thermal fluctuations or stray light from sources other than our intended target. The general g-r contribution to NEP is given by

$$\mathrm{NEP}_{\mathrm{g-r}} = \frac{2\Delta}{\eta}\sqrt{\frac{N_{qp}}{\tau_{qp}}}, \tag{2.84}$$

where η is the quasiparticle generation efficiency of either thermal or photon energy and N_{qp} is the total number of quasiparticles (Sergeev and Reizer 1996). As derived

in (Lowitz et al. 2014), the optical g-r NEP is

$$\mathrm{NEP}_{\mathrm{g-r}}^{\mathrm{opt}} = \sqrt{\frac{4\Delta P_{\mathrm{abs}}}{\eta}}, \tag{2.85}$$

where P_{abs} is the stray light power absorbed, while the thermal g-r NEP retains the form of Eq. 2.84. (De Visser et al. 2012) experimentally verified Eq. 2.84 for aluminum KIDs. The noise power spectrum for the effect of quasiparticle number fluctuations on resonator amplitude A is

$$S_A(\omega) = S_N(\omega) \left(\frac{dA}{dN_{qp}}\right)^2 \frac{1}{1 + (\omega\tau_{\mathrm{res}})^2}, \tag{2.86}$$

where

$$S_N(\omega) = \frac{4N_{qp}\tau_{qp}}{1 + (\omega\tau_{qp})^2} \tag{2.87}$$

is a Lorentzian power spectrum (Wilson and Prober 2003) and $\tau_{\mathrm{res}} = Q_{\mathrm{res}}/\pi f_r$ is the resonator ring-down time. Converting Eq. 2.86 to NEP yields

$$\mathrm{NEP}_{\mathrm{q-p}}^{\mathrm{th}}(\omega) = \sqrt{S_A} \left(\frac{\eta\tau_{qp}}{\Delta}\frac{dA}{dN_{qp}}\right)^{-1} \sqrt{\left(1 + \omega^2\tau_{qp}^2\right)\left(1 + \omega^2\tau_{\mathrm{res}}^2\right)}. \tag{2.88}$$

With $\eta = 0.57$, (De Visser et al. 2012) used measured values for the parameters in Eq. 2.88 to calculate the g-r contribution to NEP for aluminum KIDs, which is consistent with theory.

Readout tones need to be attenuated to 1 fW $-$ 100 pW before probing the KIDs. The thermal noise power at room temperature is $P_{300\,\mathrm{K}} = k_B T \Delta f \approx 4$ pW for $\Delta f = 1$ GHz. Therefore, we need to amplify the signal after the KIDs, but still on the cold stage, to a power level able to be processed by room temperature electronics. Cryogenic solid state low noise amplifiers (LNAs) (Mani and Mauskopf 2014; Bardin, Montazeri, and Chang 2017) and the emerging kinetic inductance parametric amplifiers (TKIPs) (Chaudhuri, Gao, and Irwin 2015; Vissers et al. 2016) accomplish this task.

The fundamental quantum noise limit for these amplifiers corresponds to a noise temperature of $T_{ql} = hf_r/k_B$, where f_r is the readout frequency (Caves 1982), namely

$$e_{\text{amp}} = \sqrt{4k_B T_{\text{amp}} Z_{\text{amp}}}, \tag{2.89}$$

where T_{amp} and Z_{amp} are the amplifier's noise temperature and input impedance, respectively. The noise power spectrum for amplifier fluctuations is

$$S_{f_r} = \frac{e_{\text{amp}}^2}{|dV_{\text{out}}/df_r|^2} \tag{2.90}$$

where

$$\begin{aligned} \frac{dV_{\text{out}}}{df_r} &= V_{\text{in}} \frac{dS_{21}}{df_r} \\ &\simeq 2jV_{\text{in}} \frac{Q_{\text{res}}^2}{Q_c} \frac{f}{f_r^2} \frac{1}{(1 + 2jQ_{\text{res}}x)^2}. \end{aligned} \tag{2.91}$$

In Eq. 2.91, we use Eq. 2.55a for S_{21} of the resonator. Therefore, the noise power spectrum becomes

$$S_{f_r} = 4k_B T_a Z_a \left(\frac{1}{V_{\text{in}}} \frac{Q_c}{2Q_{\text{res}}^2} \right)^2. \tag{2.92}$$

Because the readout power is $P_{ro} = V_{\text{in}}^2/Z_{\text{amp}}$, the voltage noise in response to changes in resonant frequency increases with readout power.

The final source of noise we discuss is due to variations in the permittivity and permeability of amorphous dielectric materials, which result in fluctuations in capacitance and inductance, respectively. These variations are caused by random oscillations of the electric and/or magnetic dipoles in the materials, which are modeled as two-level systems (TLS). So far, fluctuations in capacitance has been found to be the dominant form of TLS noise. TLS noise depends on KID geometry, readout power, and operating temperature, which strongly supports a noise model based on a distribution of TLSs on the surface instead of the bulk of the superconductor (Gao,

Daal, Martinis, et al. 2008; Gao, Daal, Vayonakis, et al. 2008). Studies agree on a $1/f$ dependence on frequency (Burnett et al. 2013; Neill et al. 2013) and $1/\sqrt{P}$ dependence on readout power (Gao, Daal, Martinis, et al. 2008). (Faoro and Ioffe 2015) recently developed a modification of the standard tunneling model of TLSs that perfectly agrees with recent measurements of TLS noise in high quality factor superconductor resonators. Increasing readout power and operating temperature reduces TLS noise, but thermal noise increases with temperature (Gao 2008). In addition, there is a maximum readout power level before the onset of non-linear behavior, which we discuss in Section 2.3.5. (Noroozian 2012) presents an extensive method to optimize the geometry of TiN KIDs for minimum TLS noise contribution.

2.3.5 Non-Linear Behavior

As previously mentioned, high readout powers bring about non-linear electromagnetic behavior in superconducting films. In particular, the kinetic inductance becomes a non-linear function of current, namely

$$L_k(I) \simeq L_{k,0}\left[1+\left(\frac{I}{I_*}\right)^2\right], \tag{2.93}$$

where $L_{k,0}$ is the intrinsic kinetic inductance given by Eq. 2.38 and I_* is the characteristic current that sets the scale for the nonlinearity. We can account for the resonant frequency shift $\delta\omega_r = \omega_r - \omega_{r,0}$ due to non-linear kinetic inductance at high readout powers by modifying our expression for fractional detuning in Eq. 2.50 to

$$x = \frac{\omega - (\omega_{r,0} + \delta\omega_r)}{\omega_{r,0} + \delta\omega_r} \tag{2.94a}$$

$$\approx x_0 - \delta x \tag{2.94b}$$

where $\omega_{r,0}$ and x_0 are the resonant frequency and fractional detuning at low readout power, respectively. Combining Eqs. 2.44 and 2.93, the non-linear fractional frequency shift can be written as

$$\delta x = \frac{\delta\omega_r}{\omega_{r,0}} = -\frac{1}{2}\frac{\delta L}{L} = -\frac{\alpha}{2}\frac{I^2}{I_*^2}, \tag{2.95}$$

where α is the kinetic inductance ratio.

Following (Swenson et al. 2013), we derive an expression for energy stored in the resonator $E_{\rm res}$ as a function of frequency and readout power. The amount of readout power dissipated in the resonator is

$$P_{\rm diss} = P_{\rm ro}\left(1 - |S_{11}|^2 - |S_{21}|^2\right), \tag{2.96}$$

where S_{21} and S_{11} describe the insertion and return loss of the resonant circuit, respectively, as defined in Section 2.3.2. Substituting Eqs. 2.55a and 2.55b into Eq. 2.96, the power dissipated becomes

$$P_{\rm diss} = P_{\rm ro}\left(\frac{2Q_{\rm res}^2}{Q_i Q_c}\frac{1}{1+4Q_{\rm res}^2x^2}\right). \tag{2.97}$$

Since the internal quality factor is defined as

$$Q_i = \frac{\omega_r E_{\rm res}}{P_{\rm diss}}, \tag{2.98}$$

the stored energy is

$$E_{\rm res} = \frac{1}{2}LI^2 = \frac{2Q_{\rm res}^2}{Q_c}\frac{1}{1+4Q_{\rm res}^2x^2}\frac{P_{\rm ro}}{\omega_r}, \tag{2.99}$$

which relates both readout power and current to stored energy. From Eq. 2.99 and 2.95, non-linear detuning can also be expressed as

$$\delta x = -\frac{E_{\rm res}}{E_*}, \tag{2.100}$$

where $E_* = LI_*^2/\alpha$ is on the order of the condensation energy of the inductor

$$E_c = \frac{N_0 \Delta^2 \Sigma}{2} \tag{2.101}$$

when $\alpha \approx 1$.

At readout powers for which non-linear kinetic inductance is appreciable, the resonator behavior bifurcates into two states at the same readout power and frequency. The state the resonator occupies depends on whether the frequency sweep is performed upward from below the low-power resonant frequency $f_{r,0}$ or downward from above $f_{r,0}$. For details regarding bifurcation and a complete model describing non-linear behavior of KIDs, see (Swenson et al. 2013). In general, we want to use a readout power just below the onset of bifurcation to minimize TLS noise while avoiding possible switching between the two resonator states in the bifurcated regime. To estimate this maximum readout power, we require the resonant frequency shift due to non-linear kinetic inductance to be less than the resonator linewidth, namely

$$|\delta x| = \frac{E_{\rm res}}{E_*} < \frac{1}{Q_{\rm res}}, \tag{2.102}$$

where we have used Eq. 2.100. Since $E_* \sim E_c$,

$$E_{\rm res} < \frac{N_0 \Delta^2 \Sigma}{2Q_{\rm res}} \tag{2.103}$$

and substituting Eq. 2.103 into Eq. 2.99 yields

$$P_{\rm ro} < \frac{Q_c}{2Q_{\rm res}^3} \omega_r N_0 \Delta^2 \Sigma \left(1 + 4Q_{\rm res}^2 x^2\right), \tag{2.104}$$

which provides an upper bound to readout power. Typical readout powers for aluminum and TiN KIDs are -130 dBm $\lesssim P_{\rm ro} \lesssim -70$ dBm.

The propagation speed on a superconducting transmission line is given by

$$v_p = \frac{1}{\sqrt{\mathcal{L}\mathcal{C}}}, \tag{2.105}$$

where $\mathcal{L}$ and $\mathcal{C}$ are its total inductance and capacitance per unit length. Therefore, we can also exploit the current dependent non-linear kinetic inductance to develop superconducting delay line devices such as the dual-purpose phase shifter and traveling wave kinetic inductance parametric amplifier (TKIP) to be discussed in Chapter 5. The current controlled propagation speed is

$$\begin{aligned} v_p &= v_{p,0} + \delta v_p \\ &= v_{p,0} + \frac{dv_p}{d\mathcal{L}}\delta\mathcal{L} \end{aligned} \tag{2.106}$$

where $v_{p,0}$ is the unbiased propagation speed and δv_p is the change in propagation speed due to applied current, which changes the inductance. From Eq. 2.105,

$$\begin{aligned} \frac{dv_p}{d\mathcal{L}} &= -\frac{1}{2}\frac{1}{\mathcal{L}}\frac{1}{\sqrt{\mathcal{L}\mathcal{C}}} \\ &= -\frac{1}{2}\frac{v_{p,0}}{\mathcal{L}}, \end{aligned} \tag{2.107}$$

so Eq. 2.106 becomes

$$\begin{aligned} v_p &= v_{p,0}\left(1 - \frac{1}{2}\frac{d\mathcal{L}}{\mathcal{L}}\right) \\ &= v_{p,0}\left(1 - \frac{\alpha}{2}\frac{I^2}{I_*^2}\right), \end{aligned} \tag{2.108}$$

where we use Eq. 2.95 for the second term. The unbiased effective path length of a superconducting transmission line at frequency f is

$$\phi_0 = \frac{2\pi f l}{v_{p,0}}, \tag{2.109}$$

where l is its physical length. Applying a bias current I to the same line modifies the effective path length to

$$\phi\left(I\right) = \frac{2\pi f l}{v_p\left(I\right)} = \frac{2\pi f l}{v_{p,0}\left(1 - \frac{\alpha}{2}\frac{I^2}{I_*^2}\right)}, \tag{2.110}$$

so the path length difference between a biased and unbiased line is

$$\begin{aligned}\Delta\phi &= \phi(I) - \phi_0 \\ &= \frac{2\pi f l}{v_{p,0}\left(1 - \frac{\alpha}{2}\frac{I^2}{I_*^2}\right)}\frac{\alpha}{2}\frac{I^2}{I_*^2} \\ &= \frac{\alpha\phi(I)}{2}\frac{I^2}{I_*^2}.\end{aligned} \tag{2.111}$$

This path length difference, also known as the non-linear phase shift, is controlled by the choice of superconductor, bias current, and physical length of the transmission line. $\Delta\phi$ determines the maximum possible gain that can be achieved by a TKIP employing a given transmission line geometry.

2.3.6 Optical Coupling

We have discussed how a KID responds to incident optical power, the sources of noise that determine its sensitivity, and its non-linear behavior at high readout powers. However, we first need to efficiently couple light from the sky in the target frequency band to the detector. The three main methods for optical coupling are filled arrays, horn coupling, and planar antenna coupling. See (Mauskopf 2017) for a detailed overview of all three methods, their tradeoffs, and their constraints on detector designs. We briefly describe and provide a few examples for each method. Filled arrays are closely-packed focal plane arrays of KID pixels that absorb incident light directly from telescope optics. Theoretically, filled arrays can achieve the highest optical efficiency of the three methods, but are more susceptible to stray light and difficult to integrate with readout electronics at high fill factors (Griffin, Bock, and Gear 2002). The Neel Iram KID Array (NIKA) (Monfardini et al. 2010; Monfardini et al. 2011) and second generation NIKA 2 (Catalano et al. 2016) instruments employ

filled arrays of KIDs targeting the 150 GHz and 260 GHz bands. For horn coupling, light propagating in free space is coupled to KIDs through single mode horn antennas with radiation patterns matching the field distribution of the free space mode at the focal plane. While adjacent detectors need to be spaced further apart than in filled arrays, horn coupling enables smaller detector sizes and effective stray light control (Mauskopf 2017). To be described in Sections 3.2 and 3.1, respectively, the KID arrays for cosmic microwave background studies (H McCarrick et al. 2014; Heather McCarrick et al. 2016) and BLAST-TNG instrument (Galitzki et al. 2014) employ horn coupling. In addition to horn antennas, on-chip planar antennas provide another method for coupling free space radiation to KIDs. A common configuration employs a lens to couple light from telescope optics to the radiation pattern of an array of planar antennas in the focal plane. To be discussed in Chapter 4, light is coupled to the current generation of SuperSpec devices (Wheeler et al. 2017) via lens-coupled bowtie antennas.

Chapter 3

DETECTOR DESIGN AND FABRICATION

In this chapter, we present our contribution to three major efforts to develop KID array instruments for millimeter-wave astronomy. Led by the University of Pennsylvania, the next generation Balloon-borne Large Aperture Submillimeter Telescopes for Polarimetry (BLAST-TNG) is a KID-based suborbital telescope designed to study interstellar magnetic fields and their effect on star formation. We performed extensive electromagnetic simulations to provide a horn coupled dual-polarization KID design optimized for minimum cross-polar (x-pol) to co-polar (co-pol) coupling ratio. We are also a major collaborator in an effort led by Columbia University to develop horn coupled dual-polarization KID arrays for ground-based cosmic microwave background (CMB) polarimetry. Our primary contribution to this effort has been detector fabrication using the ASU NanoFab. Assuming a minor role in the Sapienza-led OLIMPO CMB experiment, we provided an initial KID design based on Hilbert fractal absorbers.

3.1 Dual Polarization KIDs for BLAST-TNG

As the name suggests, BLAST-TNG is the next generation of the BLASTPol experiment, which produced polarization maps of many molecular clouds during two flights over Antarctica (Fissel et al. 2010). Targeting the same three observation bands as its predecessor, namely 30% bands centered on 250 μm (1.2 THz), 350 μm (857 GHz), and 500 μm (600 GHz), BLAST-TNG employs a 40% larger primary mirror and eight times the number of polarization-sensitive detectors, increasing the mapping speed by

a factor of 16 compared to its predecessor (Galitzki et al. 2014). Instead of bolometers, BLAST-TNG will employ horn coupled KID arrays with 859, 407, 201 pixels in the three bands ordered by increasing wavelength for a total of 2934 KIDs. BLAST-TNG will serve as a pathfinder instrument for dual-polarization KID technology when it flies over Antarctica in December of 2018. Our role at ASU is to design and optimize a dual-polarization absorber geometry scalable to all three bands. Both geometries we explore are designed to be front-illuminated and fabricated on a SOI substrate with its thin device side Si membrane ($\epsilon_r = 11.7$) defining the $\lambda/4$ backshort distance.

3.1.1 Optimization of Crossing Design

The first absorber design we explore is comprised of two sets of intersecting TiN lines that are sensitive to orthogonal polarizations. As shown in Fig. 5, we developed an HFSS parametric model for a 1.2 THz design that is scalable to the other two bands. We use the MATLAB-HFSS-API to sweep through the parameter space constrained by prior simulations and fabrication limitations to find the optimal parameter values that result in maximum co-pol coupling averaged over a 30% band centered on 1.2 THz (i.e., $1 - 1.4$ THz). We also want to minimize x-pol coupling, so we find the design exhibiting minimum x-pol by inspection. The optimal parameter values are given in Table 1 along with the dimensions we hold constant for this optimization. As shown in Fig. 6b, the optimal design exhibits 77.68% and 6.78% co-pol and x-pol coupling efficiencies, respectively. Fig. 6b also indicates that replacing the circular waveguide of radius $a = 90$ μm with the square waveguide of side length $s = 150$ μm, as illustrated in Fig. 6a, offers no appreciable improvement in coupling efficiency.

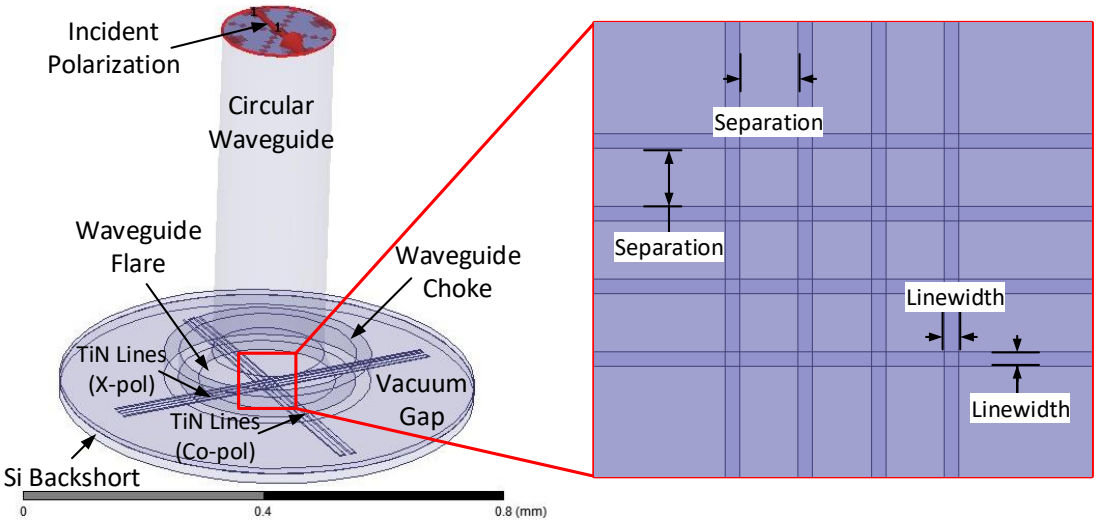

Figure 5: HFSS parametric model of crossing absorber design for BLAST-TNG KIDs with closeup view of two sets of intersecting TiN lines sensitive to orthogonal polarizations. The design employs SiO_x insulating crossovers to prevent the intersecting lines from shorting. Waveguide is flared before absorber for improved impedance match.

Table 1: Parameters and constants for optimizing crossing absorber design for BLAST-TNG KIDs.

Parameters	Optimal Value	Constants	Value
Number of Lines	4	Vacuum Gap (μm)	10
Line Width/Separation (μm)	4/16	Waveguide Radius (μm)	90
Backshort Thickness (μm)	18	Choke Inner Radius (μm)	150
TiN Sheet Impedance ($\Omega/\square$)	90	Choke Out Radius (μm)	175

Because we want to reduce the x-pol coupling to $< 3\%$, we revised our optimization problem by changing the objective to minimizing x-pol-to-co-pol coupling ratio. We also fix the Si backshort distance to 18 μm, choke inner radius to 164 μm, TiN sheet impedance to 90 $\Omega/\square$, and reduce the line width to 2 μm, which is the smallest feature size we can reliably produce with contact lithography in the ASU NanoFab. While all fabrication was ultimately done at the National Institute of Standards and

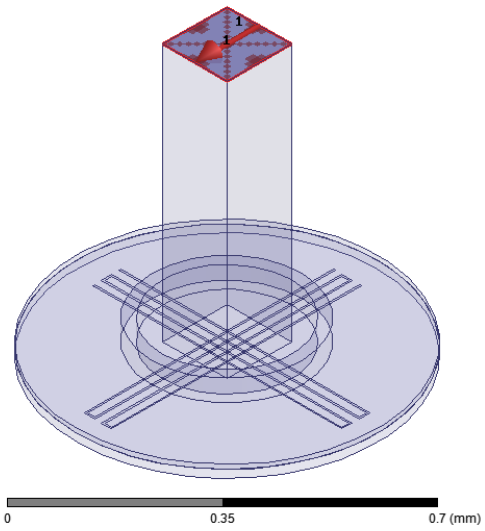

(a)

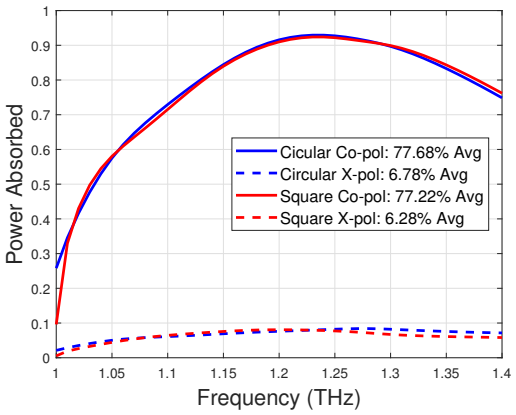

(b)

Figure 6: HFSS model of crossing absorber design for BLAST-TNG KIDs with square waveguide of side length 150 μm (a). Comparison of co-pol and x-pol performance between circular and square waveguide designs (b).

Technology (NIST), we had considered fabrication at ASU at the time. The revised parameter space is defined by line separation, waveguide radius, and choke thickness with optimal values given in Table 2. As shown in Fig. 7b, the optimal design exhibits 71.4% and 2.88% co-polar and x-polar coupling efficiencies, respectively, for a ratio of 0.04.

3.1.2 Optimization of Non-Crossing Design

The crossing absorber design requires insulating crossovers and superconducting bridges similar to those described in (Denis et al. 2017) to prevent the two polarizations from shorting to each other. To avoid this fabrication complication, we developed the

Table 2: Revised parameters and constants for optimizing crossing absorber design for BLAST-TNG KIDs.

Parameters	Optimal Value	Constants	Value
Separation	8	Line Width (μm)	2
Waveguide Radius (μm)	105	Backshort Thickness (μm)	18
Choke Thickness (μm)	35	Choke Inner Radius (μm)	164
		Vacuum Gap (μm)	10
		TiN Sheet Impedance ($\Omega/\square$)	90

non-crossing absorber geometry shown in Fig. 7a, which requires the three new design parameters listed in Table 3 to optimize. As shown in Fig. 7b, the optimal non-crossing design exhibits 70.45% and 2.42% co-polar and x-polar coupling efficiencies for a ratio of 0.034. Exhibiting similar performance to the crossing design, but requiring simpler fabrication, this non-crossing design was chosen for the absorber geometry of the horn coupled KIDs for BLAST-TNG. Our design was further optimized at NIST for a TiN/Ti multilayer film that the reduces the sheet resistance from 90 $\Omega/\square$ to 20 $\Omega/\square$, enabling a line width reduction by a factor of four, which minimizes x-pol coupling (Dober et al. 2016). Similar to single polarization TiN KIDs fabricated at NIST (Hubmayr et al. 2015), dual-polarization devices employing the optimized non-crossing absorber design demonstrate photon-limited noise performance under optical loads > 1 pW (Dober et al. 2016)

3.2 KIDs for Cosmic Microwave Background Studies

We are a main collaborator in an effort led by Columbia University to develop photon-limited, horn-coupled aluminum KIDs for cosmic microwave background (CMB)

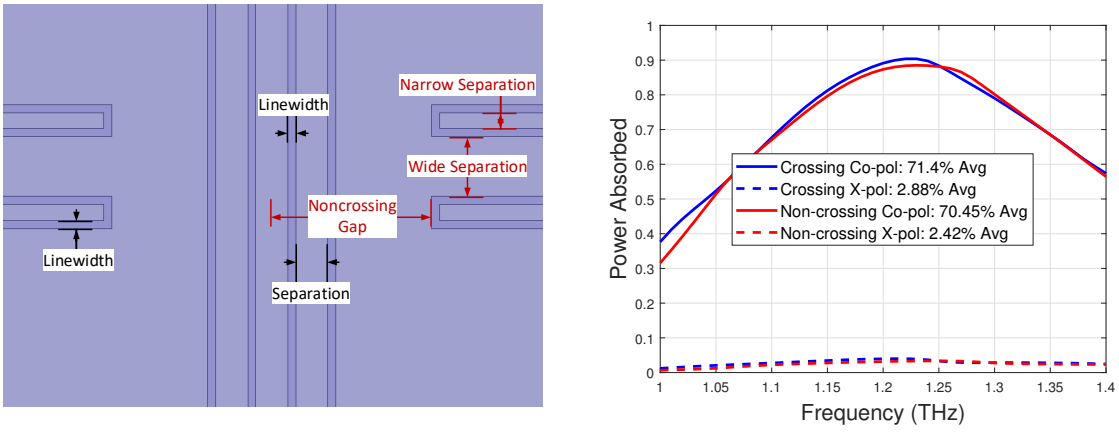

(a) (b)

Figure 7: Geometry of non-crossing absorber design for BLAST-TNG KIDs with new design parameters labeled in red (a). Comparison of co-pol and x-pol performance between crossing and non-crossing designs (b).

Table 3: Parameters and constants for optimizing non-crossing absorber design for BLAST-TNG KIDs. New design parameters are labeled in red in Fig. 7a.

Parameters	Optimal Value	Constants	Value
Noncrossing Gap (μm)	40	Line Width/Separation (μm)	2/8
Narrow Separation (μm)	2	Backshort Thickness (μm)	18
Wide Separation (μm)	20	Choke Inner Radius (μm)	164
		Choke Thickness (μm)	25
		Waveguide Radius (μm)	105
		Vacuum Gap (μm)	10
		TiN Sheet Impedance ($\Omega/\square$)	90

studies. These detectors operate in the 150 GHz band, which is where the CMB spectrum peaks. So far, there have been three detector designs: one single polarization design and two dual-polarization designs. We performed some initial simulations to design the single polarization KIDs, but our primary contribution to this effort has been device fabrication using the Arizona State University (ASU) NanoFab facilities. Fabricating millimeter-wave detectors for CMB studies had been exclusively under

the purview of government and university clean rooms, but (H McCarrick et al. 2014) demonstrated satisfactory performance of KIDs fabricated by Star Cryoelectronics, a private company. Our role at ASU is to prototype new designs and provide devices with designs identical to their commercially-fabricated counterparts for performance comparison.

3.2.1 Fabrication of Single Polarization Design

The mask layout for our single polarization KID design is shown in Fig. 8a. The detectors are sensitive to the polarization for which the electric field aligns with inductive absorbing lines. The layout, which is designed to be printed onto a 4 in. wafer, is comprised of five 20-element and four 9-element arrays of single polarization KIDs along with four witness samples for four-point probe measurements to characterize aluminum film properties. The KIDs are designed to be back-illuminated, which means incident photons first pass through the Si substrate before being absorbed by the inductive meander portion of the detector, and resonate at $100 - 200$ MHz, which is in the baseband of the readout system. All features are lithographically patterned in a 20 nm thick aluminum film deposited on a 300 μm thick high-resistivity Si wafer. See (H McCarrick et al. 2014) for details on optimizing KID absorber geometry for high optical efficiency, high responsivity, and low noise.

Fabricating these KIDs requires a single lithography step. It is worth noting that we use 4 in. high resistivity ($\rho > 1000\ \Omega\,\mathrm{cm}$) Si wafers that are 500 μm thick instead of the thinner 300 μm wafers used by Star Cryoelectronics for these single polarization KIDs. Our first step is to dip a new wafer into a 2-5% hydrofluoric acid (HF) solution to remove its native oxide, which is a main source of TLS noise. We then deposit

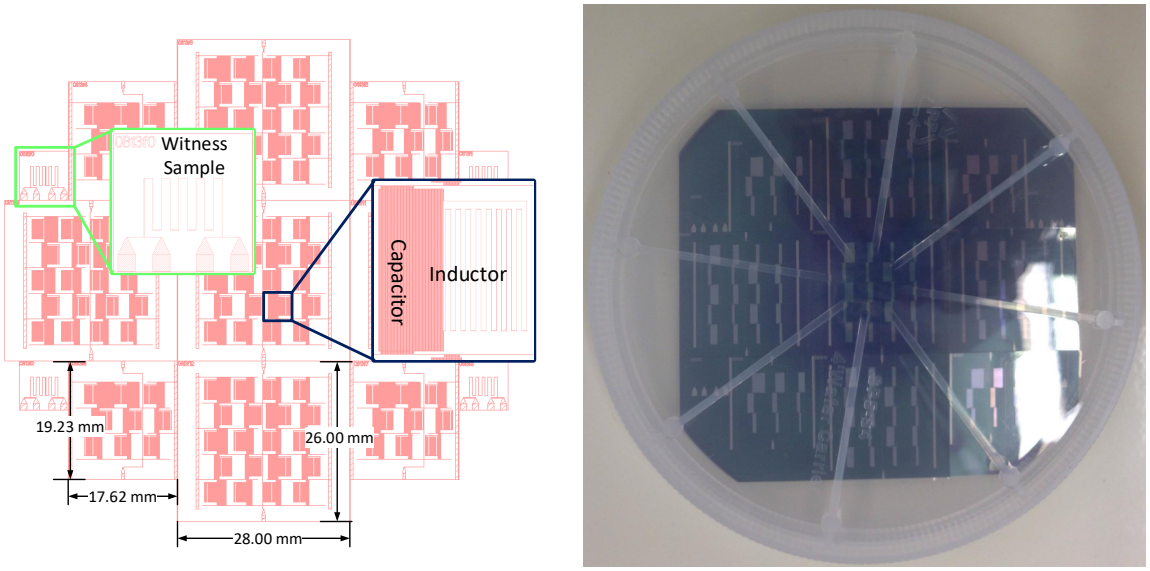

(a) (b)

Figure 8: Mask layout for single polarization aluminum KIDs designed to be patterned on 300 μm thick high-resistivity Si wafers with closeup views of single detector and witness sample for characterizing superconducting film properties (a). Photograph of completed wafer patterned using this mask layout (b).

a $20 - 40$ nm aluminum film over the entire wafer using electron beam (E-beam) evaporation, which is a physical vapor deposition (PVD) process. To protect the film from being attacked by our photoresist developer, we spin coat a $\sim$ 850 nm thick layer of PMMA over the aluminum before spinning on our AZ 3312 photoresist. After developing the pattern shown in Fig. 8a in the resist using AZ 300 MIF developer, we clean off the PMMA with a quick O_2 plasma ash before using reactive ion etching (RIE) with chlorine chemistry to define the KIDs arrays and witness samples in the aluminum film. Immediately after etching, passivate the ions embedded in the resist by immersing the wafer in deionized (DI) water to prevent unwanted etching of the aluminum underneath the resist. We clean off all remaining photoresist with a O_2 plasma ash and use a dicing saw to separate the die from the wafer. A fully diced

wafer still mounted on dicing tape is shown in Fig. 8b. See Appendix for the exact details of executing this fabrication process with the tool set in the ASU NanoFab.

The original plan was to perform the full suite of dark and optical measurements on at least one of our KID array chips at ASU to compare its performance to that of those fabricated by Star Cryoelectronics and tested in Columbia's cryogenic test system (Jones et al. 2015), we need sub-Kelvin cooling capability, for which development was shelved indefinitely until recently. Therefore, instead of testing the chips at ASU, we sent a few 20-element arrays to Columbia, where one was tested dark and shown to exhibit resonances as designed. Because the commercially-fabricated KIDs were an overwhelming success, achieving a 91% yield over multiple wafers, demonstrating the robustness and scalability of a novel multiplexing scheme, and exhibiting excellent noise performance with noise equivalent temperatures (NETs) $\sim 26 \pm 6\ \mu\mathrm{K}\sqrt{\mathrm{s}}$ referenced to a 4 K optical load (H McCarrick et al. 2014), we began to explore dual polarization designs instead of performing a full characterization of a single polarization chip fabricated at ASU. These single polarization KID arrays are the first ever to be fabricated at ASU and through this effort we have gained the expertise to complete a fabrication run for single-layer KIDs in a single workday. In addition to demonstrating the ability to fabricate KIDs at ASU, we have also gained significant insight into fabricating more complex superconducting circuits such as those described in Section 3.2.2 and Chapter 5. Once the sub-Kelvin stage of our cryostat is operational, these single polarization KIDs arrays will be one of the first devices we test.

3.2.2 Fabrication of Dual Polarization Design on SOI

Also targeting the 150 GHz band for CMB studies, two dual-polarization KID array designs, which are similar to those described by (Bryan et al. 2015), are shown in Fig. 9 and described in detail in (Heather McCarrick et al. 2016). Both chip layouts have twenty elements designed to be coupled to horns and two dark elements. Each element is comprised of two KIDs that are sensitive to orthogonal polarizations for a total of 44 KIDs on chip with each designed to resonate at $\sim$ 1 GHz. Because each element is a spatial pixel in the focal plane, dual-polarization designs double the number of detectors that fit into the same focal plane area compared to their single polarization counterparts. The layout in Fig. 9a is designed to be back-illuminated and patterned on a silicon-on-insulator (SOI) substrate with a 30 μm thick high-resistivity Si device layer. This architecture, hereinafter referred to as the SOI design, provides high optical efficiency over a wide bandwidth, but necessitates a complex fabrication process. In addition, using a thin Si membrane minimizes radiation propagating laterally in the dielectric substrate, thereby reducing optical crosstalk. The layout in Fig. 9b is designed to be front-illuminated and patterned on a 160 μm thick Si substrate, which itself sets the $\lambda/4$ backshort distance. With this architecture, hereinafter referred to as the thin Si design, we sacrifice some optical efficiency for a fabrication process requiring only a single lithography step similar to that for the single polarization design, but requiring increased care in handling the much thinner substrate. These chip designs are initial prototypes for a 271-element close-packed array with 542 KIDs for on-sky observation.

Star Cryoelectronics did not fabricate the SOI design because at the time of design,

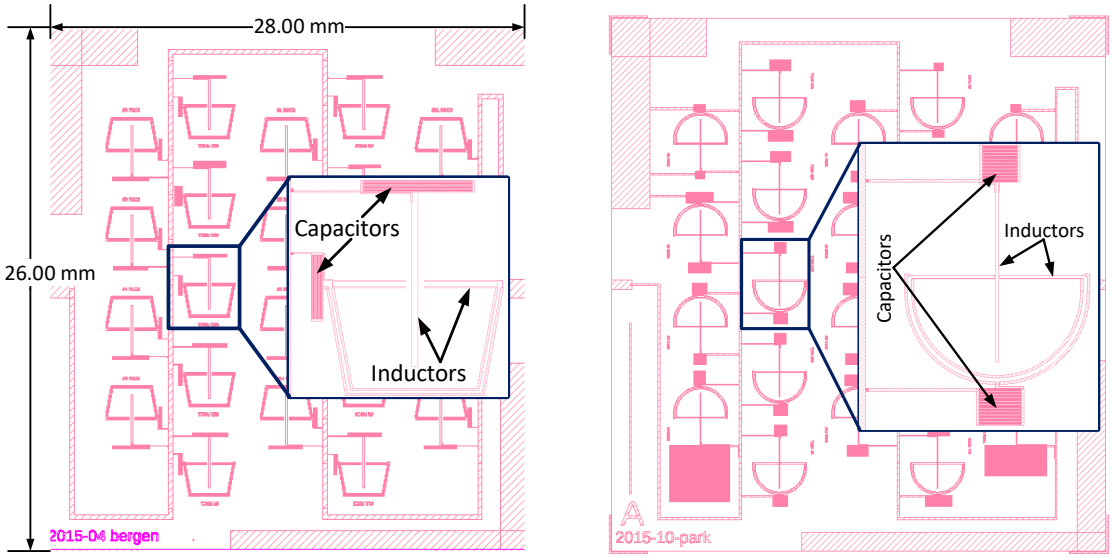

(a) (b)

Figure 9: Chip layouts for 20-element arrays of dual-polarization KIDs designed to be patterned on SOI (a) and 160 μm Si (b) substrates with closeup views of single pixels comprised of two single polarization KIDs each. The two additional pixels on chip are dark elements not coupled to horns and two chip layouts have identical dimensions.

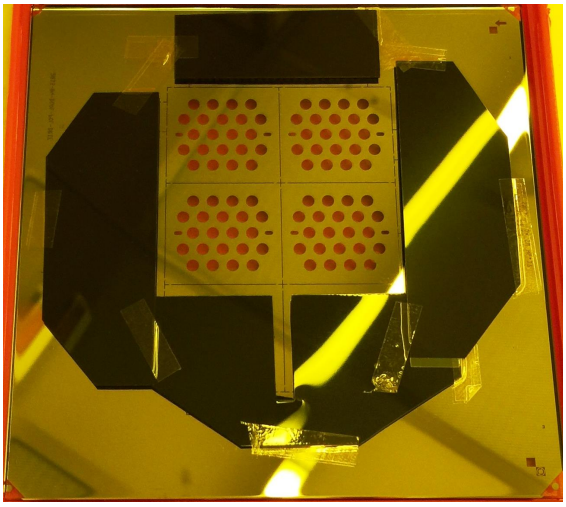

Figure 10: Handle side contact mask for dual polarization KIDs modified with emulsion film material to prevent exposure of features near edge of wafer. This modification reduces potential chip yield for single wafer from six to four.

the company lacked deep reactive ion etching (DRIE) capability, which is essential for processing the handle side of the SOI substrate. These arrays were simultaneously fabricated in the ASU NanoFab using contact lithography and Microdevices Laboratory at the Jet Propulsion Laboratory (JPL) using projection lithography. We describe our fabrication process for the dual-polarization design at ASU, which requires two lithography steps, one for each side of the SOI wafer. Because the device and handle side contact masks were designed at Columbia to fit the maximum number of chips on a 4 in. wafer, they were found to be incompatible with our DRIE tool in the ASU NanoFab. In particular, wafers need to be devoid of features in an annular region from the edge to ~ 10 mm inside the edge, where clamps affix the wafer to the chuck. Therefore, we obscure features that would be exposed into this exclusion region using opaque emulsion film material as shown in Fig. 10. Fortunately, this modified mask retains the necessary alignment keys for aligning the device and handle side patterns. In addition, the scribe grid is part of the handle side mask pattern because we need to use DRIE to separate the chips from the wafer. Dicing the wafer after DRIE would rupture the thin Si membranes on which the KIDs reside. The following describes the main steps in our fabrication process, which are illustrated in Fig. 11. All details for executing this process in the ASU NanoFab is provided in the Appendix.

I. Device Side Processing

1. Beginning with a SOI wafer comprised of a 30 μm high-resistivity device Si layer, 2 μm buried oxide layer, and 500 μm handle Si layer, dip the wafer into a 2-5% HF solution to remove its native oxide.
2. Using E-beam evaporation, deposit $20 - 40$ nm of aluminum on the device Si layer.

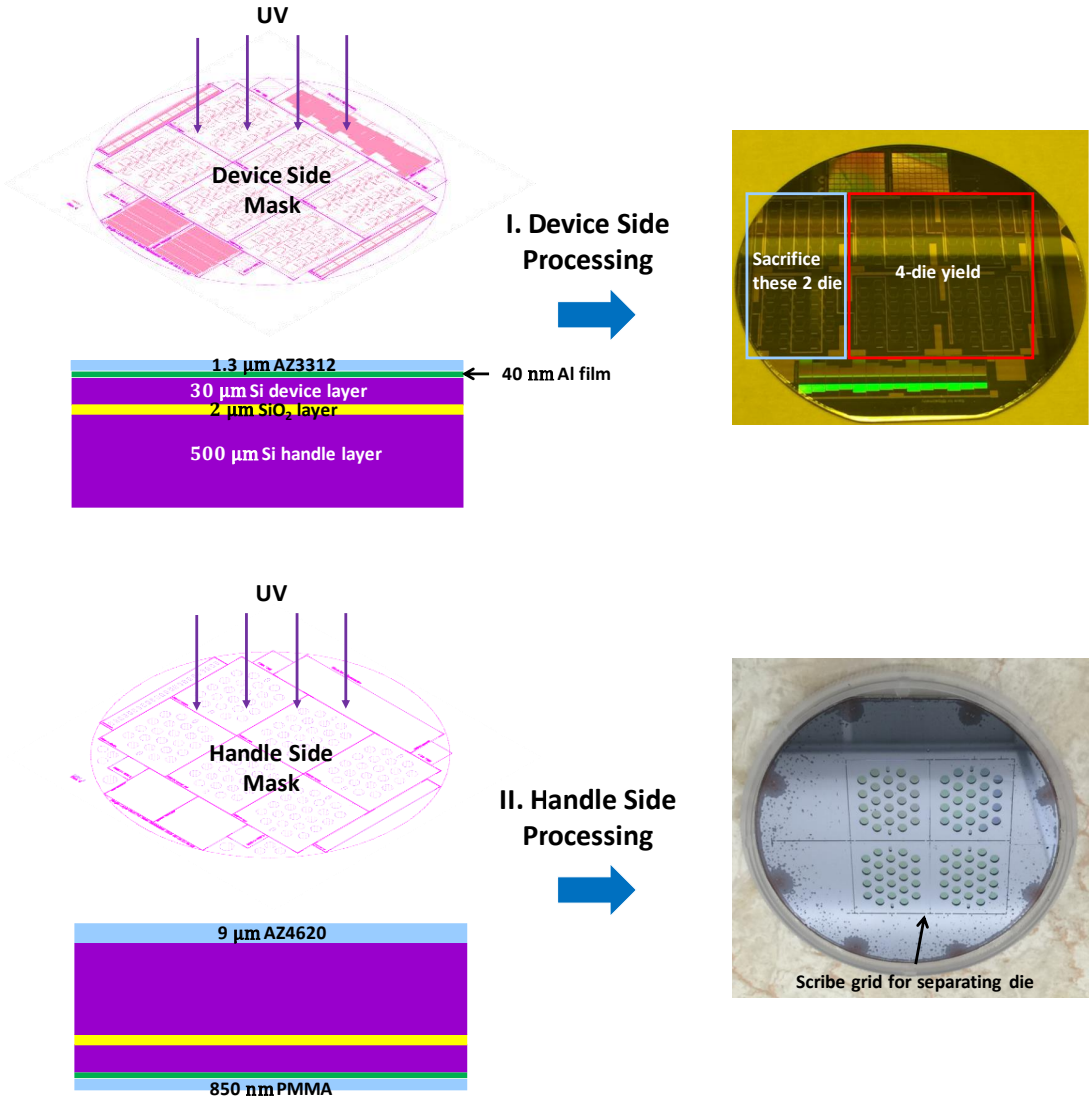

Figure 11: Fabrication process for dual-polarization KID arrays targeting the 150 GHz band designed to be patterned on SOI substrates.

3. Spin coat a $\sim$ 850 nm thick layer of PMMA over the aluminum to protect the film from being attacked by our developer.
4. Spin coat a $\sim$ 1.3 μm thick layer of AZ 3312 photoresist above the PMMA.
5. Using contact lithography, expose the device side mask pattern onto the AZ

3312 photoresist. This mask defines six chips of 20-element KID arrays in the area of a 4 in. wafer, but due to the aforementioned constraint imposed by our DRIE tool, each wafer effectively yields four chips as shown in Fig. 11. Since the mask chuck on our aligner is fixed, we shift the wafer chuck as far as possible to center these four chips on the wafer as much as possible.

6. After developing the device side pattern in the resist using AZ 300 MIF, punch through the exposed PMMA with a quick O_2 clean before using RIE with chlorine chemistry to define the dual-polarization KID arrays in the aluminum. Immediately after etching, passivate the ions embedded in the resist by immersing the wafer in DI water to prevent unwanted etching of the aluminum underneath the resist.
7. Clean off all remaining AZ 3312 with a long O_2 plasma ash and spin coat protective layer of PMMA over device side pattern to prevent damage to devices during handle side processing.

II. Handle Side Processing

1. Flip the wafer around and spin coat a ~ 9 μm layer of AZ 4620 photoresist onto the handle Si layer.
2. Using contact lithography, expose the handle side mask pattern onto the AZ 4620 photoresist. This mask defines the scribe grid for separating the chips from the wafer and hole pattern for etching away all of the handle Si and SiO_2 layers above each array element.
3. After developing the handle side pattern in the resist using AZ 300 MIF, mount the SOI wafer device side down on a carrier wafer using REVALPHA 90° C thermal release tape from Nitto. The carrier wafer is necessary for

structural support during DRIE and the tape will cleanly release when heated above 90° C.

4. Use Bosch DRIE to define the handle side pattern in the handle Si. This step, followed by a SiO_2 etch using fluorine chemistry, completely punches through 500 μm of handle Si and 2 μm of buried oxide to simultaneously place the KID arrays on a 30 μm Si membrane and separate the chips from the wafer.
5. Separate the etched SOI wafer from the carrier wafer by releasing the tape on a hot plate set to a few degrees above 90° C and remove all remaining AZ 4620 and PMMA on both sides of the wafer with a long O_2 plasma ash. Photographs of both device and handle side views of two completed chips are shown in Fig. 14.

Before fabricating on SOI, we first printed just the device side pattern on two 500 μm thick high resistivity Si wafers to characterize the behavior of the resonators shown in Fig. 9a. Star Cryoelectronics also made a few of these wafers for performance comparison. We measure a sheet resistance for our aluminum film to be $R_s \approx 5\ \Omega/\square$, which corresponds to a film thickness of $t \approx 7$ nm assuming a bulk resistivity of $\rho = 2.82 \times 10^{-8}\ \Omega\,\mathrm{m}$. The actual thickness is likely $\sim 12 - 15$ nm based on similar samples for NIKA (Mauskopf et al. 2014) , but still significantly thinner than the nominal 40 nm deposited during this fabrication run. Since we did not apply the protective PMMA layer during this fabrication run, we posit that our AZ 300 MIF developer attacked and thinned the film because we developed the photoresist for too long. Nevertheless, one ASU chip was packaged as shown in Fig. 12 and cooled down at Columbia. The critical temperature was found to be $\sim 1.50 \pm 0.01$ K, which agrees

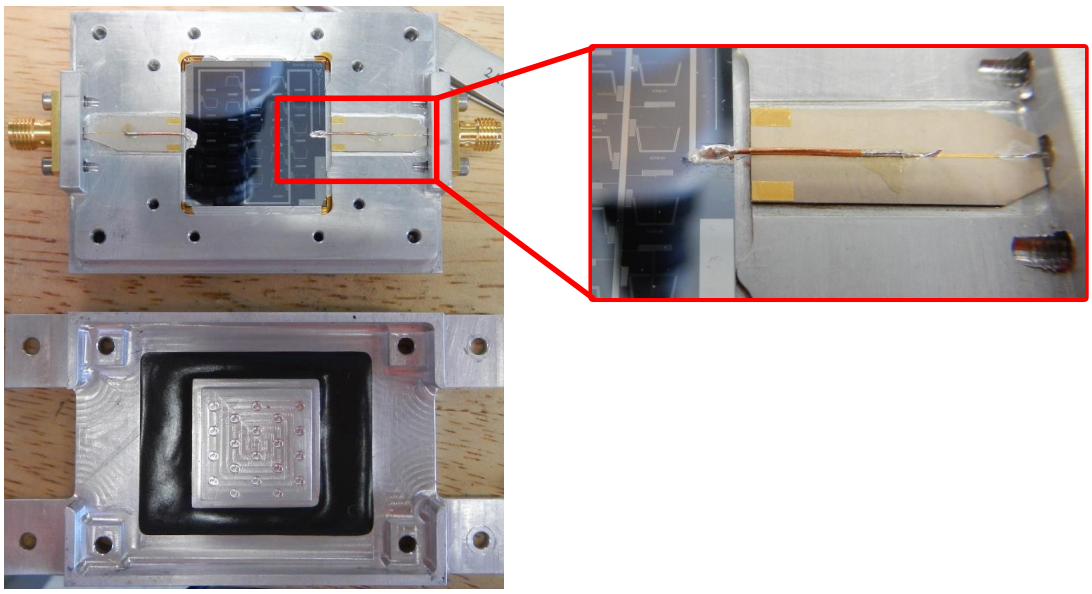

Figure 12: SOI design KID array fabricated on 500 μm Si substrate in its chip package with closeup view of interconnect between chip and package. Wire bonding is not possible due to thinner than normal film thickness, so interconnect is formed with soldered wire. Horn array apertures are blocked for dark testing.

with the measured aluminum film properties for NIKA chips. As shown in Fig. 13a, the measured internal quality factors for the KIDs on this chip are $10000 < Q_i < 60000$, which is an order of magnitude lower compared to those for the single polarization KIDs made by Star Cryoelectronics. Fig. 13b shows similarly low Q_i values for a chip fabricated at Star Cryoelectronics with the same design. However, both of these chips exhibit decent optical response and noise performance, so we proceeded to a full fabrication run on a SOI wafer.

During the fabrication run yielding the chips shown in Fig. 14, we included a glass witness sample in the E-beam evaporation chamber with the SOI wafer. We measured a film thickness of 43.8 nm on the witness sample. The critical temperature for one of these chips was found to be $T_c \approx 1.45$ K when cooled down for testing at

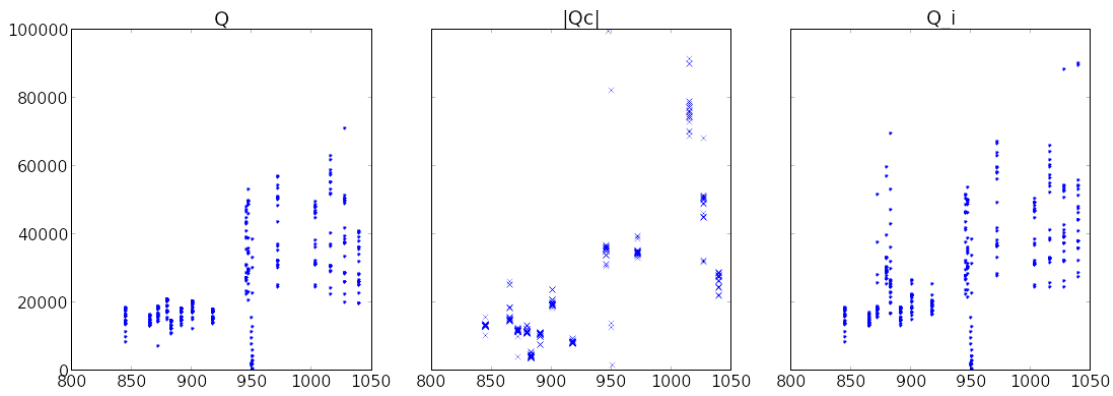

(a)

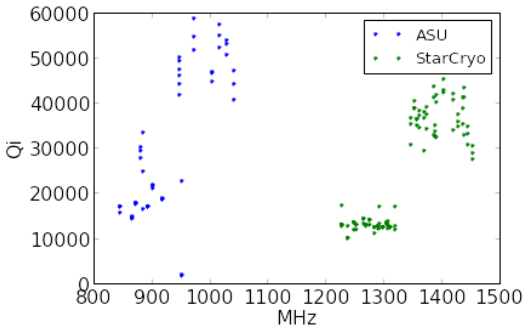

(b)

Figure 13: Measured Q_{res}, Q_c, and Q_i for prototype of SOI design fabricated on 500 μm thick Si at ASU (a). Comparison of measured Q_i for ASU chip to that for Star Cryoelectronics chip with same design (b). Horizontal axes for all plots are Frequency in MHz. Plots produced by Glenn Jones at Columbia University.

Columbia, but no resonances were observed. Upon closer inspection, we discovered that defects in the film comparable in size to the critical dimension, which is the 2 μm line width of the KID inductor, open-circuited every pixel. After processing a few test samples to troubleshoot this issue, we discovered that ions embedded in the photoresist during the aluminum etch attacked the metal underneath the resist from the sidewalls inward. These defects had not yet formed when we performed optical inspections during processing. To avoid these defects, we immerse the wafer in DI

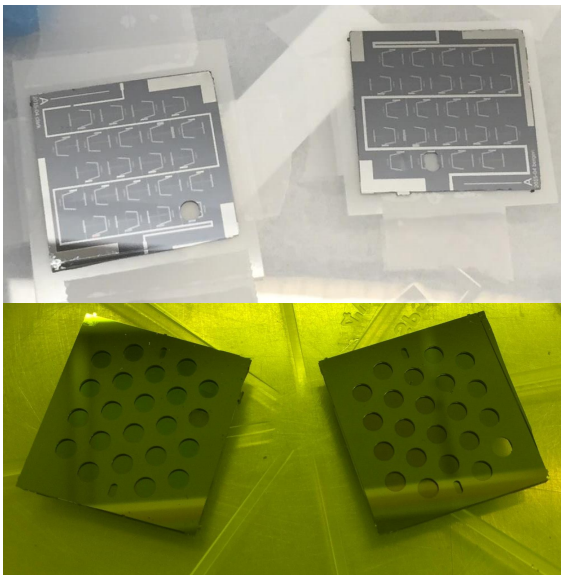

Figure 14: Photographs of device-side (top) and handle-side (bottom) views of two completed 20-element array chips of dual-polarization KIDs on SOI substrates.

water immediately after the aluminum etch. In addition only two of four chips on this wafer survived because instead of PMMA, we used AZ 4260 as the device side protective layer, which comes in contact with the thermal release tape when mounted on the carrier wafer for DRIE. When we attempted to release the tape at 105° C to demount the SOI wafer, this resist reflowed and seemingly reacted with the tape adhesive to prevent release. Attempting to demount with mechanical force completely fractured two chips and destroyed a single array element on each surviving chip. The hard bake step for PMMA is done at 180° C, so there is no chance of reflow at release temperatures for our 90° C thermal release tape. All subsequent fabrication employing PMMA as the protective layer to adhere to our tape has resulted in clean release and demount. Due to promising results presented in (Heather McCarrick et al. 2016), this SOI design was shelved in favor of the 160 μm thin Si design before we fabricated any more dual-polarization KID arrays on SOI at ASU. We have developed a reliable process to fabricate not only these KID arrays, but also other devices requiring SOI

substrates and DRIE in the ASU NanoFab. We apply a slightly modified version of this process to fabricate the W-Band phase shifter circuit to be described in Chapter 5.

3.2.3 Fabrication of Dual Polarization Design on Thin Si

The fabrication process for the thin Si design is identical to that described in Section 3.2.1 with the exception of the contact mask. In addition, the wafers we use are only 160 μm thick, so we use soft tip, non-scratch tweezers to handle them. The Microdevices Laboratory at JPL fabricated these devices with 40 nm film thickness, which is the value optimized for maximum optical efficiency for this design. Similar to the SOI design prototypes fabricated on thick Si substrates, JPL's first fabrication run yielded devices exhibiting Q_i values significantly lower than expected. To probe the reason for low Q_i values, we fabricated the thin Si design using a thicker 100 nm film thickness at ASU in order to test the hypothesis that low inductor volume limits Q_i to low values. We measured the sheet resistance to be 0.7 $\Omega/\square$, which is twice that of the chips JPL subsequently made with 100 nm film thickness. Dark tests performed at JPL on their chips yielded internal quality factors $\sim 10^6$ while loading the same chips with a 3 K blackbody reduces Q_i to $\sim 10^4$, which is still high enough to multiplex the 542 detectors of a full array in 500 MHz of bandwidth (Heather McCarrick et al. 2016). The measured NET values for representative detectors in each polarization are 36 $\mu\mathrm{K}\sqrt{\mathrm{s}}$ and 52 $\mu\mathrm{K}\sqrt{\mathrm{s}}$ referenced to a 4 K optical load (Heather McCarrick et al. 2016). Retaining the 160 μm Si substrate, this dual-polarization design has been further optimized and expanded into a 64-element array with $Q_i = 3 \times 10^5$ and NET < 100 $\mu\mathrm{K}/\sqrt{\mathrm{s}}$ under a 3.4 K blackbody load, crosstalk below -20 dB, high polarization selectivity, and photon-limited performance above 1 pW of absorbed

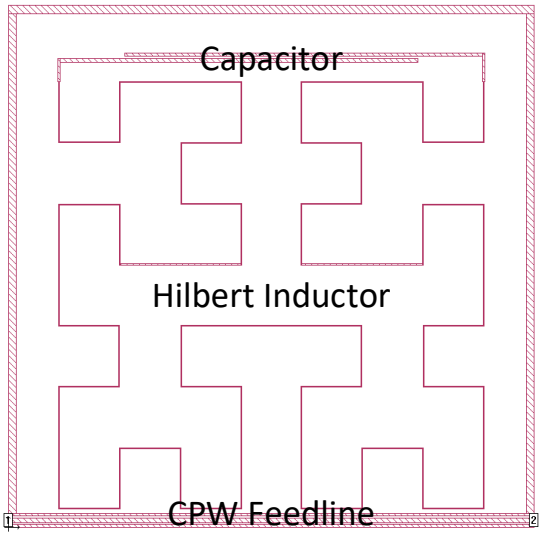

Figure 15

power (H. McCarrick et al. 2017), demonstrating its capability for on-sky CMB polarimetry.

3.2.4 Hilbert Design for OLIMPO

OLIMPO is a balloon-borne telescope designed to study the CMB in four bands centered on 150 GHz, 220 GHz, 350 GHz, 500 GHz (Coppolecchia et al. 2013). An effort was made to replace existing horn coupled TESs with KIDs in time for a summer 2016 flight. We provided an HFSS parametric model similar to those described in Section 3.1 for a KID design comprised of an interdigital capacitor in parallel with a third order Hilbert fractal-shaped inductor as shown in Fig. 15. This is a proven design (Mauskopf et al. 2014) that can be scaled to all four target bands.

3.3 Summary

We have made significant contributions to two large scale efforts to develop horn-coupled KID arrays for astronomical observations in the millimeter regime and assumed a minor role in a third. For BLAST-TNG, we developed a parametric HFSS model and used it to optimize two dual-polarization KID absorber geometries for lowest x-pol-to-co-pol coupling ratio. One of these optimized designs was adapted to a multilayer TiN/Ti film architecture that reduced sheet impedance by a factor of four, which is expected to further reduce x-pol coupling. Devices fabricated at NIST for this design demonstrate $< 3\%$ x-pol coupling and photon-limited noise performance when under > 1 pW of optical loading (Dober et al. 2016). For the Columbia University-led effort to demonstrate similar horn-coupled dual-polarization KIDs on-sky for CMB studies, we developed reliable fabrication processes for three different KID array architectures to run in the ASU NanoFab and delivered chips for all three designs, the first KIDs ever made at ASU. Because we do not yet have sub-Kelvin cooling capability at ASU, only a few of these chips have been tested at Columbia, but they are ready for testing as soon as our sub-Kelvin stage is operational. We provided a parametric model similar to that for BLAST-TNG, to the OLIMPO team to facilitate optimization of a KID design with a Hilbert fractal absorber geometry.

Chapter 4

FILTER BANK SPECTROMETERS

4.1 Millimeter-Wave Spectrometer Taxonomy

As described in Chapter 1, advancements in spectrometer technology are essential to making progress in millimeter(mm)-wave astronomy. There are two types of astronomical spectrometers operating in this regime: heterodyne and direct detection. Heterodyne instruments rely on coherent detection, which preserves both the amplitude and phase of an incident signal from the sky. The main advantage of this technology is its high achievable spectral resolution of $\mathcal{R} > 10^6$, but coherent detection exhibits a fundamental sensitivity limit due to the uncertainty principle that is not present in direct detection instruments. In addition, heterodyne instruments generally have smaller fields of view and narrower instantaneous bandwidths than their direct detection counterparts. Therefore, state-of-the-art heterodyne receivers such as those for the Atacama Large Millimeter Array (ALMA) shown in Fig. 16, are excellent for performing detailed studies of individual sources, but not suitable for survey spectroscopy over large areas of the sky. It is worth noting that recent efforts are paving the way to realize $\sim$ 1000 pixel arrays of heterodyne receivers that are suitable for mapping $\sim$ 100 deg^2 areas of the sky (Wheeler 2016).

Unlike coherent detection, direct detection, which only senses signal power, is fundamentally limited in sensitivity by photon noise. Direct detection spectrometers are further classified according to:

Figure 16: Photographs of ALMA antennas (left) and Band 1 heterodyne receiver (right) covering $35 - 50$ GHz from (Malin 2012) and (Morata and Huang 2017), respectively.

i. the medium in which the incident broadband signal propagates

ii. the method by which spectral components are separated.

For the redshift (z) and Early Universe Spectrometer (ZEUS) shown in Fig. 17a, broadband light propagates in free space before encountering an echelle grating that separates its spectral components to be detected by a 32-pixel linear array of Si bolometers (Steven Hailey-Dunsheath 2009). Targeting the 350 μm and 450 μm atmospheric windows, which are 15% bands, ZEUS achieves $\mathcal{R} = 550 - 1600$ and produced the first ever detection of the ^{13}CO $(6 \rightarrow 5)$ line from a galaxy outside of the local group (Steven Hailey-Dunsheath 2009; Hailey-Dunsheath et al. 2008). Targeting the full 1 mm atmospheric window, Z-Spec, shown in Fig. 17b, employs a waveguide as the medium for broadband light propagation and Rowland grating to separate its spectral components to be detected by 160 horn coupled SiN bolometers (Bradford

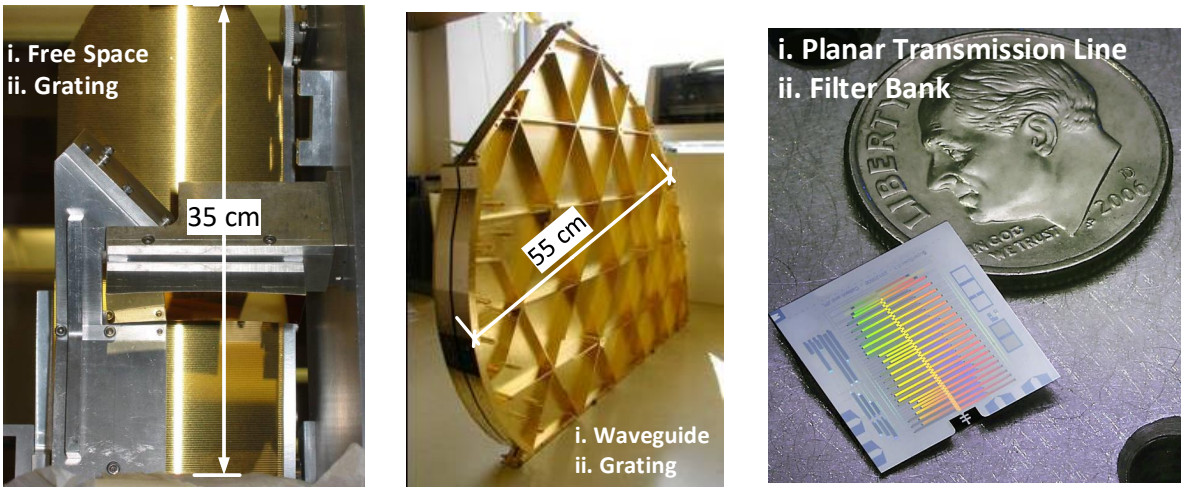

(a) (b) (c)

Figure 17: Photographs of direct detection spectrometers ZEUS (a), Z-Spec (b), and SuperSpec (c) from (Steven Hailey-Dunsheath 2009), (Bradford et al. 2004), and (McGeehan et al. 2017), respectively. Instruments further classified by i. medium in which broadband light propagates and ii. method by which spectral components are separated.

et al. 2004). Because the physical spacing between adjacent slits in a grating is on the order of λ, achieving even moderate spectral resolution requires a physically large grating at these wavelengths. Given the sizes of ZEUS and Z-Spec indicated in Figs. 17a and 17b, grating spectrometers for mm-wave astronomy are limited to at most a few spatial pixels. Dramatic miniaturization is necessary to enable large focal plane arrays for survey spectroscopy.

Covering an instantaneous bandwidth of 70% or more in the $100-500$ GHz range, SuperSpec is a novel mm-wave astronomical spectrometer technology designed to perform broadband spectral surveys of the high-redshift universe over large areas of the sky. We present a microwave network model we developed to characterize the performance and inform the design of progressively larger prototypes on our way to a ~ 300 channel filter bank covering the entire $190-310$ GHz atmospheric window for our

first on-sky demonstration. We validate our model against full-wave electromagnetic simulations and apply it to our latest 50 channel prototype to accurately extract values for key performance metrics actually exhibited by the device, which deviate significantly from their design values.

4.2 Lumped Element Microwave Network Model for SuperSpec

An emerging spectrometer technology for mm-wave astronomy, SuperSpec is designed to provide the requisite resolution ($\mathcal{R} \sim 300$), bandwidth ($\sim 1:1.7$), and sensitivity (NEP $< 10^{-17}$ W/$\sqrt{\text{Hz}}$) to enable thorough investigation of star formation and galaxy evolution during the Epoch of Reionization through survey spectroscopy of high-redshift galaxies (Wheeler et al. 2016; Hailey-Dunsheath et al. 2014; Barry 2014). Existing grating spectrometers (Stacey et al. 2007; Steven Hailey-Dunsheath 2009; Ferkinhoff et al. 2010; Earle et al. 2006) and heterodyne interferometers (Testi 2009) are well-suited for studying individual galaxies, but respectively lack the architecture and bandwidth required to conduct broadband surveys over large areas of the sky, which are necessary to observe a statistically large sample of these galaxies. As shown in Fig. 17c, SuperSpec integrates a broadband transmission line filter bank and hundreds of inherently multiplexable kinetic inductance detectors (KIDs) on a single chip only ~ 1 cm^2 in size, enabling construction of powerful, multi-pixel, focal-plane spectrometer arrays. We are currently developing this technology for ground-based observations in the $190 - 310$ GHz atmospheric window.

For recent designs (Hailey-Dunsheath et al. 2016; Wheeler et al. 2017), a lens-coupled antenna receives a broadband signal from the sky, which then propagates down a microstrip feedline and encounters a series of spectral channels implemented

as $\lambda_i/2$ resonant filters, where λ_i is the center wavelength of the spectral component accepted by the i^{th} channel. Each staple-shaped[2] filter is gap-coupled to both the feedline and a KID with tunable coupling strengths determined by the sizes of these gaps and described by Q_{feed} and Q_{det}, respectively. Accounting for dielectric loss with Q_{loss}, we control the spectrometer resolving power $\mathcal{R}$ according to

$$\frac{1}{\mathcal{R}} = \frac{1}{Q_{\text{ch}}} = \frac{1}{Q_{\text{feed}}} + \frac{1}{Q_{\text{det}}} + \frac{1}{Q_{\text{loss}}}. \tag{4.1}$$

To assemble a filter bank, channels are ordered monotonically decreasing in frequency with adjacent channels having logarithmic frequency spacing and an odd multiple of $\lambda_i/4$ physical spacing.

Fig. 18 summarizes our latest SuperSpec prototype (Wheeler et al. 2017; McGeehan et al. 2017), a 50 channel subset of a ~ 300 channel filter bank covering the entire $190 - 310$ GHz atmospheric window we are developing for on-sky deployment. A full-wave electromagnetic (EM) simulator such as Sonnet is an excellent tool for understanding a single spectral channel or small filter bank with $\lesssim 10$ channels, but it becomes prohibitively memory intensive to perform full-wave analysis on larger devices. To fully understand recent prototype measurements on our way to developing an optimized filter bank for scientific use, we have developed a microwave network model capable of simulating the EM effects needed to capture the performance of a full filter bank with accuracy comparable to full-wave analysis in less than a minute of computation time on a typical workstation. This model serves as a general purpose tool to evaluate all future SuperSpec devices and inform subsequent designs. We present our model and insights gleaned from its application to recent measurements.

[2]Each $\lambda/2$ resonator is bent into a staple to facilitate coupling to the KID and reduce radiation loss (Barry et al. 2012)

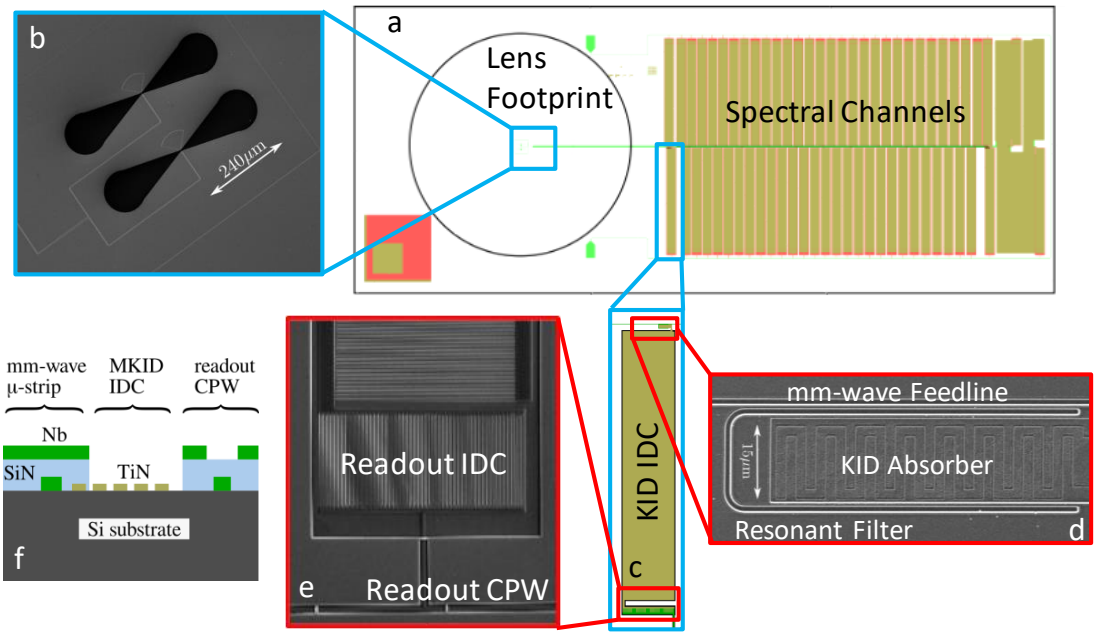

Figure 18: Latest 50-channel SuperSpec prototype architecture. Mask layout (a) with closeups on a bowtie antenna (b), single channel with KID (c), mm-wave $\lambda/2$ resonator (d), and KID readout geometry (e). Chip cross-section (f).

4.2.1 Model Overview

The required number of channels to sample a frequency band $f_l < f < f_u$ with resolving power $\mathcal{R}$ and spectral oversampling factor Σ, which is defined as the ratio of channel bandwidth to the center frequency separation of adjacent channels, is

$$N_{\rm ch} = \Sigma \mathcal{R} \ln\left(\frac{f_u}{f_l}\right). \tag{4.2}$$

Starting at f_u, each subsequent channel frequency $f_{\rm r}$ is scaled from its predecessor by the factor

$$x = \exp\left[-\frac{\ln f_u - \ln f_l}{N_{\rm ch} - 1}\right]. \tag{4.3}$$

Caltech's SuperMix code provided initial proof-of-concept for these log-spaced filter banks (Kovács et al. 2012) and we have designed all prototypes using analytic expres-

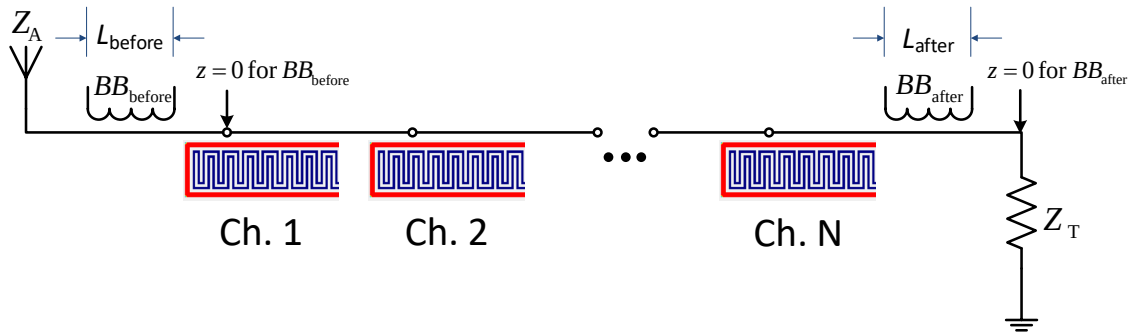

(a)

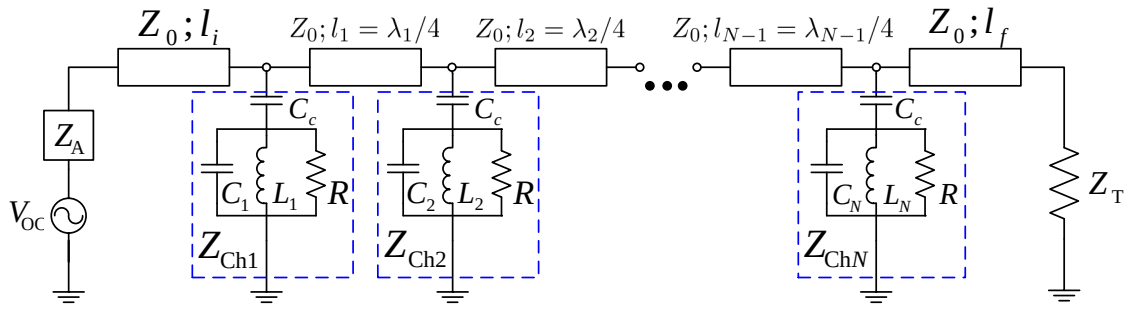

(b)

Figure 19: Block diagram (a) and transmission line (b) representations of our model for SuperSpec filter banks. Block diagram shows effective single point of coupling to be approximately 1/3 of the length along each distributed resonator.

sions combined with full-wave Sonnet simulations to map design parameters f_r, Q_{feed}, Q_{det} to physical dimensions on chip, assuming isolated channels with ideal Lorentzian response (Barry et al. 2012; Shiu 2015). As evidenced by discrepancies between measured and design values of these parameters (Wheeler et al. 2016), channels within filter banks exhibit non-Lorentzian response due to crosstalk.

The filter bank block diagram in Fig. 19a shows the spectral channels bracketed by two diagnostic broadband channels to measure power at two key positions along the feedline. A broadband receiving antenna with impedance Z_A and absorber with impedance Z_T feeds and terminates the feedline, respectively. In Fig. 19b, we describe

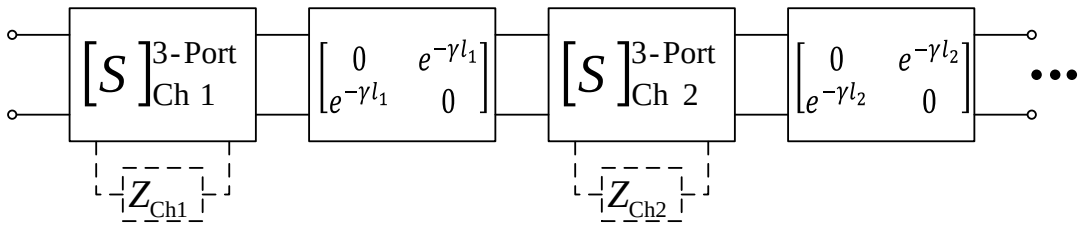

Figure 20: Cascaded Network Representation for SuperSpec Model

the filter bank with a lossy transmission line model that treats each $\lambda/2$ resonator as a lumped element tank circuit coupled to the feedline through a coupling capacitor. We have implemented this model in MATLAB and IDL using ABCD matrix formalism and Python using its scikit-rf module. This section focuses on the final and most detailed implementation, which captures channel crosstalk, EM loss, and potential impedance mismatches to provide a high-fidelity representation of real filter bank behavior. A full version of the code for this Python implementation is given in Appendix A.

4.2.2 Spectral Channels

Both the MATLAB and IDL implementations treat each spectral channel as a 2-port network of a shunt impedance equal to the total impedance of its tank circuit representation, namely

$$\begin{aligned} Z_{\mathrm{ch}}(\omega) &= \frac{1}{j\omega C_c} + \frac{1}{R + j\omega L + \dfrac{1}{j\omega C}} \\ &\simeq \frac{Z_0 Q_{\mathrm{feed}}}{2}\left(\frac{1}{Q_{\mathrm{det}}} + \frac{1}{Q_{\mathrm{loss}}}\right) + jZ_0 Q_{\mathrm{feed}} x \end{aligned} \tag{4.4}$$

where Z_0 is the feedline's characteristic impedance and $x = (\omega - \omega_{\mathrm{r}})/\omega_{\mathrm{r}}$ is the fractional detuning of the resonator. As shown in Fig. 20, our implementation treats

each channel as a 3-port network with S-matrix $[S]^{3-\text{port}}_{\text{Ch1}}$, $[S]^{3-\text{port}}_{\text{Ch2}}$, etc. and all ports shorted together, but referenced to different impedances. We implement this using scikit-rf by creating a 3-port network with S-matrix

$$[S]^{3-\text{port}} = \begin{bmatrix} -\frac{1}{3} & \frac{2}{3} & \frac{2}{3} \\ \frac{2}{3} & \frac{1}{3} & \frac{2}{3} \\ \frac{2}{3} & \frac{2}{3} & -\frac{1}{3} \end{bmatrix} \tag{4.5}$$

and renormalizing the port impedances to Z_0 for ports 1 and 3, which connect to the rest of the filter bank, and Z_{ch} from Eq. 4.4 for port 2. Our 3-port approach is equivalent to the 2-port approach, but provides ports to directly access each channel's response once the filter bank is assembled.

4.2.3 Filter Bank Assembly

As shown in Fig. 20, we construct a full filter bank by cascading a series of 3-port and 2-port networks representing its constituent spectral channels and their interconnecting transmission lines, respectively, using scikit-rf's connect function identical to the approach in (Bryan et al. 2015). We describe transmission line loss with $\tan\delta = Q^{-1}_{\text{loss}}$ because the feedline and resonant filters are microstrip with the same inner layer dielectric. Each section of feedline between adjacent channels is an odd multiple of $\lambda/4$ in length where λ is the resonant wavelength of the channel closer to the antenna. Feedline sections preceding the first channel and following the final channel have lengths greater than the center wavelength of the target band. While the antenna and termination are designed to be matched to the feedline, fabrication errors may result in mismatches, so Z_{A} and Z_{T} are free parameters in our model. When fully assembled, a filter bank is a $(N_{\text{ch}} + 2)$-port scikit-rf network object with port 1

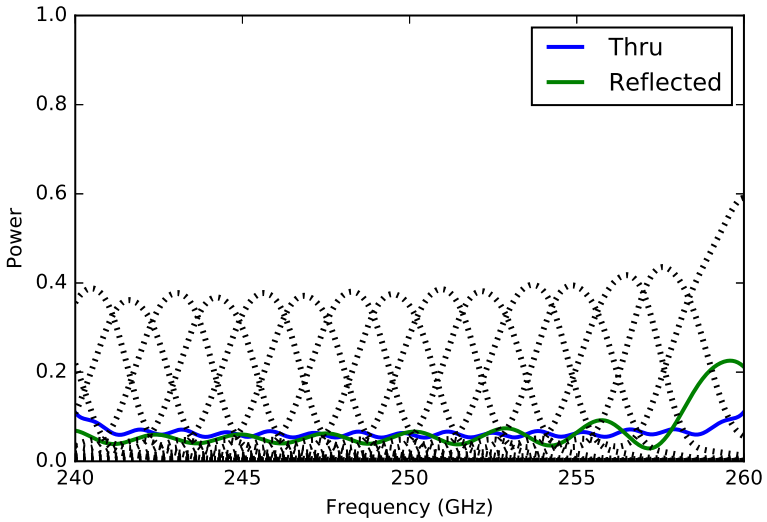

(a)

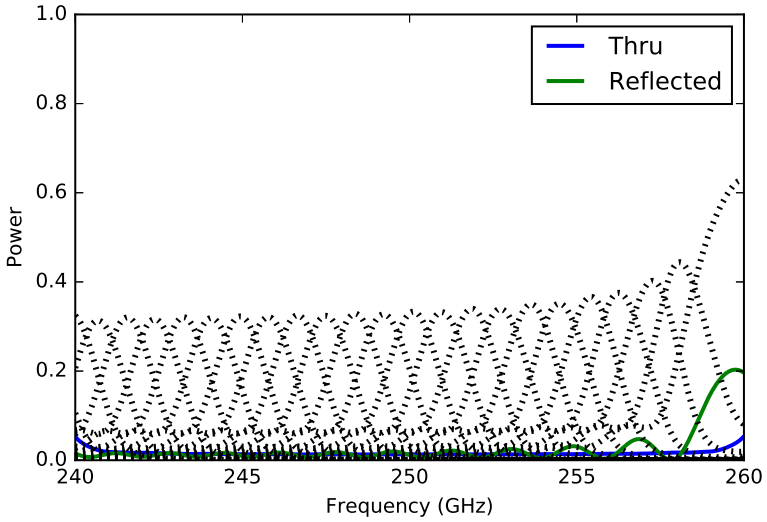

(b)

Figure 21: Through, reflected, and channel response (dotted traces) for log-spaced filter banks with $\Sigma = 2$ (a) and $\Sigma = 3$ (b) computed by our model. For both filter banks, $Z_{\mathrm{A}} = Z_0 = Z_{\mathrm{T}}$.

(input) referenced to Z_{A}, port $N_{\mathrm{ch}} + 2$ (termination) referenced to Z_{T}, and ports 2 to $N_{\mathrm{ch}} + 1$ (spectral channels) referenced to their respective channel impedances.

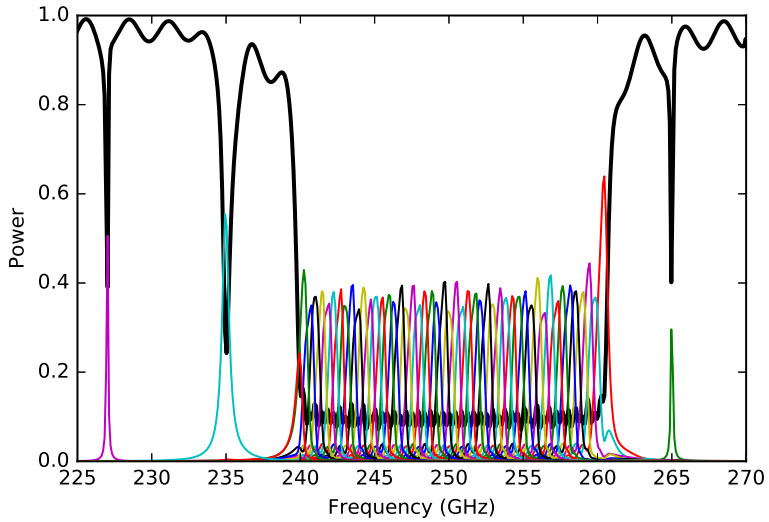

Figure 22: Through power (black) and response of each channel (other colors) for 55-channel filter bank with $Z_0 = 37.58\ \Omega$, $Z_\mathrm{A} = 30\ \Omega$, and $Z_\mathrm{T} = 50\ \Omega$ computed by our model.

To demonstrate the basic functionality of our Python implementation, we compute the through power, reflected power, and channel response for three log-spaced filter banks. Fig. 21 compares the behavior of filter banks covering $240 - 260$ GHz with $\Sigma = 2$ and $\Sigma = 3$. All channels for both filter banks are designed for $Q_\mathrm{feed} = Q_\mathrm{det} = 200$ and channel frequencies are determined by Eqs. 4.2 and 4.3. As expected, the highest frequency channel in each filter bank is significantly more efficient than all other channels. With logarithmic frequency spacing, the peak efficiency for each individual channel except the highest frequency channel decreases with increasing Σ, but the average efficiency across the band increases due to closer frequency spacing. The overall filter bank behavior matches that from Caltech's SuperMix code (Kovács et al. 2012) and the MATLAB implementation (Shiu 2015). Computed by our model, the response for a 55-channel filter bank design is shown in Fig. 22. This design, which has been fabricated and tested at Caltech, has 50 $\Sigma = 3$ log-spaced channels between

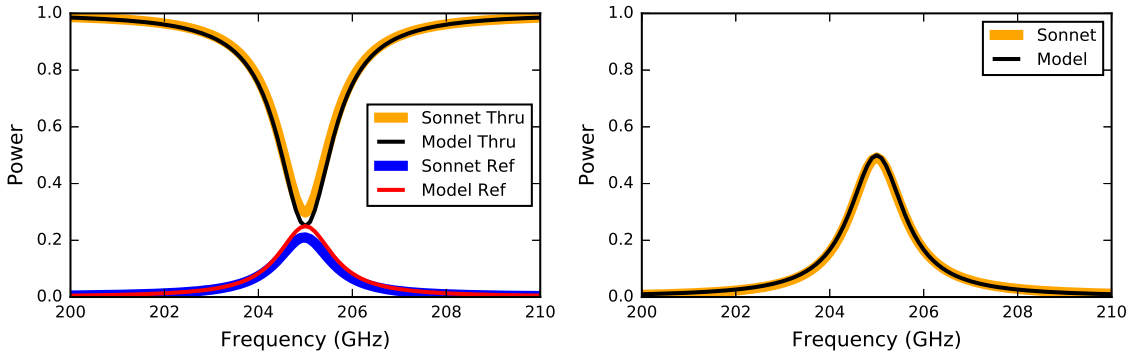

Figure 23: Our model compared to Sonnet simulation for single spectral channel designed for $f_r = 205$ GHz and $Q_{\text{feed}} = Q_{\text{det}} = 290$. Through and reflected power (left) and channel response (right).

$240 - 260$ GHz and five isolated channels outside this band. The log-spaced channels exhibit the aforementioned behavior as expected. We see that within a filter bank, even the isolated channels deviate from ideal Lorentzian behavior due to crosstalk among channels. Thus, the response of each channel in a filter bank depends not only on its own parameters, but also those of all other channels. With $Z_0 = 37.58\ \Omega$, we set $Z_{\text{A}} = 30\ \Omega$ and $Z_{\text{T}} = 50\ \Omega$ to demonstrate our model's capability of handling antenna and termination mismatches. The out-of-band standing wave pattern in the through power trace captures these mismatches.

Figs. 23, 24, and Fig. 26 validate our model against full-wave Sonnet simulations for a single channel with $f_r = 205$ GHz, 5-channel filter bank with channels well-separated in frequency, and 6-channel filter bank with $\Sigma = 3$, respectively, all of which are lossless. The channels in the 6-channel filter bank are designed to have the same $\mathcal{R}$, be well-matched, namely $Q_{\text{det}} = Q_{\text{feed}} = 295$, and admit spectral bands centered on frequencies given in the first row of Table 4. For real filter banks, coupling between the feedline and each channel is distributed along the length of its $\lambda/2$ resonator,

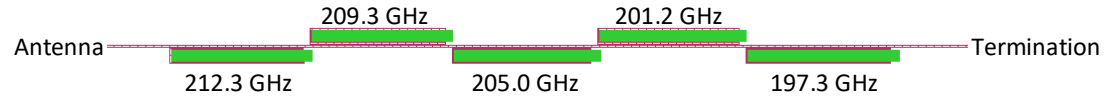

(a)

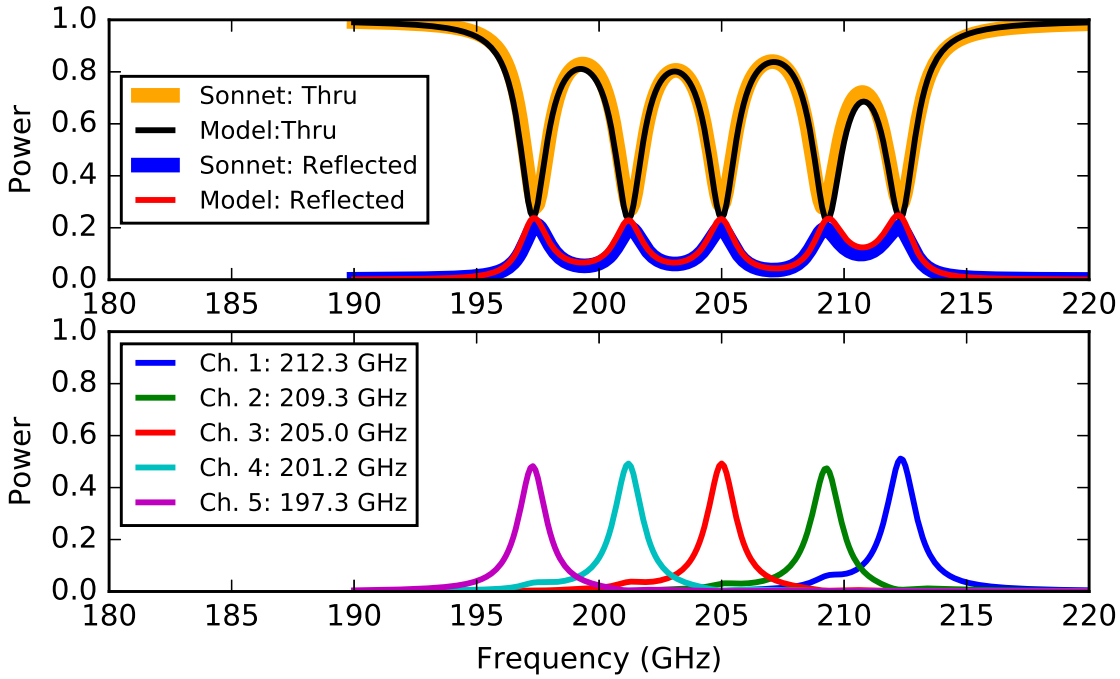

(b)

Figure 24: Our model compared to Sonnet simulation for filter bank with five well-separated channels. Sonnet geometry for filter bank labeled with design values for channel frequencies (a). Plots of model against Sonnet for through and reflected power (b, top) and model channel response (b, bottom).

but our lumped element representation models capacitive coupling at a single point. In addition, our microstrip geometry allows for the possibility of direct coupling between channels, which is not captured by the model. As shown in Fig. 23, there is a small discrepancy between our model and Sonnet, which simulates distributed coupling, for the through and reflected power of a single isolated channel, but strong overall agreement between the two methods indicates that our tank circuit is a valid

Figure 25: Sonnet geometry for 6-channel log-spaced filter bank labeled with design values for channel frequencies

representation of a distributed $\lambda/2$ resonator. This is further corroborated by the strong agreement between our model and Sonnet for the filter bank with five channels well-separated in frequency shown in Fig. 24a. As shown in the top panel of Fig. 24b, plotting our model against Sonnet for through and reflected power for this 5-channel device exhibits the same minor discrepancies as those for the single channel, but our model reproduces the overall response of full wave analysis with reasonable accuracy. With multiple channels, we see that even though channel frequencies are reasonably well separated, the response of each channel deviates from that of the single isolated channel due to cross talk among channels. In particular, we see that each channel exhibits noticeable response at the center frequency of its immediate neighbor as shown in the bottom panel of Fig. 24b. As the frequency spacing between channels is decreased, we expect an increase in the effects of cross talk on channel response.

The geometry of our 6-channel log-spaced filter bank is shown in Fig. 25. While a single channel exhibits Lorentzian response, log-spaced channels deviate significantly from this behavior due to crosstalk as shown in Fig. 26. For the Sonnet simulation, we apply the method from (Shiu 2015) to extract each channel's response from current density information. With both channel response and through power for full-wave analysis, we use SciPy's curve_fit function to fit our model to Sonnet for the entire filter bank. The initial guess and fit result values for the nine free parameters are listed

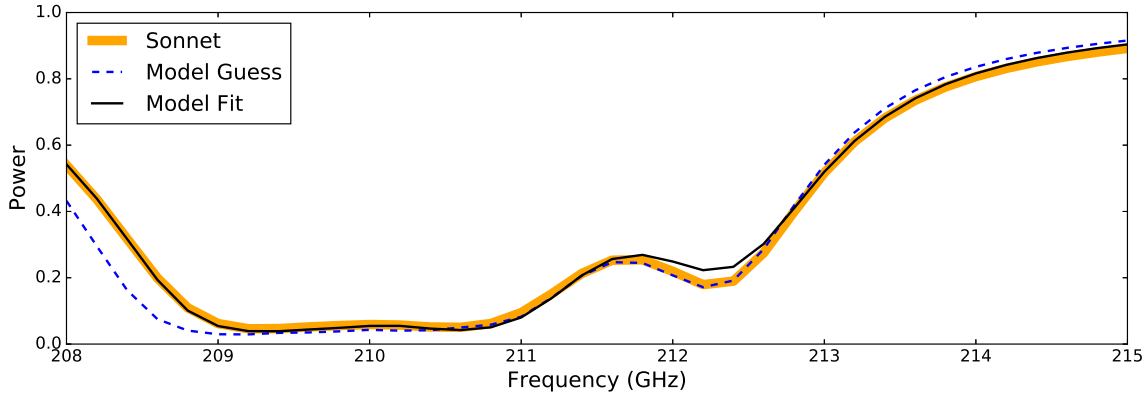

(a)

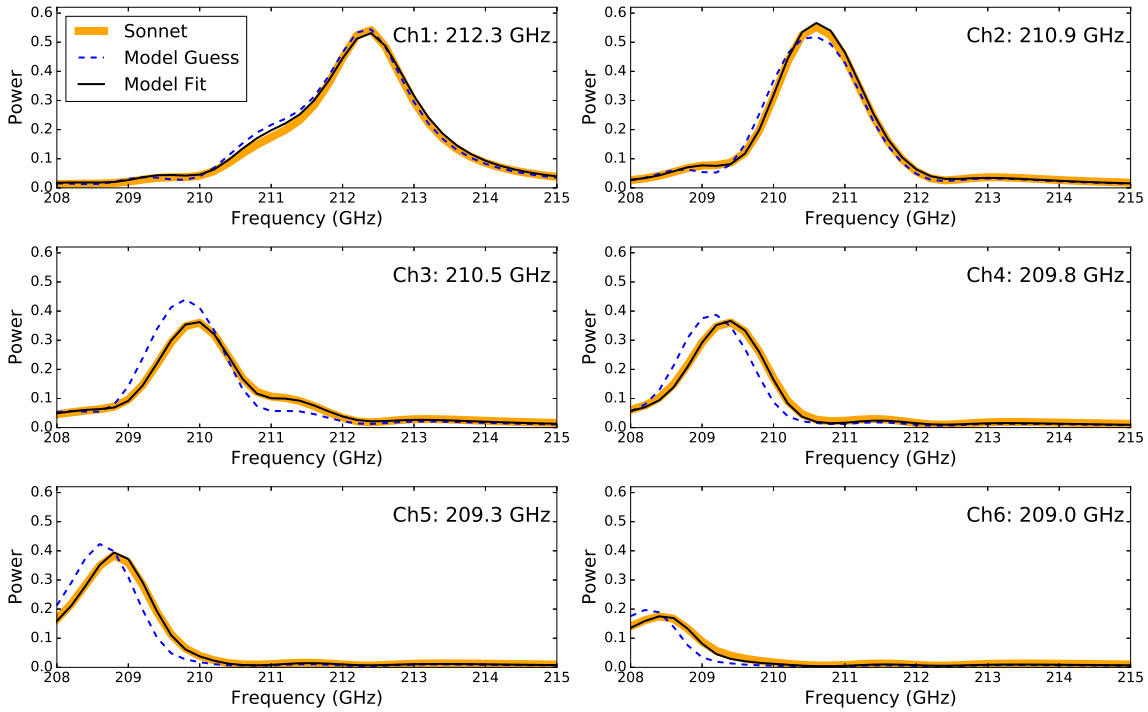

(b)

Figure 26: Our model compared to Sonnet simulation for filter bank with six log-spaced ($\Sigma = 3$) channels. Plots of initial model guess and model fit against Sonnet for through power (a) and channel response (b).

in the second and third rows of Table 4, respectively. Plotting our model fit against Sonnet for through power and channel response in Figs. 26a and 26b, respectively, demonstrates the ability of our model to accurately fit all features of full-wave analysis

with the exception of some deviation in the through power around 212.5 GHz. From fit results, we see that full-wave analysis of a log-spaced filter bank indicates channels with $Q_{\text{feed}} \neq Q_{\text{det}}$ and center frequencies shifted downward from their design values. Our model is able to capture the complex interactions among channels that produce these effects, achieving accuracy comparable to full-wave analysis and providing a robust tool to extract actual achieved values of f_r, Q_{feed}, and Q_{det} from data. In addition, accurate reproduction of full-wave analysis by our model suggests minimal direct coupling between channels while (Shiu 2015) found the effective single point of coupling to model distributed coupling to be approximately 1/3 of the length along the horizontal section of each staple as illustrated in Fig. 19a.

4.2.4 Broadband Channels

We need to calculate the response of the broadband channels analytically because our model only tracks power at the ports. The broadband channel before the spectral channels is sensitive to the voltage wave

$$V(z) = V_0^+ \left(e^{-\gamma z} + \Gamma e^{\gamma z}\right) \tag{4.6}$$

on the leading section of feedline of length l_i, where $\gamma = \alpha + j\beta$ is the complex propagation constant, $z = 0$ is at the position of the first spectral channel as shown in Fig. 19a, and V_0^+ and Γ are the incident wave and reflection coefficient at $z = 0$, respectively. We construct a filter bank network excluding the antenna and leading transmission line, so that its S_{11} represents the load for a terminated transmission line problem to determine $V(z)$. Illustrated in Fig. 19b, the generator is our antenna with impedance Z_{A} and source V_{oc}, the open circuit voltage between its terminals. To obtain the response of this broadband channel, BB_{before}, we average $V(z)\,V^*(z)$ over

its coupling length L_{before}. Using Eq. 4.6, we obtain

$$\begin{aligned} V(z)\,V^*(z) &= \left|V_0^+\right|^2 \left[e^{-(\alpha+j\beta)} + S_{11}e^{(\alpha+j\beta)}\right]\left[e^{-(\alpha-j\beta)} + S_{11}^* e^{(\alpha-j\beta)}\right] \\ &= \left|V_0^+\right|^2 \left[e^{-2\alpha z} + S_{11}^* e^{-2j\beta z} + S_{11}e^{2j\beta z} + |S_{11}|^2 e^{2\alpha z}\right] \\ &= \left|V_0^+\right|^2 \left[e^{-2\alpha z} + 2\,|S_{11}|\cos(2\beta z + \theta) + |S_{11}|^2 e^{2\alpha z}\right], \end{aligned} \tag{4.7}$$

where $\Gamma = S_{11} = |S_{11}|\,e^{j\theta}$. Therefore, the response of the broadband channel is

$$\begin{aligned} BB_{\text{before}} &= \frac{\epsilon_{\text{before}}}{L_{\text{before}}} \int_{z_c - L_{\text{before}}/2}^{z_c + L_{\text{before}}/2} V(z)\,V^*(z)\,dz \\ &= \epsilon_{\text{before}} \left|V_0^+\right|^2 [\text{sinc}\,(j\alpha L_{\text{before}})\,e^{-2\alpha z_c} \\ &\quad + |S_{11}|\cos(2\beta z_c + \theta)\,\text{sinc}\,(\beta L_{\text{before}}) + |S_{11}|^2\,\text{sinc}\,(j\alpha L_{\text{before}})\,e^{2\alpha z_c}], \end{aligned} \tag{4.8}$$

where ϵ_{before} and z_c are its coupling efficiency to the feedline and center position, respectively, and

$$V_0^+ = \frac{Z_{\text{in}}}{Z_{\text{in}} + Z_{\text{A}}} \frac{V_{\text{oc}}}{e^{\gamma l_i} + S_{11}e^{-\gamma l_i}} \tag{4.9}$$

with Z_{in} the input impedance at $z = -l_i$ looking toward the load.

For a filter bank network including the antenna and termination, the voltage at the termination is $S_{21}V_{\text{oc}}$, so the voltage wave on the feedline section of length l_f after the final channel is

$$V(z) = S_{21}V_{\text{oc}}e^{-\gamma z}, \tag{4.10}$$

where $z = 0$ is now defined to be at the position of the termination as shown in Fig. 19a. Therefore, the response of the broadband channel after the spectral channels is

$$BB_{\text{after}} = \frac{\epsilon_{\text{after}}\,|S_{21}|^2\,|V_{\text{oc}}|^2}{L_{\text{after}}} \int_{z_c - L_{\text{after}}/2}^{z_c + L_{\text{after}}/2} e^{-2\alpha z} dz \tag{4.11}$$

$$= \epsilon_{\text{after}}\,|S_{21}|^2\,|V_{\text{oc}}|^2\,\text{sinc}\,(j\alpha L_{\text{after}})\,e^{-2\alpha z_c} \tag{4.12}$$

where ϵ_{after}, z_c, and L_{after} are its coupling efficiency, center position, and coupling length, respectively.

4.3 SuperSpec Model Applications

4.3.1 Fits to Measurements

For maximum coupling on-resonance, channels are individually designed to be well-matched, but fabrication variance from chip to chip combined with channel crosstalk unpredictably alters the actual Q_{feed}, Q_{det}, and f_r achieved by real filter banks from their design values. We need to be able to measure achieved Q_{feed}, Q_{det}, and f_r to evaluate performance and optimize future devices. For current prototypes, we can determine Q_{det}, Q_{feed}, and f_r by fitting an ideal Lorentzian to isolated channels such as the lowest frequency channel shown in the top panel of Fig. 27, but for a full size filter bank, the entire target bandwidth is filled with log-spaced channels and thus devoid of any unused frequency space to fit isolated channels. As shown in Section 4.2.3, the response of a channel in a log-spaced filter bank depends not only on its own parameters, but also every other channel. Thus, we need to fit the entire filter bank at once to obtain accurate values for Q_{feed}, Q_{det}, and f_r exhibited by the device.

Using curve_fit, we fit our model to measured channel response data for a 50-channel prototype of design described in Fig. 18. For this device, we observed no out-of-band standing waves, so we perform the fit assuming $Z_{\mathrm{A}} = Z_0 = Z_{\mathrm{T}}$. Also assuming $\epsilon_{\mathrm{before}} = \epsilon_{\mathrm{after}}$, the 54 free parameters for this fit are broadband channel efficiency, Q_{feed}, Q_{det}, Q_{loss}, and the 50 channel frequencies. Shown in the bottom left panel of Fig. 27, we perform an additional fit for $BB_{\mathrm{after}}/BB_{\mathrm{before}}$, which measures total power coupled off the feedline, to help constrain Q_{loss}, an important parameter due to significant EM loss evidenced by out-of-band deviation from unity of measured

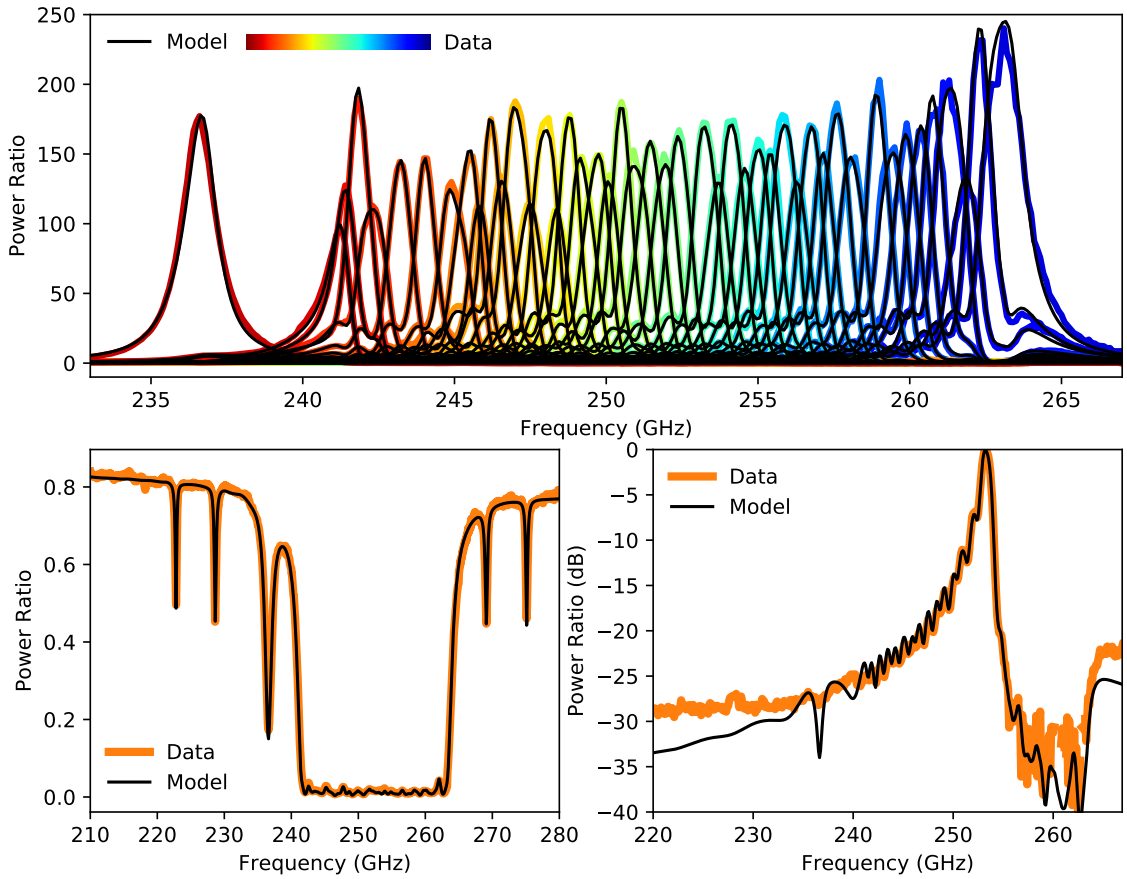

Figure 27: Model applied to measurements on prototype filter bank with design described in Fig. 18. Measured data and model fit to spectral channels normalized by $BB_{\rm before}$ (top). Measured data and fit for $BB_{\rm after}/BB_{\rm before}$ (bottom left). Measured data and fit for single spectral channel in middle of filter bank normalized by $BB_{\rm before}$ (bottom right).

$BB_{\rm after}/BB_{\rm before}$. Small variations in f_r for each channel causes the variation in peak response seen in the top panel of Fig. 27. This fit, the first ever for a full filter bank with all channels fit simultaneously, yields $Q_{\rm feed} = 415$ (designed 462), $Q_{\rm det} = 685$ (designed 800), and $Q_{\rm loss} = 1260$. As shown for a channel in the middle of the filter bank (bottom right panel of Fig. 27), our model does not reproduce the evident direct coupling between the KID and feedline at the -30 dB level well out-of-band. Similar

to our lumped element approach's inability to perfectly model distributed coupling, this is another limitation of our model.

4.3.2 Sensitivity Optimization

To optimize a ~ 300 channel filter bank for highest sensitivity, we use our model to compute instrument noise equivalent power (NEP) as a function of the design parameters Q_{feed}, Q_{det}, and Σ along with estimated Q_{loss} and measured detector sensitivity $\mathrm{NEP}_{\mathrm{KID}}$. For SuperSpec, we modify the expression for photon noise given in Eq. 2.80 to

$$\mathrm{NEP}_{\mathrm{ph}}^2 = 2 \int_{f_l}^{f_u} (hf)^2 \, n\,(f)\,[2 + n\,(f)]\, df, \tag{4.13}$$

where the 2 in square brackets accounts for equal contributions from shot and recombination noise and $N_{\mathrm{pol}} = N_{\mathrm{mode}}$=1. The occupation number in the detector is

$$n\,(f) = \epsilon\,(f)\,\eta\,(f)\,n_0\,(f) = \frac{\epsilon\,(f)\,\eta\,(f)}{e^{hf/k_B T_{\mathrm{sky}}} - 1}, \tag{4.14}$$

where $\eta\,(f)$ is the channel optical efficiency computed as the product of our system efficiency from cryostat window to filter bank input, namely $\eta_{\mathrm{sys}} = 0.5$, and channel efficiency referenced to filter bank input, which is computed by our model. To compute the occupation number in the source n_0, we assume an on-sky source with temperature $T_{\mathrm{sky}} = 260$ K and emissivity $\epsilon = 0.1$. To obtain the total NEP for each channel, we sum its photon noise and detector contributions in quadrature, namely

$$\mathrm{NEP}_{\mathrm{ch,\,abs}}^2 = \mathrm{NEP}_{\mathrm{ph}}^2 + \mathrm{NEP}_{\mathrm{KID}}^2, \tag{4.15}$$

which is referenced to absorbed power. The NEP referenced to power incident on the cryostat window is $\mathrm{NEP}_{\mathrm{ch}} = \mathrm{NEP}_{\mathrm{ch,\,abs}}/\eta\,(f)$. Every channel contributes some NEP

at every frequency in band, so the total sensitivity to a given frequency is the sum of the contributions from all channels. We sum these contributions in reciprocal to obtain the instrument NEP to be

$$\frac{1}{\mathrm{NEP}^2_{\mathrm{inst}}} = \sum_{i=1}^{N_{\mathrm{ch}}} \frac{1}{\mathrm{NEP}^2_{\mathrm{ch,\,i}}}. \tag{4.16}$$

The final step is to average $\mathrm{NEP}_{\mathrm{inst}}$ over the target band.

Sweeps over a large range of parameter values using the IDL implementation of our model have yielded an optimized design for the first full size filter bank for SuperSpec, which is currently being fabricated at JPL (Steven Hailey-Dunsheath 2016, 2017). Estimating the loss to be $Q_{\mathrm{loss}} = 1000$ and using the most recent (and best) measured detector sensitivity of $\mathrm{NEP}_{\mathrm{KID}} = 3 \times 10^{-18}$ W/$\sqrt{\mathrm{Hz}}$ (Wheeler et al. 2017), the parameter values to achieve the best instrument sensitivity are $Q_{\mathrm{feed}} \approx 500$, $Q_{\mathrm{det}}/Q_{\mathrm{feed}} = 0.94$, and $\Sigma = 2$ yielding $\mathrm{NEP}_{\mathrm{inst,\,avg}} \approx 4 \times 10^{-17}$ W/$\sqrt{\mathrm{Hz}}$ (Steven Hailey-Dunsheath 2017). Additional design iterations will be needed to hone in on a device for on-sky demonstration, so applying our Python implementation in tandem with the IDL implementation a provides a robust tool for sensitivity optimization.

4.4 Waveguide Filter Bank Spectrometer

For SuperSpec, the filter bank circuit is implemented in planar transmission line. With precision machining, we can also implement the same circuit in rectangular waveguide. We have designed, fabricated, and characterized a 5-channel prototype spectrometer pixel operating in W-Band to demonstrate this novel moderate-resolution ($\mathcal{R} \sim 50 - 250$), multi-pixel, broadband, spectrometer concept for mm-wave astronomy. Our design implements a transmission line filter bank using waveguide resonant cavities as a series of narrow-band filters, each coupled to an aluminum kinetic inductance

detector (KID). This technology has the potential to perform the next generation of spectroscopic observations needed to drastically improve our understanding of the epoch of reionization (EoR), star formation, and large-scale structure of the universe. We present our design concept, results from measurements on our prototype device, and the latest progress on our efforts to develop a 4-pixel demonstrator instrument operating in the $130 - 250$ GHz band.

Technological advancements in imaging and spectroscopy in the mm and submm-wave regimes have revolutionized the fields of observational cosmology and extragalactic astronomy. The Atacama Large Millimeter Array (ALMA), a product of these advancements, is currently performing spectroscopic measurements at resolutions and sensitivities much higher than those ever previously attainable (Testi 2009) . While ALMA is a superb tool for performing high-resolution imaging and spectroscopy on individual sources, it would be prohibitively time-consuming to use it for wide-band spectral surveys over large areas of the sky. Requiring only moderate spectral resolution ($\mathcal{R} \sim 50 - 200$), such surveys are vitally important to the challenging next steps in mm-wave imaging and spectroscopy, which aim to characterize the large-scale structure and star formation history of the universe using CO and CII intensity mapping and perform high angular resolution observations of the hot gas in galaxy clusters using the Sunyaev-Zel'dovich (SZ) effect.

The current state of the art in mm-wave spectroscopy is Z-Spec (Earle et al. 2006), a single-pixel grating-type spectrometer that achieves $\mathcal{R} \sim 300$. There are also substantial ongoing efforts to develop ultra-compact on-chip spectrometers such as SuperSpec and DESHIMA (Endo et al. 2012) based on lithographically-patterned superconducting filter banks coupled to large arrays of KIDs. We are developing a scalable multi-pixel waveguide spectrometer (WSpec) that implements filter banks

using rectangular waveguide resonant cavities instead of lithography for horn-coupled imaging spectroscopy using KIDs. The spectrometer pixels, which can be warm and cold tested independently from the detector arrays, are fabricated with standard precision machining tools.

WSpec is a highly complementary technology to on-chip designs in several ways:

1. Our WSpec demonstrator instrument targets the relatively unexplored $130 - 250$ GHz band, which is suitable for CO line emission and kinetic SZ studies.
2. WSpec is designed for lower spectral resolution than the superconducting spectrometers.
3. WSpec may be used as a room-temperature backend for cryogenic amplifiers, removing the need for down-converting mixers.
4. Because WSpec operates reasonably well at room temperature, the technology, which is still compact, has the potential to be used for earth observing and planetary science missions.

4.4.1 Design Concept

The design of a single waveguide spectrometer pixel is illustrated in the top panel of Fig. 28, which shows an HFSS drawing of our 5-channel prototype filter bank. A feed horn couples light from the sky into the main waveguide. Each channel connects to the main waveguide through an evanescent coupling section into a $\lambda/2$ resonant cavity, the electrical length of which defines the center frequency of the channel. An identical coupling section on the other side of the resonator connects to another section of waveguide, which is terminated by an aluminum KID. H-plane and E-plane closeup views of a single channel are shown in the top and bottom panels

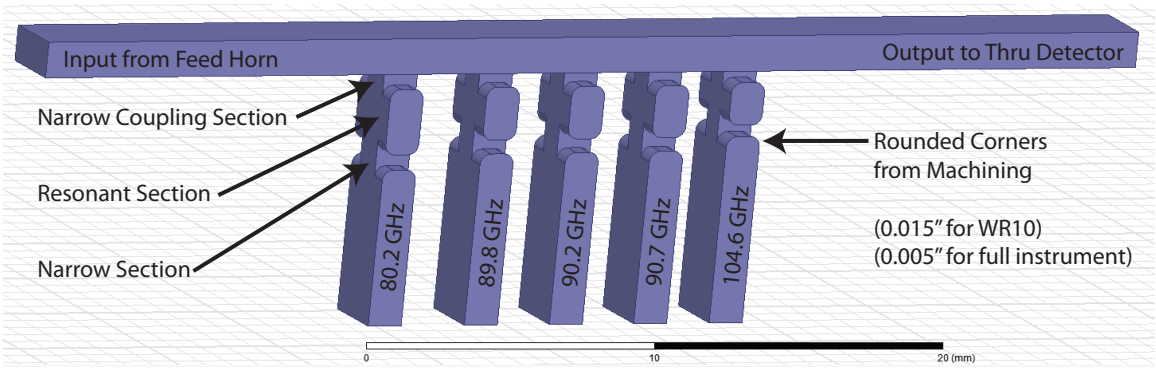

Figure 28: HFSS model for 5-channel W-Band prototype illustrating design concept for WSpec. A feed horn (not shown) receives broadband light, which propagates down a main waveguide, and different frequencies are selected off by each of five spectral channels. We account for rounded corners, a product of machining, in our simulations.

of Fig. 29, respectively. The three main design parameters are resonator length, which tunes the channel's center frequency, and coupling length and width, which both control the channel's quality factor. Since the cutoff frequency of the coupling sections is approximately 1.5 times the channel's center frequency, these sections are seen as capacitive loads. On-resonance, the cavity becomes an inductive load that tunes out the capacitive sections allowing a narrow band of light centered on the resonant frequency to propagate through to that channel's KID. Off-resonance, no impedance cancellation occurs, so no light passes through. Therefore, each channel is a narrow-band frequency filter.

4.4.2 5-Channel W-Band Prototype

We have successfully designed, fabricated, and tested a 5-channel prototype filter bank for W-Band ($75-110$ GHz) implemented in WR-10 rectangular waveguide. The reason for choosing this band is two-fold. We own a W-Band VNA extension module

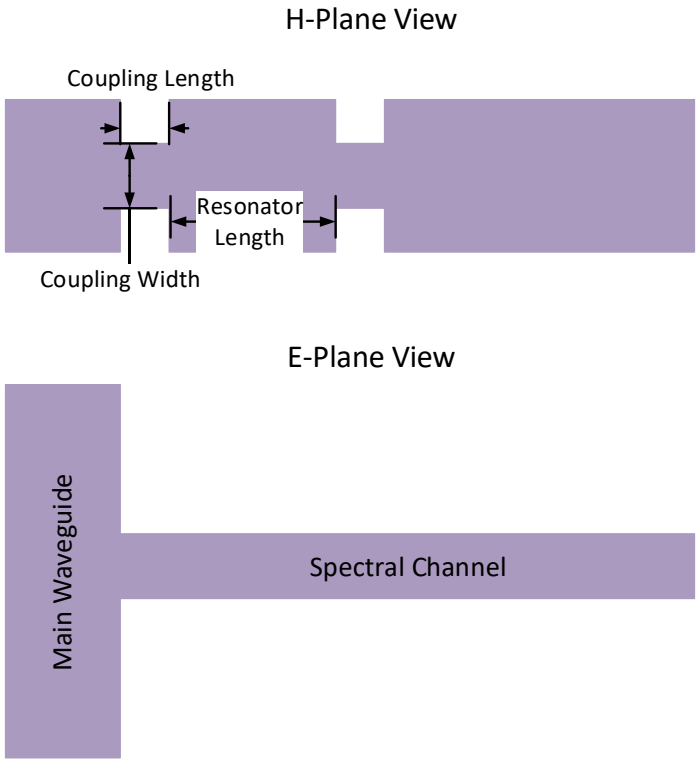

Figure 29: Closeup H-plane (top) and E-plane (bottom) views of single WSpec spectral channel. Three design parameters labeled in H-plane view.

from OML and the relatively large 1.27×2.54 mm dimensions of WR-10 waveguide are suitable for a first fabrication to evaluate machining accuracy. We design the prototype to have five $\mathcal{R} = 200$ channels with center frequencies given in the first column of Table 5. For a Nyquist sampled ($\Sigma = 2$) filter bank targeting $\mathcal{R} = 200$ with $f_u = 110$ GHz and $f_l = 75$ GHz, the number of channels is $N_{\text{ch}} = 77$ according to Eq. 4.2. We calculate f_r for all 77 channels using Eq. 4.3 and choose our five channels the following way. The lowest and highest frequency channels are chosen to span W-Band while the middle three are chosen to demonstrate log-spacing. We use $3\lambda_g/4$ physical spacing between adjacent channels, where λ_g is the average guided wavelength of the two channels, because this is the smallest physically realizable

odd integer multiple of $\lambda_g/4$. Individual channels were optimized by using HFSS with its MATLAB API to obtain the appropriate dimensions for each channel before fabrication. Just as planned for the demonstrator instrument, we employ E-plane split-block construction using conventional alignment pins, as shown in the top left panel of Fig. 30. The prototype device was machined from aluminum using a 5 μm tolerance micromilling machine at ASU. The 1 μm tolerance required for the higher-frequency full size instrument is achieved consistently on another machine in the ASU Micromachining Laboratory.

After optimizing the dimensions for each channel, we performed a final simulation of the entire 5-channel prototype device in HFSS using these dimensions. The full structure was small enough to simulate in a single day and the results are shown in the top panel of Fig. 31. We fit Lorentzian curves to both the simulated and measured response of each channel to extract the parameter values listed in Table 5. we see that the simulation closely matches design values for center frequency, but deviates more from the designed $\mathcal{R} = 200$ resolving power suggesting that channel crosstalk has a disproportional effect on R. Results from measurements of our prototype using the setup in Fig 30 are plotted in the bottom panel of Fig. 31. Measured center frequencies agree with the simulation to within 0.5% and resolving powers to within 30%. The standing wave pattern observed in the through detector spectrum is most likely due to imperfect terminations in the horns or detectors and/or a mismatch inside the VNA extension module. We also list the simulated and measured peak optical efficiency (OE) of each channel in Table 5. It is evident that crosstalk significantly alters OE from its nominal value of 50%. Overall, our measurement results agree with the HFSS simulation, confirming that our device nominally works according to design

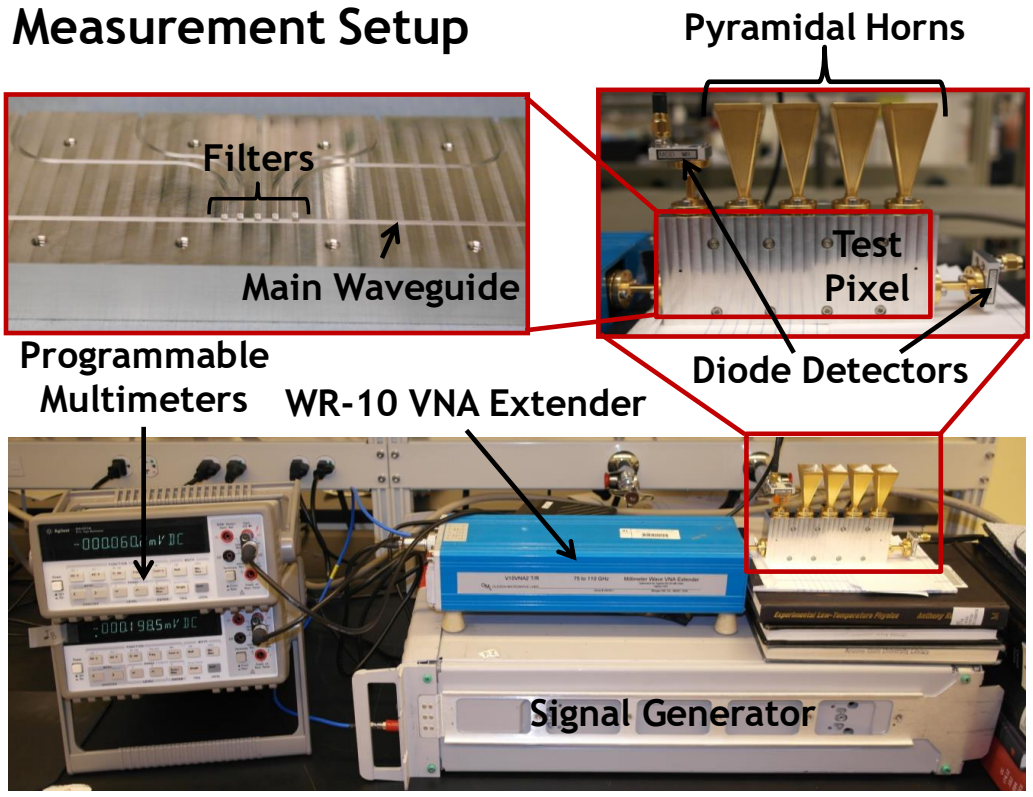

Figure 30: Laboratory setup for measuring our W-Band prototype (bottom), featuring closeup views of the device connected to horns and detectors (top-right) and half of the device, illustrating E-plane split-block construction (top-left).

and suggesting HFSS as an appropriate tool to design our 4-pixel demonstration instrument.

4.4.3 4-Pixel Demonstration Spectrometer

An important next step is to demonstrate a small array of waveguide spectrometer pixels coupled to arrays of KIDs targeting a scientifically interesting frequency band. We have decided to construct a 4-pixel array of filter banks targeting the $130-250$ GHz

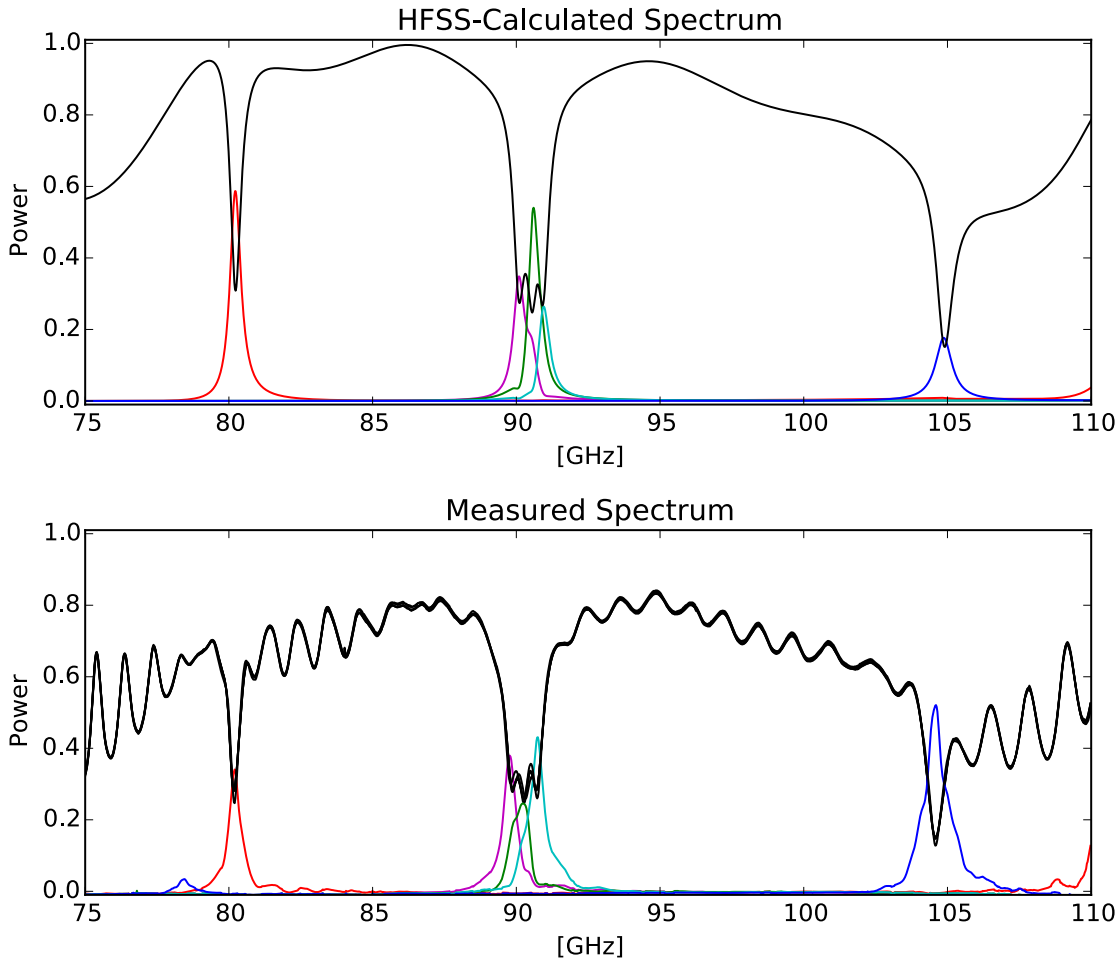

Figure 31: Simulated (top) and measured (bottom) power absorbed by each channel (color) and thru detector (black) of our 5-channel W-Band prototype device.

band, which is optimal for studying CO line emission and the kinetic SZ effect. In order to Nyquist sample the entire $130 - 250$ GHz band, we need 108 channels. The entire band is too wide for a single mode rectangular waveguide, so we will split the band into a lower band (band A) below the 183 GHz atmospheric absorption line and upper band (band B) above the line. Two independent horns will feed 54-channel filter banks covering bands A and B and these two filter banks collectively comprise a single spatial pixel. As illustrated in Fig. 32, which is a CAD drawing of our 4-pixel

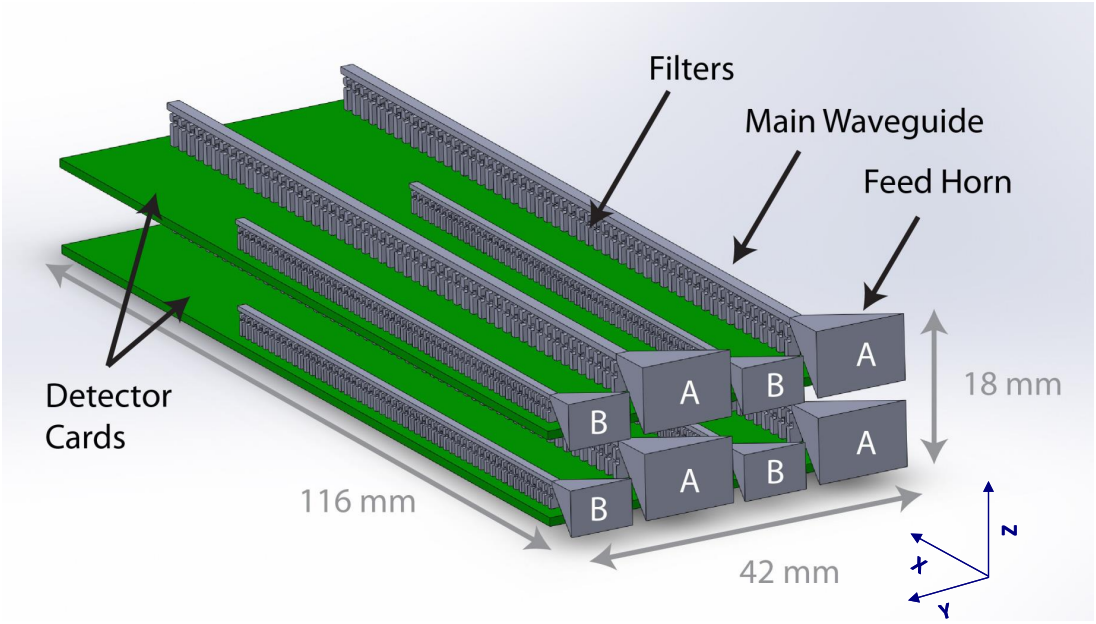

Figure 32: SolidWorks drawing of our horn-coupled 4-pixel focal plane array of filter banks.

design, a linear array of spatial pixels is formed in the Y-direction, with all spectral channels in the X-direction and feeding a single card of KIDs. These linear arrays are then stacked in the Z-direction to form a filled 2-dimensional focal plane array of filter bank spectrometer pixels. Using $3\lambda_g/4$ physical spacing between adjacent channels, the band A and band B filter banks, are only 96 mm and 68 mm long, respectively, excluding horns. As eventual goal for this technology is a 100-pixel instrument, which would still be relatively compact.

Drawing and simulating an entire 54-channel filter bank is prohibitively memory-intensive and time-consuming to do in a single HFSS run. Therefore, we developed an equivalent method, which entails using HFSS to compute the scattering matrix of each individual channel and then cascading these matrices together with the scikit-rf package in python. Using this method, we can reproduce all the details of a full HFSS

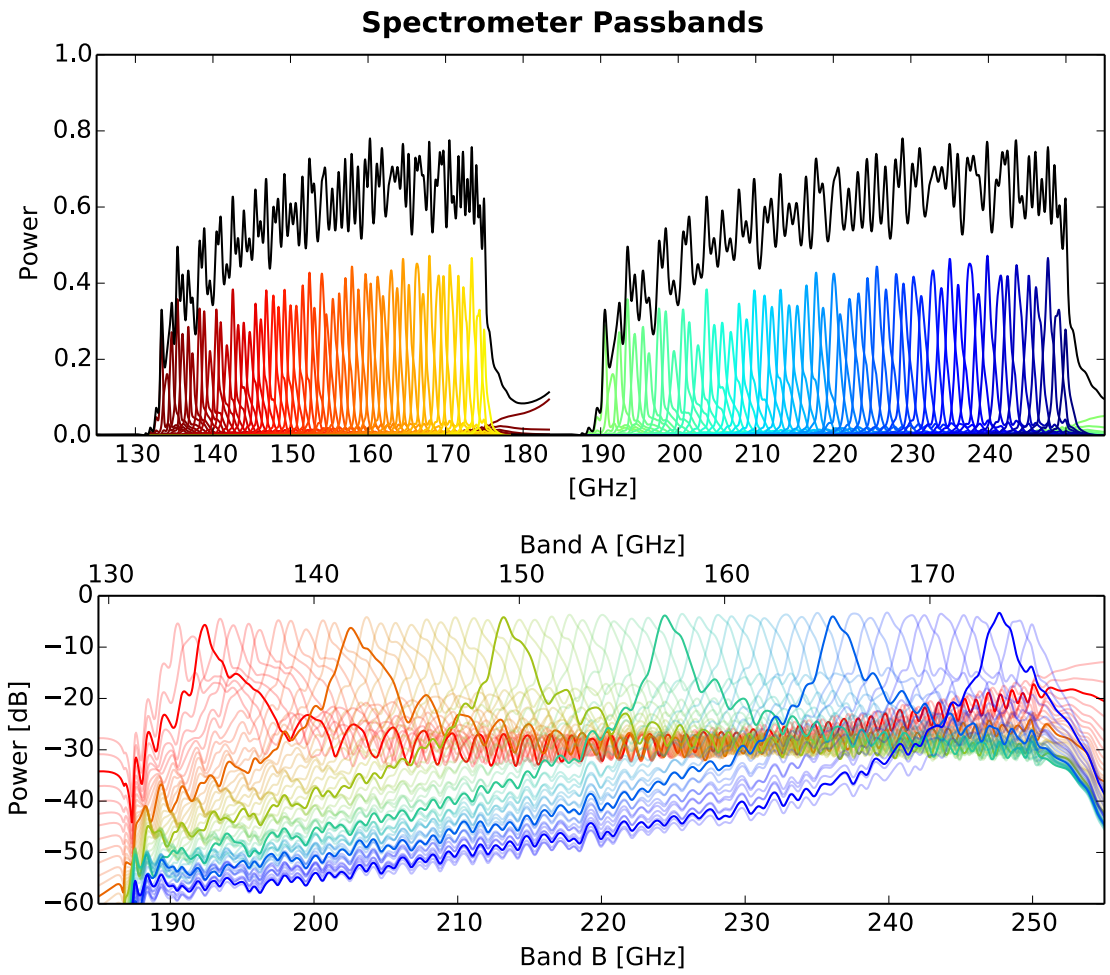

Figure 33: HFSS-simulated response in linear units (top) and dB (bottom) for band A, which covers $135 - 170$ GHz, and band B, which covers $190 - 245$ GHz. The black curve in the top panel represents the sum total of all channels.

simulation down to the -60 dB level and simulate an entire 54-channel filter bank in only 3 hours of computer time. We simulated both band A and band B filter banks and the results are shown in both linear units and dB in Fig. 33 . The peak optical efficiency of the channels ranges from 25% to 40% and the out-of-band coupling is at the -20 to -30 dB level.

4.4.4 Loss and Machining Tolerance

Good agreement between lossless conductor HFSS simulations and measurements of our prototype implies that conductor loss is not limiting the performance of our W-Band device at room temperature. For the dominant TE_{10} mode of rectangular waveguide, the attenuation constant due to conductor loss is

$$(\alpha_c)_{10} = \sqrt{\frac{\pi f \mu_0}{\sigma}} \frac{\left[1 + \frac{2b}{a}\left(\frac{f_c}{f}\right)^2\right]}{\eta_0 b \sqrt{1 - \left(\frac{f_c}{f}\right)^2}} \ (\mathrm{Np/m}), \tag{4.17}$$

where σ is the metal conductivity, $\eta_0 = 377\ \Omega$ is the impedance of free space, a and b are the waveguide dimensions, and

$$f_c = \frac{1}{2a\sqrt{\mu_0 \epsilon_0}} \tag{4.18}$$

is the cutoff frequency of this dominant mode (Balanis 2012). This loss can be expressed as the quality factor

$$Q_{\mathrm{loss}} = \frac{2\pi}{1 - e^{-(\alpha_c)_{10}\lambda_g}}, \tag{4.19}$$

which degrades the actual resolving power achieved by the spectrometer. Analogous to Eq. 4.1, the effective resolving power in the presence of loss is

$$\frac{1}{\mathcal{R}_{\mathrm{eff}}} = \frac{1}{\mathcal{R}} + \frac{1}{Q_{\mathrm{loss}}}. \tag{4.20}$$

At room temperature, the conductivity of aluminum is 3.816×10^7 S/m, so Eq. 4.17 gives an attenuation constant of 0.25 Np/m at 105 GHz. This corresponds to a $Q_{\mathrm{loss}} \sim 7000$, which has a negligible impact on a spectrometer designed for $\mathcal{R} = 200$. However, scaling the design to higher frequencies could make conductor loss a more

significant factor. At the highest frequency in our target band 250 GHz, $Q_{\rm loss} \sim 4500$, which is still high enough to only slightly degrade the performance of a spectrometer designed for $\mathcal{R} = 200$. Operating the device at cryogenic temperatures and switching from aluminum to a different material such as gold-plated OFHC copper would reduce loss. Sputter coating the waveguide with Nb and operating below its superconducting critical temperature would eliminate conductor loss entirely below its gap frequency of ~ 670 GHz. (Bryan et al. 2015) includes a brief discussion on how machine tolerance may limit performance at higher frequencies.

4.5 Summary

We have developed a lumped element microwave network model with accuracy comparable to full-wave EM simulation to serve as a general purpose tool for evaluating SuperSpec devices. While likely to be complicated random fabrication variance, we will apply our model to a large number of previous measurements to look for systematic relationships between design and measured values of f_r, $Q_{\rm feed}$, and $Q_{\rm det}$. In addition, our model can be used to optimize filter bank sensitivity by computing noise equivalent power as a function of design parameters. Our lumped element approach captures neither distributed coupling perfectly nor direct coupling between between KIDs and the feedline at all, so we will further explore its limitations. Nevertheless, our model will play an instrumental role in converging on a filter bank design covering the entire $190 - 310$ GHz band for on-sky demonstration.

We also presented an implementation of the same filter bank concept in rectangular waveguide instead of planar transmission lines. We optimized and fabricated a 5-channel prototype operating in W-Band. Measurements of this device have yielded

promising results, demonstrating the basic design concept and paving the way to develop a 4-pixel demonstration instrument employing this technology that operates in the $130 - 250$ GHz band. For this instrument, each pixel is comprised of 54 spectral channels to Nyquist sample the band. We scaled our 5-channel W-Band prototype to work at ~ 200 GHz and measurement results on this higher frequency prototype are included in (Bryan et al. 2016). In the future, we may investigate the possibility of incorporating an orthomode transducer and wide band frequency diplexer to allow dual polarization measurements over the entire frequency band for each pixel.

Table 4: Design, initial guess, and model fit parameter values for 6-channel log-spaced filter bank.

Parameter	Q_{feed}	Q_{det}	Q_{loss}	$f_{r,1}$ (GHz)	$f_{r,2}$ (GHz)	$f_{r,3}$ (GHz)	$f_{r,4}$ (GHz)	$f_{r,5}$ (GHz)	$f_{r,6}$ (GHz)
Design	295	295	∞	212.3	211.9	211.5	211.0	210.4	210.0
Guess	295	295	10^{10}	212.3	210.9	210.3	209.7	209.1	208.7
Fit	321	242	10^{10}	212.3	210.9	210.5	209.8	209.3	209.0

Table 5: Design, simulated, and measured parameter values for 5-channel WSpec prototype. Simulated and measured peak optical efficiencies (OEs) are also included.

Channel	Design f_r (GHz)	Sim. f_r (GHz)	Meas. f_r (GHz)	Sim. $\mathcal{R}$	Meas. $\mathcal{R}$	Sim. OE	Meas. OE
1	80.35	80.22	80.20	182	178	59%	34%
2	90.28	90.09	89.78	120	180	35%	38%
3	90.73	90.60	90.23	193	120	54%	24%
4	91.20	90.95	90.75	207	158	26%	43%
5	105.10	104.87	104.60	154	135	18%	52%

Chapter 5

W-BAND PHASE SHIFTER AND PARAMETRIC AMPLIFIER

The W-Band ($75 - 110$ GHz) sky contains a plethora of information about star formation, galaxy evolution and the cosmic microwave background. We have designed and fabricated a dual-purpose superconducting circuit to facilitate the next generation of astronomical observations in this regime by providing proof-of-concept for both a millimeter-wave low-loss phase shifter, which can operate as an on-chip Fourier transform spectrometer (FTS) and a traveling wave kinetic inductance parametric amplifier (TKIP). Superconducting transmission lines have a propagation speed that depends on the inductance in the line which is a combination of geometric inductance and kinetic inductance in the superconductor. The kinetic inductance has a non-linear component with a characteristic current, I_*, and can be modulated by applying a DC current, changing the propagation speed and effective path length. Our test circuit is designed to measure the path length difference or phase shift, $\Delta\phi$, between two symmetric transmission lines when one line is biased with a DC current. To provide a measurement of $\Delta\phi$, a key parameter for optimizing a high gain W-Band TKIP, and modulate signal path length in FTS operation, our 3.6×2.5 cm chip employs a pair of 503 mm long NbTiN inverted microstrip lines coupled to circular waveguide ports through radial probes. For a line of width 3 μm and film thickness 20 nm, we predict $\Delta\phi \approx 1767$ rad at 90 GHz when biased at close to I_*. We have fabricated a prototype with 200 nm thick Nb film and the same line length and width. The predicted phase shift for our prototype is $\Delta\phi \approx 30$ rad at 90 GHz when biased at close to I_* for Nb.

Many astronomical observations at long wavelengths use coherent amplification

of weak signals from the sky to enable readout. The figures of merit for an amplifier are gain, bandwidth, dynamic range, and noise performance. An ideal amplifier produces high, uniform gain over the entire observation band while exhibiting both high dynamic range and quantum-limited noise performance. Wideband amplifiers are used as the first stage in radio astronomy receivers (Weinreb et al. 2009; Pospieszalski 2012; Goddard and Milne 1994) and as intermediate frequency (IF) amplifiers for mm-wave-THz heterodyne receivers. The use of low noise first stage amplifiers could increase the instantaneous bandwidth and simplify the design of higher frequency instruments. High electron mobility transistor (HEMT) amplifiers achieve > 20 dB gain over the entire ALMA Band 3 ($84 - 116$ GHz), but their best noise temperature is ~ 25 K, which is 5-10 times above the quantum limit (Cuadrado-Calle et al. 2017; Tang et al. 2017; Samoska et al. 2012) and is a significant contribution to the system noise. Replacing HEMTs with an amplifier that simultaneously achieves high gain across multi-octave instantaneous bandwidth and quantum-limited noise performance would significantly improve the sensitivity of ALMA and similar instruments.

The TKIP is an emerging technology that offers both wide instantaneous bandwidth and quantum-limited noise performance. Parametric amplifiers produce gain through four wave or three wave mixing (FWM/TWM) during which a strong pump mixes with a weak signal through a non-linear medium. Fiber optic amplifiers, which exploit the Kerr effect of non-linear optical materials, represent a well-established amplifier technology in the telecommunications industry (Hansryd et al. 2002; Tong et al. 2011). TKIPs, which exploit the non-linear kinetic inductance of superconductors, provide an analogous amplifier technology for mm-wave applications. Realized in superconducting transmission lines (STLs), which are inherently wideband, TKIPs achieve a maximum gain that depends on two superconductor material properties: I_*, the characteristic

current parameter that sets the scale for non-linearity and $\Delta\phi_{\max}$, the maximum non-linear phase shift that can be induced by applying DC bias to a STL (Ho Eom, Day, LeDuc, et al. 2012). (Bockstiegel et al. 2014; Adamyan et al. 2016; Vissers et al. 2016; Chaudhuri et al. 2017) have investigated TKIPs operating in the 10 GHz range that achieve ~ 15 dB gain over ~ 4 GHz of bandwidth and noise temperature as low as 0.5 ± 0.3 K, which approaches the quantum limit.

We have developed a dual purpose superconducting circuit with an inverted microstrip geometry that provides proof-of-concept for two technologies: a W-Band TKIP and a DC current controlled differential phase shifter which can act as an on-chip FTS. As a phase shifter, our circuit also provides a measurement of $\Delta\phi_{\max}$, which combined with I_* from previous experiments, provides the parameters necessary to design and optimize a high-gain W-Band TKIP. The STLs on our device are not dispersion-engineered, but will still produce quadratic gain, demonstrating parametric amplification due to FWM/TWM at W-Band frequencies. Here we describe our circuit design, fabrication process, test setup, and phase shift and gain measurements.

5.1 Principle and Design

5.1.1 Kinetic Inductance Parametric Amplification

For $T \ll T_c$, the kinetic inductance per unit length of a STL is

$$\mathcal{L}_k(I) \simeq \mathcal{L}_{k,0}\left[1 + \left(\frac{I}{I_*}\right)^2\right], \tag{5.1}$$

where $\mathcal{L}_{k,0}$ is the intrinsic kinetic inductance per unit length, I_* is the characteristic current, and I is the bias current applied to the line. The quadratic term in Eq. (5.1) represents the non-linearity through which FWM/TWM occurs to generate gain in

a STL. Three tones are involved in this process: a strong pump (f_p), a weak signal (f_s), and generated idler (f_i). The strong pump mixes with a weak signal along the STL converting two pump photons into a signal photon and an idler photon with frequency $f_i = 2f_p - f_s$, thus amplifying the weak signal by drawing power from the pump. Stronger pump tones result in more gain, but we are limited by I_*, which corresponds to the maximum pump power before the onset of dissipation. Following (Ho Eom, Day, Leduc, et al. 2012), we measured $I_* \approx 0.4$ mA at a readout power of -68 dBm for the low Q NbTiN resonators shown in Fig. 34 with 10 μm line width and 20 nm film thickness by monitoring its fractional detuning at increasing readout powers. I_* sets a limit on the non-linearity and thus a limit on the gain that can be produced by a STL of a given material and geometry. NbTiN is a particularly suitable superconductor for TKIP technology due to its large non-linearity and low microwave loss.

In the absence of an applied current, a tone propagates down a STL with speed

$$v_{p,0} = \frac{1}{\sqrt{(\mathcal{L}_{k,0} + \mathcal{L}_m)\mathcal{C}}}, \tag{5.2}$$

where $\mathcal{L}_m$ and $\mathcal{C}$ are the line's geometric inductance and capacitance per unit length, respectively, and attains a phase shift equal to the line's unbiased path length

$$\phi_0 = \frac{2\pi f l}{v_{p,0}}, \tag{5.3}$$

where l is its physical length. Applying a DC bias $I \leq I_*$ to the line, the propagation speed and biased path length become

$$v_p(I) = \frac{1}{\sqrt{(\mathcal{L}_k(I) + \mathcal{L}_m)\mathcal{C}}} \tag{5.4}$$

and

$$\phi(I) = \frac{2\pi f l}{v_p(I)}, \tag{5.5}$$

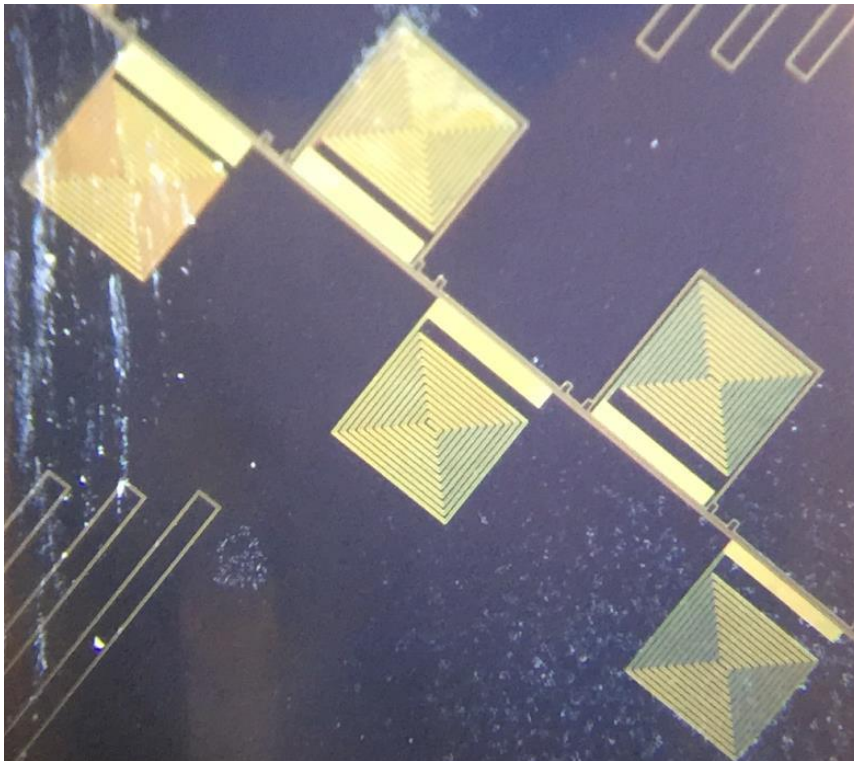

Figure 34: NbTiN resonators with resonant frequencies ~ 2 GHz fabricated at ASU to probe non-linearity.

respectively, resulting in an additional non-linear phase shift

$$\Delta\phi\left(I\right) = \phi\left(I\right) - \phi_0 \tag{5.6}$$

compared to that attained on the unbiased line. This non-linear phase shift causes dispersion between the pump, signal, and idler tones, resulting in a predicted signal gain of

$$G_s = 1 + \left(\Delta\phi\right)^2, \tag{5.7}$$

which defines the quadratic gain regime of FWM/TWM.Phase matching these tones through dispersion engineering (Chaudhuri, Gao, and Irwin 2015) enables us to access the the exponential gain behavior of FWM/TWM, namely

$$G_s = \frac{e^{2\Delta\phi}}{4}. \tag{5.8}$$

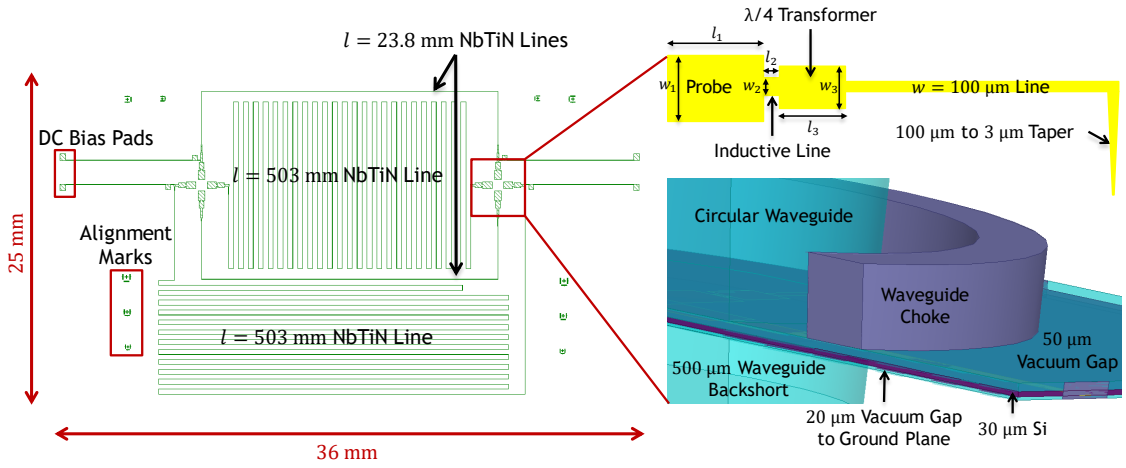

Figure 35: W-Band phase shifter and TKIP circuit layout (left) with detailed top (top right) and cross-sectional (bottom right) views of the radial probe circular waveguide-to-inverted microstrip transition. Optimizing the dimensions for maximum coupling between the waveguide and inverted microstrip across the band yields the following: $w_1 = 0.4$ mm, $l_1 = 0.56$ mm, $w_2 = 0.1$ mm, $l_2 = 0.07$ mm, $w_3 = 0.3$ mm, and $l_3 = 0.4$ mm.

In both cases, we need to measure $\Delta\phi$ to determine the maximum achievable gain, which defines the requirement on a TKIP's STL length.

5.1.2 Circuit Design

To measure $\Delta\phi$, we developed the circuit shown in Fig. 35. The device is comprised of two pairs of 3 μm wide inverted microstrip lines with 20 nm NbTiN film thickness. A pair of identical 503 mm long lines are used to measure $\Delta\phi$ and a pair of 23.8 mm long lines, which support a linear polarization orthogonal to that of the first pair, are used to calibrate the measurement setup. To measure $\Delta\phi$, one of the 503 μm lines is biased at $I \leq I_*$ with the other line unbiased. Radial probes couple a single frequency tone from an input waveguide port to both 503 mm lines. When they recombine at

the output port, the signal on the biased line has been shifted an additional $\Delta\phi$ in phase relative to the signal on the unbiased line resulting in constructive or destructive interference. To determine $\Delta\phi$, we measure the complex transmission coefficient, S_{21}, at the output port as a function of bias current. Our choice of circular waveguide input and output allows us to access both microstrip polarizations without disassembling the setup.

Fig. 35 also provides top and cross sectional closeup views of our radial probe circular waveguide-to-inverted microstrip transition (vice versa for the output port), which is based on designs from (Shih, Ton, and Bui 1988; Fan, Li, and Chang 1995; Leong and Weinreb 1999; Datta et al. 2014). Our design consists of a rectangular probe that intercepts the TE_{11} waveguide mode followed by a broadband impedance matching section. In the impedance matching section, an inductive line tunes out the probe's capacitance, a quarterwave transformer matches 2.46 mm diameter circular waveguide to 100 μm wide inverted microstrip across W-Band, and a taper transitions the line width from 100 μm to 3 μm. We used HFSS and its MATLAB API to optimize all dimensions to achieve maximum coupling between the waveguide and inverted microstrip across the band. Beginning at the waveguide, the dielectric stack for our back-illuminated design consists of a 50 μm vacuum layer, 30 μm Si substrate, and 20 μm vacuum layer between the lines and ground plane, forming our inverted microstrip geometry. The waveguide itself is surrounded by a choke that attenuates higher order modes and terminated in a standard quarterwave backshort. A detailed description of this design is given in (Surdi 2016).

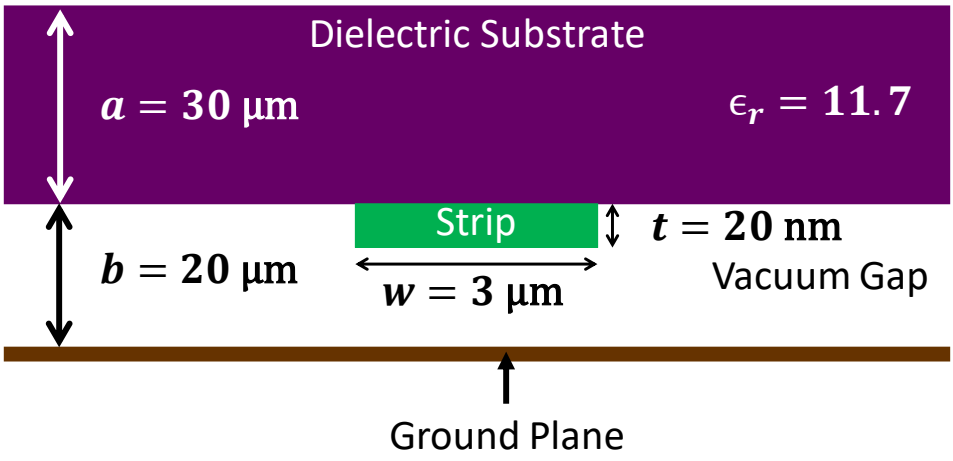

Figure 36: Inverted microstrip geometry for W-Band phase shifter and TKIP circuit.

5.1.3 Predicted Performance

Our inverted microstrip geometry is shown in Fig. 36. We use empirical formulas to determine this geometry's characteristic impedance Z_0 and effective dielectric constant ϵ_{eff} in order to calculate $\mathcal{L}_m$ and $\mathcal{C}$. Following (Garg et al. 2001), for inverted microstrip when $t/(a+b) \ll 1$,

$$Z_0 = \frac{60}{\epsilon_{\text{eff}}} \ln \left[\frac{f(u)}{u} + \sqrt{1 + \left(\frac{2}{u}\right)^2} \right], \tag{5.9}$$

where

$$f(u) = 6 + (2\pi - 6) \exp\left[-\left(\frac{30.666}{u}\right)^{0.7528} \right], \tag{5.10}$$

$u = w/b$, and ϵ_{eff} is the effective dielectric constant, which is given by

$$\sqrt{\epsilon_{\text{eff}}} = 1 + \frac{a}{b}\left(\bar{a} - \bar{b} \ln \frac{w}{b}\right)\left(\sqrt{\epsilon_r} - 1\right), \tag{5.11}$$

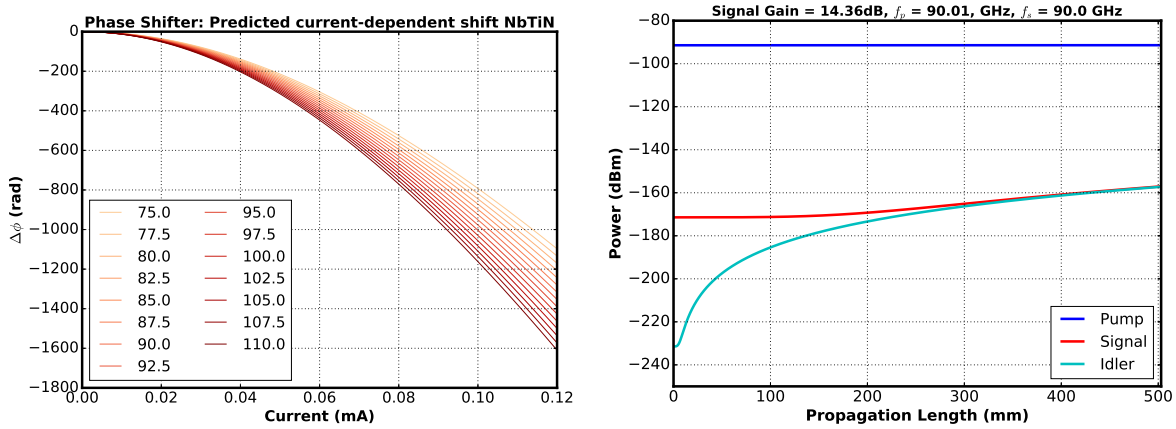

(a) (b)

Figure 37: Predicted non-linear phase shift $\Delta\phi$ for our NbTiN circuit at various W-Band frequencies as a function bias current (a). Predicted signal gain due to FWM/TWM as a function of propagation length for $f_p \approx f_s = 90$ GHz (b). For a -91 dBm pump, which is initially 80 dB above the signal, our line geometry produces 14.36 dB of signal gain.

where

$$\begin{aligned} \bar{a} &= \left(0.5173 - 0.1515 \ln \frac{a}{b}\right)^2 \\ \bar{b} &= \left(0.3092 - 0.1047 \ln \frac{a}{b}\right)^2 \end{aligned} \tag{5.12}$$

and ϵ_r is the dielectric constant of the substrate. For $a = 30$ μm, $b = 20$ μm, $w = 3$ μm, and $\epsilon_r = 11.7$ for Si, Eqs. 5.9-5.12 yield $Z_0 = 106$ Ω and $\epsilon_{\text{eff}} = 5.04$, so the normal state propagation speed is $v_{p,n} = 1.34 \times 10^8$ m/s. Since

$$Z_0 = \sqrt{\frac{\mathcal{L}_m}{\mathcal{C}}} \tag{5.13a}$$

$$v_{p,n} = \frac{1}{\sqrt{\mathcal{L}_m \mathcal{C}}}, \tag{5.13b}$$

we obtain $\mathcal{L}_m = 0.80$ μH/m and $\mathcal{C} = 70.38$ pF/m.

The normal state resistivity of NbTiN film has been measured to be $\rho_n \approx 140$ $\mu\Omega$ cm

Westig et al. 2013. For $T \ll T_c$, the penetration depth is

$$\lambda_0 = \sqrt{\frac{\hbar \rho_n}{\pi \mu_0 \Delta_0}}, \tag{5.14}$$

where μ_0 is the permeability of free space and Δ_0 is the superconductor energy gap. Since $\Delta_0 = 1.76 k_B T_c$, where k_B is Boltzmann's constant and T_c is the superconductor critical temperature, and $T_c = 14.5$ K for NbTiN (Westig et al. 2013), $\lambda_0 \approx 325$ nm, so the intrinsic kinetic inductance per unit length for our STL is

$$\mathcal{L}_{k,0} = \frac{\mu_0 \lambda_0^2}{wt} \approx 2.22 \ \mu\text{H/m}, \tag{5.15}$$

where w and t are its line width and film thickness, respectively. Assuming uniform current density, scaling its value from Section 5.1.1 to these dimensions yields $I_* = 0.12$ mA. Applying a DC bias at this level to our 503 mm long line results in $\Delta\phi \approx 1318$ rad at 90 GHz according to Eqs. 5.2-5.6. Fig. 37a shows the predicted non-linear phase shift as a function of bias current across W-Band. As shown in Fig. 37b, FWM/TWM over 503 mm of NbTiN inverted microstrip produces 14.36 dB of signal gain for $f_p \approx f_s = 90$ GHz and a pump that is initially eight orders of magnitude stronger than the signal.

To facilitate rapid proof-of-concept testing, we have fabricated a prototype on 200 nm thick Nb film while keeping the same geometry. $\rho_n \approx 59 \ \mu\Omega\,\text{cm}$ and $T_c = 9.2$ K for Nb (Westig et al. 2013), so the penetration depth is $\lambda_0 \approx 84$ nm, which agrees with (Anlage, Snortland, and Beasley 1989). We are no longer in the thin film regime, so we use the full expression in (Doyle 2008), namely

$$\mathcal{L}_{k,0} = \frac{\mu_0 \lambda_0}{4w} \left[\coth\left(\frac{t}{2\lambda_0}\right) + \left(\frac{t}{2\lambda_0}\right) \csc^2\left(\frac{t}{2\lambda_0}\right) \right], \tag{5.16}$$

to calculate the intrinsic kinetic inductance for Nb to be $\mathcal{L}_{k,0} = 22.7$ nH/m, which is much smaller than that for NbTiN. The characteristic current density for a supercon-

ductor is

$$J_* = \sqrt{\frac{4\pi N_0 \Delta_0^3}{\hbar \rho_n}}, \tag{5.17}$$

where N_0 is the single-spin density of states per unit energy per unit volume. Therefore,

$$\frac{J_{*,\mathrm{Nb}}}{J_{*,\mathrm{NbTiN}}} = \left(\frac{\rho_{n,\mathrm{NbTiN}}}{\rho_{n,\mathrm{Nb}}}\right)^{\frac{1}{2}} \left(\frac{\Delta_{0,\mathrm{Nb}}}{\Delta_{0,\mathrm{NbTiN}}}\right)^{\frac{3}{2}} \left(\frac{N_{0,\mathrm{Nb}}}{N_{0,\mathrm{NbTiN}}}\right)^{\frac{1}{2}} \approx 3.48, \tag{5.18}$$

where we have estimated $(N_{0,\mathrm{Nb}}/N_{0,\mathrm{NbTiN}})^{1/2} \sim 20$. Accounting for the order of magnitude increase in film thickness, biasing the Nb line with the same geometry otherwise at $I_* = 4.2$ mA results in a predicted phase shift of $\Delta\phi \approx 30$ rad at 90 GHz, which is still measurable using our network analyzer (VNA) setup.

5.2 Device Fabrication

Beginning with a silicon-on-insulator (SOI) wafer comprised of a 30 μm high-resistivity device Si layer, 2 μm buried oxide layer, and 500 μm handle Si layer, we use DC sputtering to deposit 20 nm of NbTiN on the device Si layer. After depositing the metal, the main steps of our fabrication process are illustrated in Fig. 38 and described below.

1. Using contact lithography, expose the circuit layout defined by the device mask onto a ~ 1.3 μm layer of AZ 3312 photoresist directly above the NbTiN film. This mask defines two identical circuits in the area of a 4 inch wafer, so each wafer yields two chips.
2. After developing the device side pattern in the photoresist, use reactive ion etching (RIE) with fluorine chemistry to define the circuit pattern in the NbTiN.

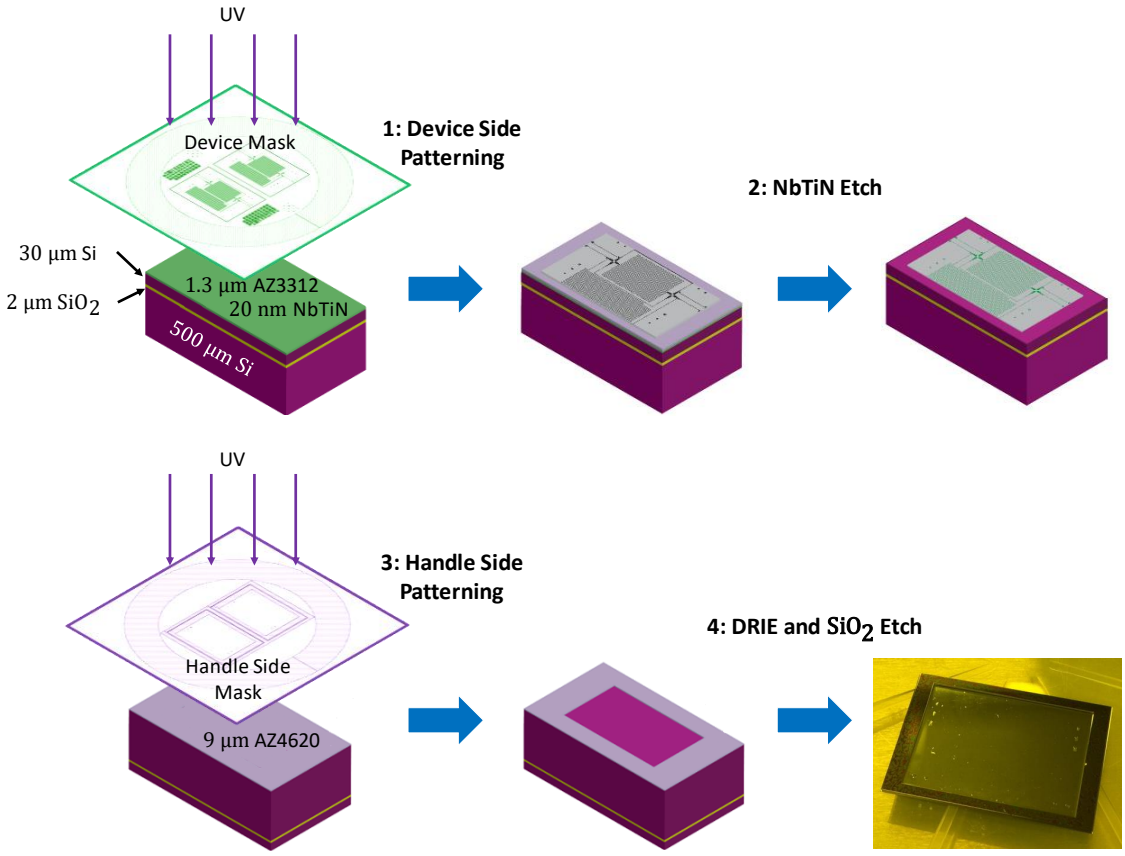

Figure 38: Fabrication process for W-Band phase shifter and TKIP circuit.

3. Flip the wafer around and use contact lithography to expose the scribe grid and large central rectangles defined by the handle side mask onto a ~ 9 μm layer of AZ 4620 photoresist directly above the handle Si.
4. After developing the handle side pattern in the photoresist, use deep reactive ion etching (DRIE), in particular the Bosch process, to define the scribe grid and rectangular depressions in the handle Si. This step, followed by a SiO_2 etch, completely punches through the 500 μm handle Si and 2 μm buried oxide to simultaneously place the circuit on a 30 μm Si membrane and separate the chips from the wafer. The bottom-right image in Fig. 38 is a handle side view of a completed chip.

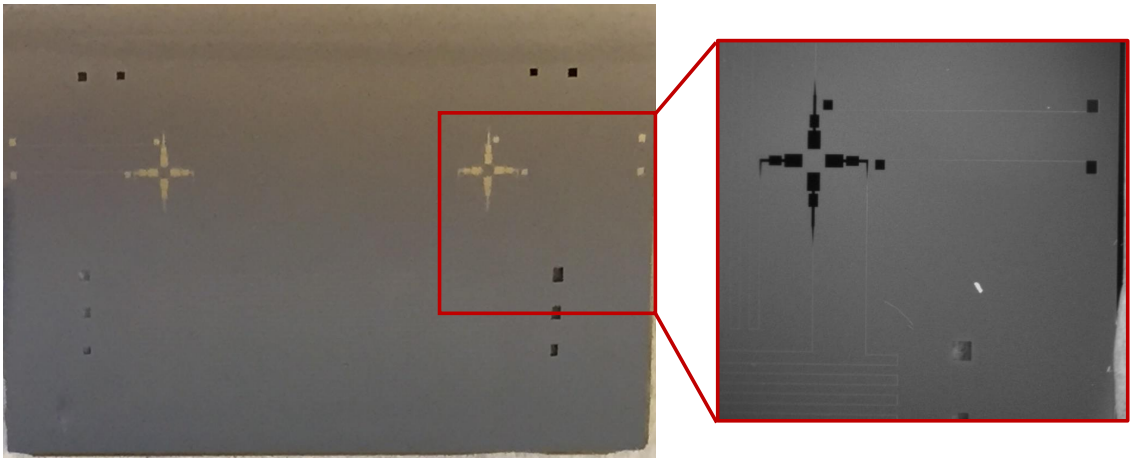

Figure 39: Prototype of W-Band phase shifter and TKIP circuit with 200 nm Nb film.

We have fabricated a prototype of our circuit using 200 nm thick Nb film in the ASU NanoFab. The process is identical to that above with the exception of depositing 200 nm of Nb instead of 20 nm of NbTiN before the first lithography step. The device side of a completed Nb prototype chip with a closeup on an inverted microstrip-to-circular waveguide transition is shown in Fig. 39. The exact details of the fabrication process we run in the ASU NanoFab is given in Appendix **??** (reference the exact section of the appendix when written).

5.3 Device Packaging

To establish our inverted microstrip dielectric stack, provide waveguide ports, and implement DC bias capability, we have designed the three-piece copper chip package shown in Fig. 40a. We choose copper to facilitate soldering to sections of copper waveguide in our waveguide feedthrough described in Section 5.4 and minimize thermal contraction when cooled to cryogenic termperatures. The chip is mounted to the piece labeled Backplate, into which the waveguide ports, chokes, and holes for DC bias pins

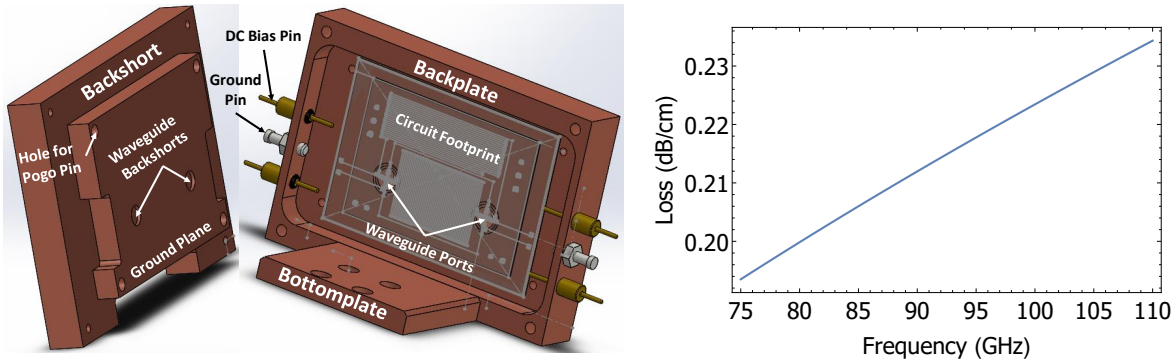

(a) (b)

Figure 40: Three-piece copper chip package for our phase shifter and TKIP circuit (a). Plot of copper ground place loss as a function of frequency in W-Band (b).

are directly machined. The waveguide backshorts are machined into the piece labeled Backshort, which also contains the ground plane. When Backplate and Backshort are fastened together, the former maintains a 50 μm gap between the waveguide port and bare Si while the latter maintains a 20 μm gap between the circuit and ground plane. Due to the precise dimensions required, this package was manufactured in the ASU Micromachining Laboratory, which regularly achieves feature size tolerance of ± 1 μm. The third piece, Bottomplate, mounts to the 4 K stage of our cryostat.

While the NbTiN or Nb strips will be superconducting, the copper ground plane will be lossy. Conductor loss on a transmission line is given by

$$\alpha_c = 8.686 \times \frac{R'}{2Z_0} (\text{dB/m}), \tag{5.19}$$

where R' is the high frequency resistance per unit length of the conductor. For loss due to the ground plane, we estimate that the fields spread out uniformly by a factor of 5 above the strip, so $R' \approx 0.2 R_s/w$, where $R_s = \sqrt{\omega \mu_0 \rho / 2}$ is the surface resistance of the conductor. For copper with a residual resistivity ratio (RRR) of 10, $\rho = 1.7$ nΩ m (*Cryogenic Properties of Copper* 2017). We plot ground plane loss as a function of

frequency in W-Band in Fig. 40b and see that our 503 mm long line will incur ~ 10 dB of loss, which is significant. Therefore, we sputter coat the inside of our package with a 200 nm thick Nb film to avoid conductor loss.

5.4 W-Band Waveguide Feedthrough

5.4.1 Design

To deliver W-Band signals to and from a device under test (DUT) on the 4 K stage of our pulse-tube cooled cryostat, we have developed a cryogenic waveguide feedthrough (Fig. 41) with thermal break and vacuum window designs based on (Melhuish et al. 2016) and (Ediss et al. 2005), respectively. While designed for characterizing our phase shifter and TKIP circuit, this feedthrough is a general purpose system for W-Band measurements and can facilitate further development of the waveguide spectrometer described in Section (cite section of WSpec). Our feedthrough is comprised of two sections separated at the thermal break. The warm and cold sections attach to the cryostat's 300 K and 4 K stages, respectively. Eliminating the need to precisely align small-diameter waveguide sections across a gap, our thermal break employs roughly-aligned conical horns separated by 2.5 mm. The end of the aluminum aligner facing the 4 K stage is open to avoid physical contact between the warm and cold sections with the exception of four nylon alignment screws. Therefore, some signal leakage is expected, but not enough to present a significant stray light issue in the cryostat. We are working on mitigating signal leakage by coating the inner walls of the aligner with absorbing paint, but developing a formula to absorb W-Band frequencies while remaining physically thin has presented some difficulty. For the

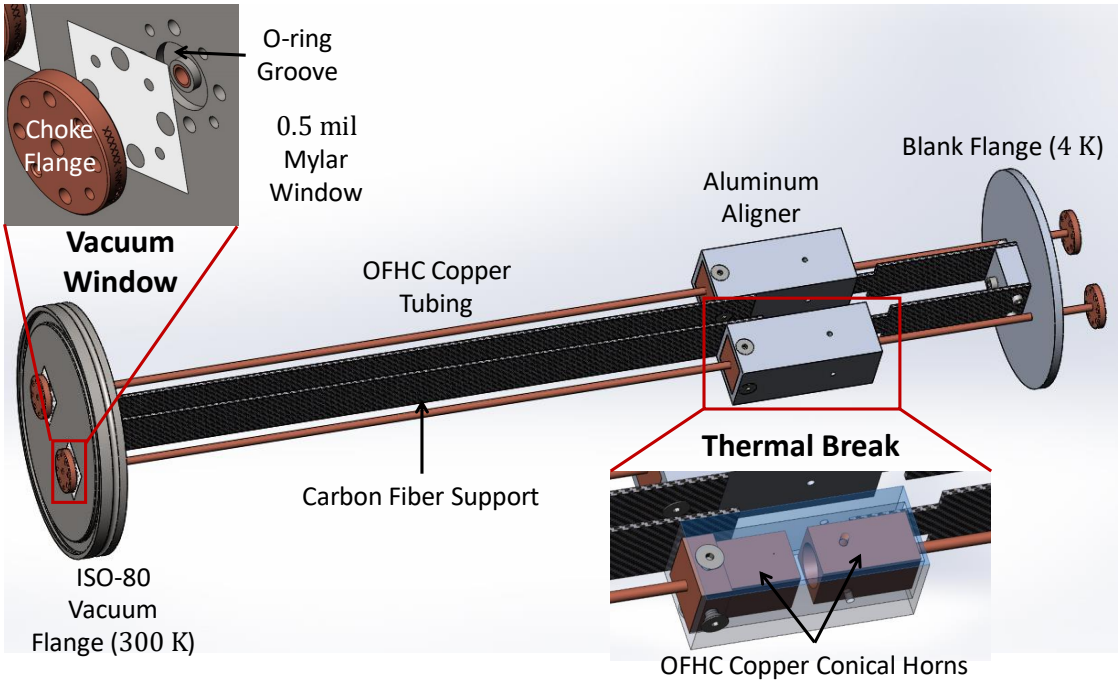

Figure 41: Design of W-Band circular waveguide feedthrough employing a thermal break and vacuum window.

vacuum window, we use 0.5 mil thick mylar as the window material, which has $> 95\%$ transmission across W-Band. This dielectric window creates an open circuit, so we use a waveguide choke flange to transform this open circuit to a short circuit, reducing insertion and return losses incurred due to this discontinuity. Fig. 42a shows our feedthrough mounted in an open cryostat. The input and output legs are connected with a "U" shaped circular waveguide through to measure total system insertion and return loss.

Our waveguide feedthrough is constructed from a combination of commercially available waveguide components and custom-machined parts. The circular waveguide is 0.097 in. diameter copper tubing soldered to standard waveguide flanges from QuinStar.

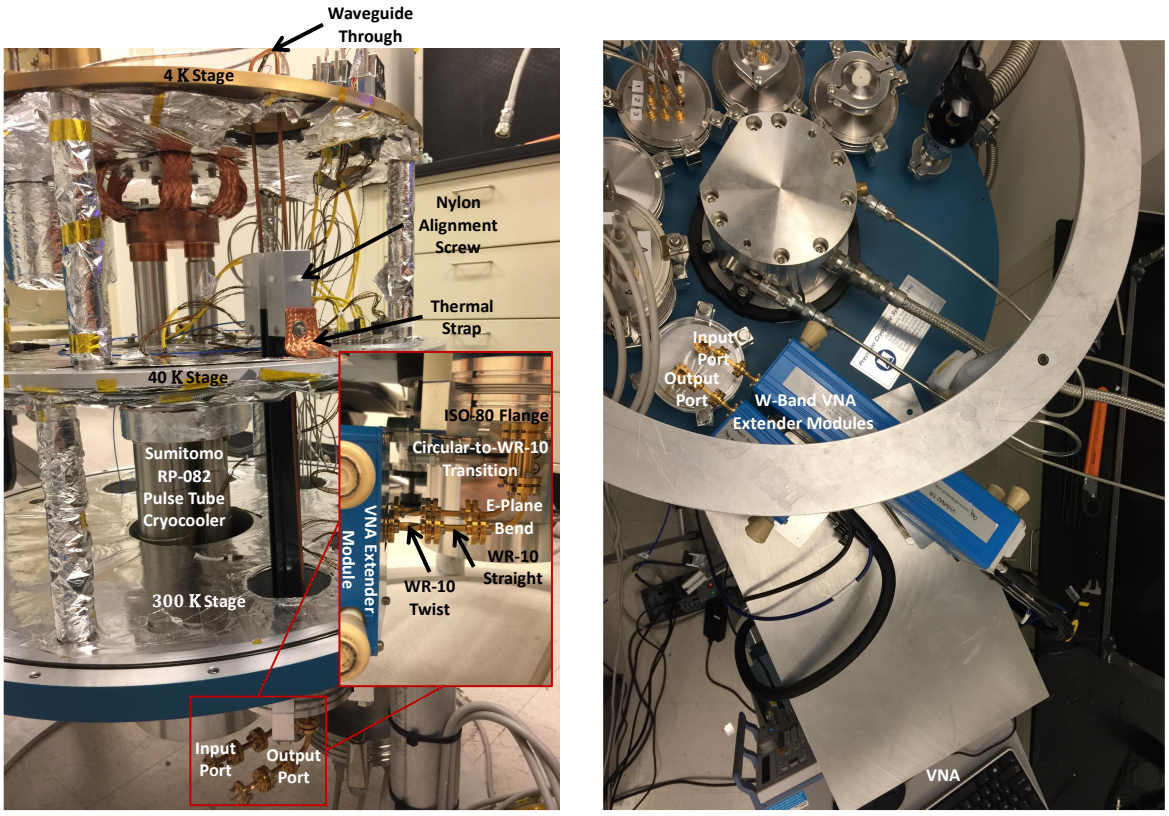

(a) (b)

Figure 42: Waveguide feedthrough installed in our pulse-tube cooled cryostat with closeup of connection between feedthrough and VNA extender modules (a). Setup for cryogenic insertion and return loss measurements (b).

The W-Band horns, carbon fiber support struts, and modifications to the ISO-80 and blank flanges in order to affix waveguide components are all made in the ASU instrument shop. We fabricated the simpler components such as the horn aligners in the ASU student shop. As shown in the closeup in Fig. 42a, we use a series of QuinStar waveguide components to connect our feedthrough with custom circular waveguide to our W-Band VNA extender modules with WR-10 waveguide. Immediately outside the vacuum window is a circular-to-rectangular waveguide transition followed by a 90° E-Plane bend. Space constraints necessitate a straight section of WR-10 and 90° waveguide twist to bridge the gap between the waveguide bend and VNA extender

module, which needs to be on its side. An additional straight section of W-Band circular waveguide connected between the feedthrough and transition would enable access to both circular waveguide polarizations without breaking vacuum.

The DUT must remain ≤ 4 K, so our waveguide feedthrough must minimize heat conduction to the 4 K stage. As shown in Fig. 42a, nylon screws used to align the cold horns result in physical contact between the warm and cold feedthrough sections. To reduce the heat load on the 4 K stage, we use thermal strap to heat sink the aluminum aligners to the 40 K stage, so heat from 300 K is dissipated on this intermediate stage. In our system, heat is conducted from 300 K to 40 K through the two copper tubes with length $L_{\text{tube}} = 0.302$ m and cross-sectional area $A_{\text{tube}} = 3.15 \times 10^{-6}$ m^2. Using data from (Marquardt, Le, and Radebaugh 2000) for copper and assuming RRR = 50, we plot the thermal conductivity $k_{\text{copper}}(T)$ from $T = 4$ K to $T = 300$ K in Fig. 43a. The heat load on the 40 K stage is

$$\dot{Q} = -\frac{2A_{\text{tube}}}{L_{\text{tube}}} \int_{T=300\text{ K}}^{T=40\text{ K}} k_{\text{copper}}(T)\, dT = 2.485\text{ W}, \tag{5.20}$$

which is well below the 45 W cooling capacity of our Sumitomo RP-082 pulse tube's first stage. Heat is conducted from the aligners at 40 K to the 4 K stage through eight 4-40 nylon screws. We choose nylon for its low thermal conductivity as shown in Fig. 43b. The length of conduction is the separation distance between the aligner and cold horn, which is $L_{\text{sep}} = 1.9 \times 10^{-3}$ m. The cross-sectional area of the screw is $A_{\text{screw}} = 6.35 \times 10^{-6}$ m^2, so the heat load on the 4 K stage is

$$\dot{Q} = -\frac{8A_{\text{screw}}}{L_{\text{sep}}} \int_{T=40\text{ K}}^{T=4\text{ K}} k_{\text{nylon}}(T)\, dT = 104\text{ mW}, \tag{5.21}$$

which is an order of magnitude below the 1 W cooling capacity of our pulse tube's second stage. Assuming radiative heat conduction across the thermal break is minimal,

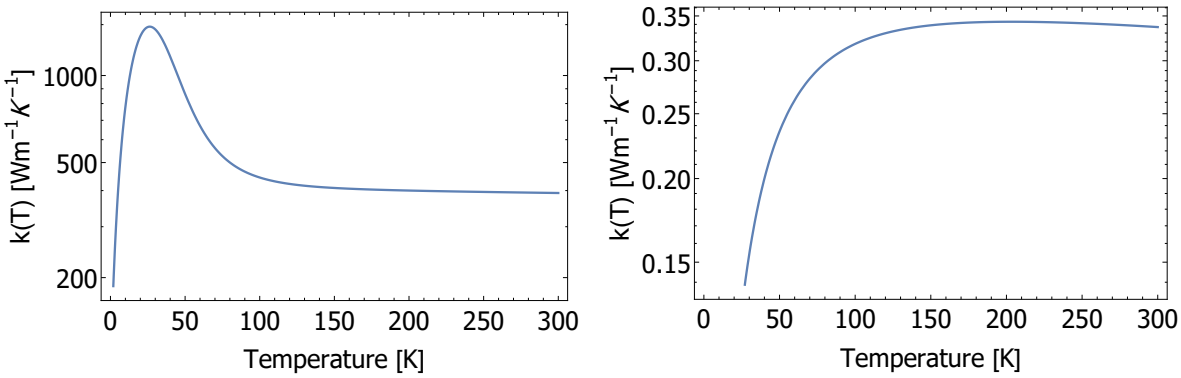

(a) (b)

Figure 43: Thermal conductivity as a function of temperature for copper (a) and polyamide (nylon) (b). Both were computed from cryogenic material properties data from the National Institute of Standards and Technology (Marquardt, Le, and Radebaugh 2000).

the heat load on the 4 K stage should not significantly raise its temperature. For our first cool down with the feedthrough installed, the cold stage reached $T = 3.785$ K.

5.4.2 Calibration Measurement

Using a Rohde&Schwartz ZVA-24 VNA connected to W-Band frequency extender modules from OML, we measure the total insertion and return loss for the complete feedthrough system at both 300 K and 3.785 K to evaluate performance and generate calibration data for W-Band DUT measurements. For these measurements, we drive the extender modules with 10 dBm power level from the VNA's internal source, use 1 Hz measurement bandwidth, and average 25 times. As shown in Fig. 44a, the average insertion and return loss between $75-90$ GHz at 300 K are -18.14 dB and -25.38 dB, respectively. When the cold stage is cooled to 3.785 K, the insertion loss remains the same, but Fig. 44b indicates a return loss increase to -15.55 dB averaged across the

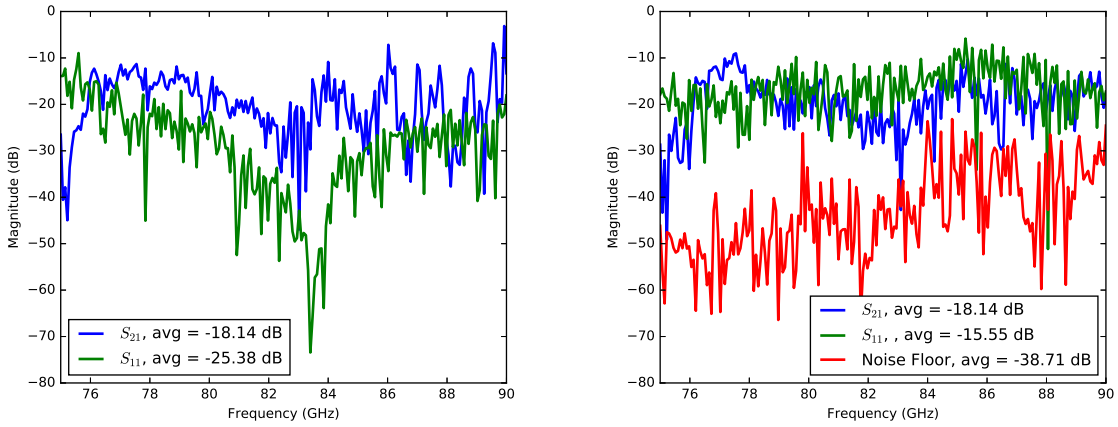

(a) (b)

Figure 44: Measured insertion (S_{21}) and return (S_{11}) loss for waveguide feedthrough at 300 K (a) and 3.785 K (b). The cryogenic measurements include the noise floor of our VNA.

same band. The additional reflection is likely due to a misalignment of the standard waveguide components connecting the feedthrough to the VNA extender modules in the constrained space on top of the cryostat, which is shown in the cryogenic measurement setup in Fig. 42b. We turned off all RF channels to measure a noise floor of −38.71 dB, confirming signal passage through the entire feedthrough. We use these insertion and return loss measurements to calibrate our W-Band feedthrough for testing our phase shifter and TKIP circuit and other DUTs.

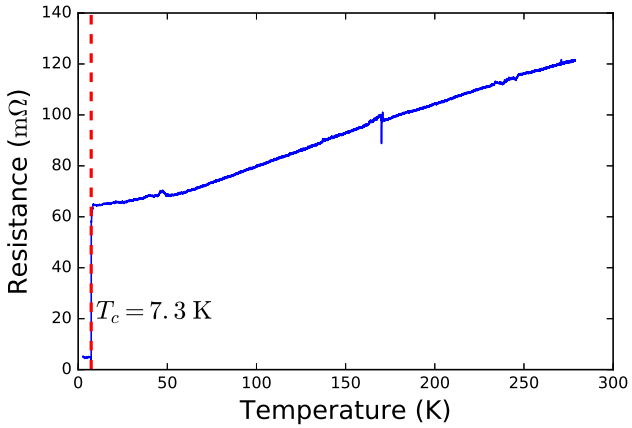

Figure 45: T_c measurement for 200 nm thick Nb film deposited on 1 cm^2 high-resistivity Si sample in ASU NanoFab.

5.5 Phase Shift Measurement

5.5.1 Preparation and Setup

The first time we deposited Nb on a wafer for this project, we included a few 1 cm $\times$ 1 cm, 500 μm thick square Si witness samples for film characterization in the same sputtering chamber. We performed cryogenic four-wire measurements on one of these witness samples to determine the T_c and residual resistance ratio (RRR) of our Nb film. Since we deposited Nb on this sample at a base pressure of $\sim 6 \times 10^{-7}$ Torr instead of at ultra-high vacuum, which is required for pure films, we expect the critical temperature of our Nb film to be lower than its nominal value of 9.2 K due to impurities. A plot of resistance v. temperature is shown in Fig. 45. We measure a critical temperature of $T_c = 7.3$ K and RRR of ~ 2 for our 200 nm thick Nb film.

With the device and package fabricated, the procedure to set up the phase shift measurement is illustrated in Fig. 46. We describe each step below.

(a) As shown in Fig. 46a, the first step is to affix the chip to the Backplate piece of the package at the position where the waveguide ports align to the on-chip radial probes. To attach the chip to the package, we apply epoxy to only a single corner to avoid differential thermal contraction, which would almost inevitably fracture the chip. This is what happened to the first chip we attempted to mount, which is how we were able to produce the closeup view in Fig. 46a. We choose Henkel Loctite STYCAST 2850FT epoxy for its good thermal conductivity, a property essential to cooling the chip to the same temperature as that of the package, which is heat sunk to the 4 K stage as shown in Fig. 46c and therefore below T_c.

(b) To apply DC bias to one of the 503 mm long lines for the phase shift measurement, we need interconnects between the bias tee pads on chip and DC bias pins mounted on the package. Fig. 46b shows our device undergoing wire bonding to form these interconnects with a closeup view of the completed assembly. Because it is difficult to wire bond directly from the pad to the pin, we use an intermediate 50 Ω microstrip line on alumina to facilitate the interconnects. It is worth noting that we must use aluminum wire for these interconnects, because gold will not stick to Nb.

(c) The third and final step is to mount the chip package assembly onto the 4 K stage of our cryostat. As shown in Fig. 46c, we connect the input and output legs of the waveguide feedthrough to the input and output waveguide ports of the chip package using sections of waveguide bent inward to account for the difference in center-to-center distance between input and output waveguide openings at the two interfaces. These bent sections are soldered directly into the chip package and connected to the feedthrough using standard waveguide flanges. We need to solder before mounting the chip in the package, so in order to fit the assembly

on our wire bonding machine, we cut the bent waveguide sections 1 in. from the face of the chip package using wire-cut electrical discharge machining (EDM). To reattach the waveguide, we use a copper tube sleeve with inner diameter of 0.128 in., which is slightly larger than the 0.125 in. outer diameter of our waveguide. The junction is wrapped with aluminum tape with a strong adhesive and good thermal conductivity for heat sinking. We also explicitly heat sink the chip package assembly to the 4 K stage using copper braid wrapped in indium foil as thermal straps. The straps are screwed into both sides using a pyramid of washers to maximize the area of thermal contact. We also mount a diode temperature sensor, which is read out by a cryogenic temperature monitor from LakeShore Cryotronics, directly to the chip package and use a Keithley 2400 series multimeter to source DC current. When this step is complete, we follow the standard procedure for closing the cryostat and turning on the pulse tube to cool our device to below T_c before making measurements.

After wire bonding to form interconnects and closing the chip package, we measured the normal state resistance through the 503 mm long inverted microstrip line with all cabling from the DC bias wire to the Keithley multimeter to be 2.3 MΩ. We periodically checked continuity during the setup procedure to make sure open the wire bonds did not fail. Our setup in Fig. 46c is configured for two different measurements. The first is a measurement of S_{21} across W-Band to verify signal transmission through the device. This measurement would confirm superconductivity of the Nb film and demonstrate the feasibility of fabricating devices employing long ($> 100\lambda$) superconducting transmission lines in the ASU NanoFab. The second is the measurement of non-linear phase shift $\Delta\phi$. With the VNA set to continuous wave (CW) mode, we deliver a 90 GHz tone to

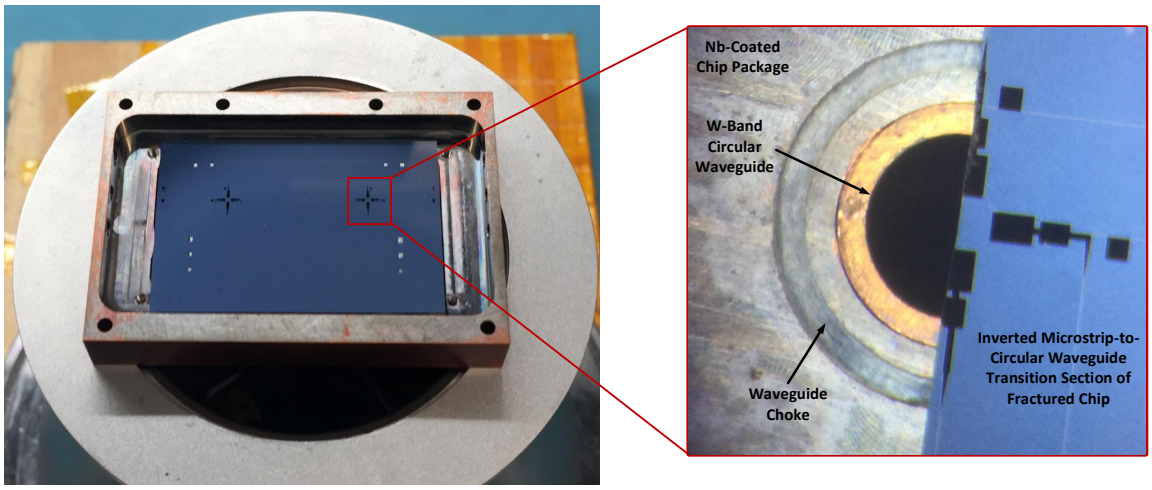

(a)

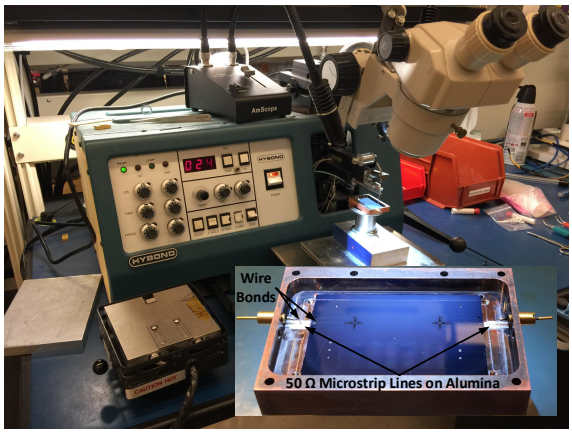

(b)

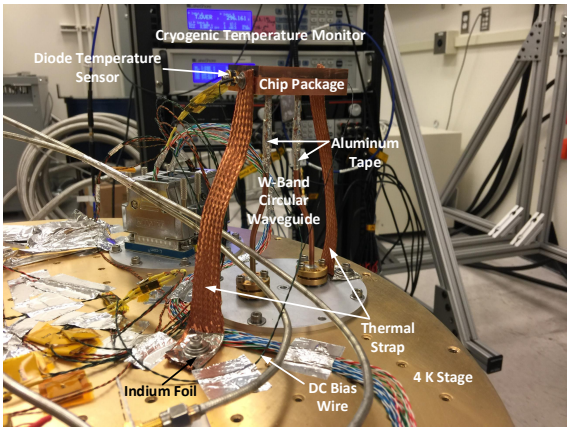

(c)

Figure 46: Steps to prepare for phase shift measurement. Chip epoxy-mounted to package with closeup view of inverted microstrip-to-circular waveguide section of fractured chip showing position of radial probes in waveguide footprint (a). Chip undergoing wire bonding to form interconnects to the package (b). Setup to mount and heat sink chip package assembly to 4 K stage of our cryostat (c).

the feedthrough's input waveguide and sweep the DC current applied to one of the 503 mm long STLs from zero to I_* for Nb to measure $\Delta\phi$ as a function of bias current.

5.5.2 Cooldown 1 Results

Following the procedure outlined in Section 5.5.1, we cooled down the cryostat with a single temperature sensor, labeled "Channel B," mounted to our chip package, using "DC4" as our DC line connected to the Keithley. We continued to periodically check continuity during the cooldown and when the temperature reached below 100 K, there was an open circuit on the DC line. In addition, the chip package did not cool below 8.9 K, indicating poor heat sinking between the 4 K stage and the chip package, which is connected to the waveguide feedthrough. While this chip is from a different wafer than the sample used for our T_c measurement shown in Fig. 45, the Nb film for both wafers was deposited using the same sputtering tool under similar conditions, so we expect T_c to be roughly the same. At 8.9 K, our device did not reach the superconducting state as evidenced by no transmission of W-Band signal power. We then warmed the system back up to 300 K to diagnose our problems. Back at 300 K, the Keithley multimeter once again measured a 2.3 MΩ through resistance on the DC line. We initially hypothesized that our wire bonds broke during the cooling cycle, but upon demounting and opening the chip package, all wire bonds were intact. Therefore, we hypothesized that the open circuit was due to an issue with the "DC4" line and use "DC3", which is proven to be reliable, for the next cooldown.

5.5.3 Cooldown 2 Results

We improved the heat sinking in a number of ways based on past experience with a different cryogenic system. These improvements, which are labeled in yellow in Fig. 47, are as follows:

(a) Replace as many flexible thermal straps with semi-rigid thermal straps made from thin sheets of OFHC copper. These copper sheets have large and flatter areas of thermal contact. We apply these semi-rigid straps to heat sink both the chip package to the 4 K stage and waveguide feedthrough to the 40 K stage.

(b) Use conical spring washers to increase force for better thermal contact. This is especially important for contact between the 4 K stage and blank flange, which is connected to both the chip package and waveguide feedtrhough. We need good heat sinking between our chip package and the 4 K stage, so the chip cools down to the same temperature as the stage.

(c) Block any open areas on both stages of the cryostat with aluminum tape or foil to prevent radiative heat transfer between stages. The waveguide feedthrough leaves open area in both the 40 K and 4 K stages, so the 4 K stage is exposed to radiative heat load from 300 K. We blocked these open areas as much as possible.

For cooldown 1, we had a single working temperature sensor mounted to our chip package. A second temperature sensor, labeled "Channel A," did not read properly due to a cold solder joint. We resoldered the cable for "Channel A" and mounted it directly onto the 4 K stage, so we can simultaneously monitor the temperature on the stage and chip package. With the cryostat open, "Channel A" and "Channel B" read 294 K and 296 K, respectively. Using "DC3" this time, we measured a through resistance of 1.6 MΩ at 300 K and periodically performed this continuity test while closing up the cryostat for cooldown 2. Once again, the Keithley indicated an open circuit when the temperature dropped below 100 K. Since we used a different DC line, which has proven reliability, the open circuit is likely occurring on chip rather than in the DC

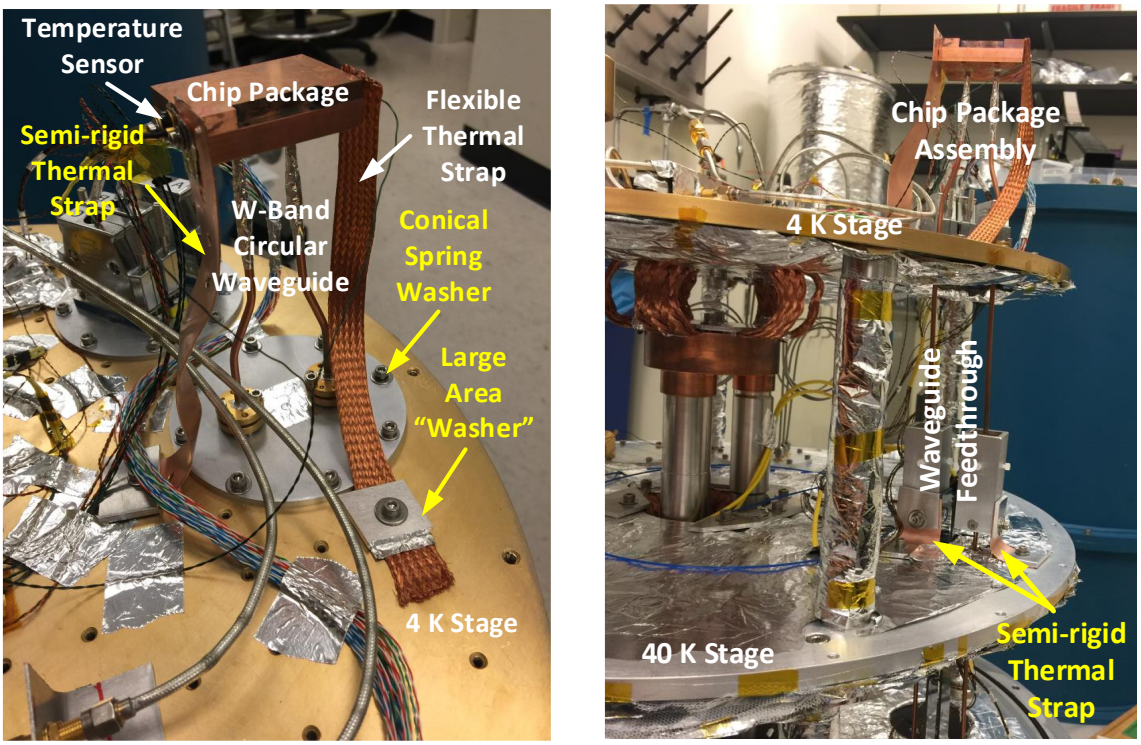

(a) (b)

Figure 47: Improved heat sinking for mounting chip package assembly to 4 K stage (a) and waveguide feedthrough to 40 K stage. Improvements compared to setup in Fig. 46 are labeled in yellow.

feedthroughs. Our changes to improve heat sinking did result in a "Channel B" reading of 7.15 K for the chip package, a ~ 2 K improvement over Cooldown 1. "Channel A" read a temperature of 3.99 K on the 4 K stage, which is comparable to that achieved when the system was cooled to test just the waveguide feedthrough. However, this temperature is still significantly higher the ~ 2.7 K achieved before the feedthrough was installed. The most likely source of heat reaching the 4 K stage is the nylon screws that align the cold and warm horns of the thermal break. Redesigning this alignment apparatus to further minimize heat conduction between the warm and cold sides of the thermal break is an avenue to explore. Also, even though the chip package reached

a temperature below the nominal T_c of Nb deposited in the ASU NanoFab, we still observed no W-Band signal transmission through the device when we measured S_{21}. The Nb on this particular chip may have a lower T_c or the STYCAST 2850FT epoxy may provide insufficient heat sinking to the chip package, both of which would prevent the Nb from reaching the superconducting state. Therefore, the next cooldown will be dedicated to obtaining an accurate measurement of T_c on this particular chip before we proceed to making another attempt at measuring phase shift. In addition, we will add two more DC wires, enabling the standard four-wire measurement capability.

5.6 Summary

We have designed a dual-purpose superconducting circuit to provide proof-of-concept for a W-Band TKIP and current-controlled differential phase shifter that can operate as an on-chip FTS, two key technologies for the next generation of astronomy at W-Band frequencies. We have also fabricated a Nb prototype of this circuit and assembled a measurement setup to verify a predicted phase shift of $\Delta\phi \approx 30$ rad when one of a pair of symmetric STLs is biased near the critical current. After two attempts, we have not yet achieved a successful measurement of $\Delta\phi$, but have gained insight into addressing flaws in both the chip design itself and measurement setup. In addition, our two cooldowns helped us identify ways to improve our cryogenic system as a whole with regard to heat sinking, thermal insulation, and general configuration of its subsystems. Addressing these issues before our previously planned installation of a newly designed sub-Kelvin stage will significantly improve our system's overall capability to efficiently characterize all future devices.

There are two paths forward toward measuring $\Delta\phi$. We can continue with our

existing Nb chip or outsource fabrication to a facility that produces good NbTiN films to obtain a NbTiN device as originally designed. Successful measurement of $\Delta\phi$ with our Nb chip would verify one mode of device operation and demonstrate the feasibility of fabricating future TKIP devices in the ASU NanoFab. However, it is reasonable to conclude that there is a significantly greater probability of success for a NbTiN chip because the design is optimized for this material. For whichever path we chose, a successful measurement would bring us one step closer to an optimized W-Band TKIP. When a NbTiN chip made, its FTS mode of operation will also be thoroughly explored.

Chapter 6

SUMMARY AND FUTURE WORK

We have contributed significant electromagnetic design, device fabrication, and cryogenic testing efforts to fulfill technological needs that will make the next generation of millimeter-wave astronomy possible. These needs include dual-polarization KID arrays for both star formation and cosmic microwave background studies, compact filter bank spectrometers designed to conduct broadband spectral surveys at millimeter wavelengths over large areas of the sky, and parametric amplifiers with the potential to achieve quantum-noise limited noise performance and improve upon instantaneous bandwidth and gain compared to solid state low noise amplifiers such as high electron mobility transistor amplifiers.

For our contribution to the Columbia University-led effort to demonstrate large arrays of dual-polarization KIDs for ground-based CMB polarimetry at 150 GHz, we fabricated numerous arrays of aluminum KIDs. However, only a few chips have been tested because we do not yet have a robust sub-Kelvin stage in our cryostat here at ASU. The devices that have been tested were tested in the cryogenic testbed at Columbia. We are currently developing a stage capable of reaching 100 mK and making general improvements to our system as a whole. These aluminum devices will be some of the first we test after fully assembling and integrating the sub-Kelvin stage. Having full capability to design, fabricate, and test devices in-house at ASU will greatly facilitate future prototyping of novel devices and performing detailed measurements on existing devices.

The W-Band cryogenic waveguide feedthrough developed for testing our phase

shifter/TKIP circuit is a general purpose enhancement to our cryogenic testbed that expands its capability to characterize devices operating in W-Band. The other main W-Band device we discussed in this dissertation is our 5-channel prototype for WSpec. The feedthrough enables cryogenic testing of this prototype with or without integrated arrays of KIDs, further advancing this novel implementation of filter bank spectrometer technology that complements its on-chip counterparts such as SuperSpec and DESHIMA. Our feedthrough is potentially scalable to higher frequencies, but further investigation is necessary to determine how much additional electromagnetic loss would be incurred. In addition, since WSpec implements the same filter bank circuit as SuperSpec, just in a different choice of propagation medium, we can apply our lumped element model to inform future designs of WSpec devices. The same fitting procedure can be used to map lumped circuit elements to physical dimensions in full wave HFSS simulations for log-spaced filter bank devices.

With a plethora of promising technologies on the horizon, the future of millimeter-wave astronomy is extremely bright. All of the work conducted for this dissertation focuses on the subset of these technologies based on kinetic inductance, a simple physical phenomenon exhibited by superconductors. This intersection of nature and human ingenuity has led to the development of technologies with the potential to revolutionize an entire scientific discipline. We greatly look forward to the wealth of scientific knowledge to be gained from observations enabled by these technologies, which will substantially enhance our understanding of our universe from the Big Bang to today.

REFERENCES

Adamyan, A. A., S. E. De Graaf, S. E. Kubatkin, and A. V. Danilov. 2016. "Superconducting microwave parametric amplifier based on a quasi-fractal slow propagation line." *J. Appl. Phys.* 119 (8). doi:10.1063/1.4942362.

Ade, P. A.R., R. W. Aikin, D. Barkats, S. J. Benton, C. A. Bischoff, J. J. Bock, J. A. Brevik, et al. 2014. "Detection of B -mode polarization at degree angular scales by BICEP2." *Phys. Rev. Lett.* 112 (24): 1–25. doi:10.1103/PhysRevLett.112.241101. arXiv: 1403.3985.

Akgiray, Ahmed H., Sander Weinreb, Rémy Leblanc, Michel Renvoise, Peter Frijlink, Richard Lai, and Stephen Sarkozy. 2013. "Noise measurements of discrete HEMT transistors and application to wideband very low-noise amplifiers." *IEEE Trans. Microw. Theory Tech.* 61 (9): 3285–3297. doi:10.1109/TMTT.2013.2273757.

Anlage, S. M., H. J. Snortland, and M. R. Beasley. 1989. "Current controlled variable delay superconducting transmission line." *IEEE Trans. Magn.* 25 (2): 1388–1391. doi:10.1109/20.92554.

Audley, Michael D., Gert De Lange, Jian Rong Gao, Pourya Khosropanah, Richard Hijmering, Marcel Ridder, Philip D. Mauskopf, Dmitry Morozov, Neil A. Trappe, and Stephen Doherty. 2016. "Optical performance of an ultra-sensitive horn-coupled transition-edge-sensor bolometer with hemispherical backshort in the far infrared." *Rev. Sci. Instrum.* 87 (4). doi:10.1063/1.4945302.

Balanis, Constantine. 2012. *Advanced Engineering Electromagnetics.* 2nd. Danvers, MA: John Wiley & Sons, Inc.

Bardeen, J., L. N. Cooper, and J. R. Schrieffer. 1957. "Theory of superconductivity." *Phys. Rev.* 108 (5): 1175–1204. doi:10.1103/PhysRev.108.1175. arXiv: 1101.0277.

Bardin, J. C., S. Montazeri, and Su Wei Chang. 2017. "Silicon Germanium Cryogenic Low Noise Amplifiers." *J. Phys. Conf. Ser.* 834 (1). doi:10.1088/1742-6596/834/1/012007.

Barry, P S, E Shirokoff, A Kov·cs, T J Reck, S Hailey-Dunsheath, C M McKenney, L J Swenson, et al. 2012. "Electromagnetic design for SuperSpec: a lithographically-patterned millimetre-wave spectrograph." In *Soc. Photo-Optical Instrum. Eng. Conf. Ser.* Vol. 8452. doi:10.1117/12.927089.

Barry, Peter Stuart. 2014. "On the development of SuperSpec ; a Fully Integrated On-chip Spectrometer for Far-infrared Astronomy." PhD Dissertation, Cardiff University.

Baselmans, J. J. A., J. Bueno, S. J. C. Yates, O. Yurduseven, N. Llombart, K. Karatsu, A. M. Baryshev, et al. 2016. "A kilo-pixel imaging system for future space based far-infrared observatories using microwave kinetic inductance detectors." *Astron. Astrophys.* 89:1–16. doi:10.1051/0004-6361/201629653. arXiv: 1609.01952.

Bespalov, Anton, Manuel Houzet, Julia S. Meyer, and Yuli V. Nazarov. 2016. "Theoretical Model to Explain Excess of Quasiparticles in Superconductors." *Phys. Rev. Lett.* 117 (11): 1–5. doi:10.1103/PhysRevLett.117.117002. arXiv: 1603.04273.

Beyer, Andrew D., M. Kenyon, P. M. Echternach, B. Bumble, M. C. Runyan, T. Chui, C. M. Bradford, W. A. Holmes, and J. J. Bock. 2012. "Development of fast, background-limited transition-edge sensors for the background-limited infrared/sub-mm spectrograph (BLISS) for SPICA." In *Proc. SPIE,* vol. 8452, 84520G. doi:10.1117/12.926326.

Bockstiegel, C., J. Gao, M. R. Vissers, M. Sandberg, S. Chaudhuri, A. Sanders, L. R. Vale, K. D. Irwin, and D. P. Pappas. 2014. "Development of a broadband NbTiN traveling wave parametric amplifier for MKID readout." *J. Low Temp. Phys.* 176 (3-4): 476–482. doi:10.1007/s10909-013-1042-z.

Bradford, C. Matt, Peter A. R. Ade, James E. Aguirre, James J. Bock, Mark Dragovan, Lionel Duband, Lieko Earle, et al. 2004. "Z-Spec: a broadband millimeter-wave grating spectrometer: design, construction, and first cryogenic measurements." In *Proc. SPIE,* 257. October 2004. doi:10.1117/12.552182.

Bryan, Sean. 2014. "Half-wave Plates for the Spider Cosmic Microwave Background Polarimeter." PhD Dissertation, Case Western Reserve University. arXiv: 1402.2591. http://arxiv.org/abs/1402.2591.

Bryan, Sean, James Aguirre, George Che, Simon Doyle, Daniel Flanigan, Christopher Groppi, Bradley Johnson, et al. 2016. "WSPEC: A Waveguide Filter-Bank Focal Plane Array Spectrometer for Millimeter Wave Astronomy and Cosmology." *J. Low Temp. Phys.* 184 (1-2): 114–122. doi:10.1007/s10909-015-1396-5. arXiv: 1509.04658.

Bryan, Sean, George Che, Christopher Groppi, Philip Mauskopf, and Matthew Underhill. 2015. "A Compact Filter-Bank Waveguide Spectrometer for Millimeter Wavelengths." *IEEE Trans. Terahertz Sci. Technol.* 5 (4): 598–604. doi:10.1109/TTHZ.2015.2433919. arXiv: 1502.02735.

Bueno, J., P. C.J.J. Coumou, G. Zheng, P. J. De Visser, T. M. Klapwijk, E. F.C. Driessen, S. Doyle, and J. J.A. Baselmans. 2014. "Anomalous response of superconducting titanium nitride resonators to terahertz radiation." *Appl. Phys. Lett.* 105 (19). doi:10.1063/1.4901536. arXiv: 1408.0270.

Bueno, J., O. Yurduseven, S. J.C. Yates, N. Llombart, V. Murugesan, D. J. Thoen, A. M. Baryshev, A. Neto, and J. J.A. Baselmans. 2017. "Full characterisation of a background limited antenna coupled KID over an octave of bandwidth for THz radiation." *Appl. Phys. Lett.* 110 (23). doi:10.1063/1.4985060.

Bueno, Juan, Ozan Yurduseven, Stephen J.C. Yates, Nuria Llombart, Vignesh Murugesan, David J. Thoen, Andrey M. Baryshev, Andrea Neto, and Jochem J.A. Baselmans. 2016. "Photon noise limited performance over an octave of bandwidth of kinetic inductance detectors for sub-millimeter astronomy." In *Int. Conf. Infrared, Millimeter, Terahertz Waves, IRMMW-THz,* vol. 2016-Novem, 1–2. doi:10.1109/IRMMW-THz.2016.7758429.

Burnett, J., T. Lindström, M. Oxborrow, Y. Harada, Y. Sekine, P. Meeson, and a. Tzalenchuk. 2013. "Slow noise processes in superconducting resonators." *Phys. Rev. B* 87 (14): 140501. doi:10.1103/PhysRevB.87.140501. arXiv: arXiv:1210.2351v3.

Carlstrom, J. E., P. A. R. Ade, K. A. Aird, B. A. Benson, L. E. Bleem, S. Busetti, C. L. Chang, et al. 2011. "The 10 Meter South Pole Telescope." *Publ. Astron. Soc. Pacific* 123 (903): 568–581. doi:10.1086/659879. arXiv: 0907.4445.

Catalano, A., R. Adam, P. Ade, P. André, H. Aussel, A. Beelen, A. Benoît, et al. 2016. "The NIKA2 commissioning campaign: performance and first results." In *Proc. SPIE.* arXiv: 1605.08628. http://arxiv.org/abs/1605.08628.

Caves, Carlton M. 1982. "Quantum limits on noise in linear amplifiers." *Phys. Rev. D* 26 (8): 1817–1839. doi:10.1103/PhysRevD.26.1817. arXiv: 1208.5174.

Chaudhuri, S., D. Li, K. D. Irwin, C. Bockstiegel, J. Hubmayr, J. N. Ullom, M. R. Vissers, and J. Gao. 2017. "Broadband parametric amplifiers based on nonlinear kinetic inductance artificial transmission lines." *Appl. Phys. Lett.* 110 (15). doi:10.1063/1.4980102. arXiv: 1704.00859.

Chaudhuri, Saptarshi, Jiansong Gao, and Kent Irwin. 2015. "Simulation and analysis of superconducting traveling-wave parametric amplifiers." *IEEE Trans. Appl. Supercond.* 25 (3). doi:10.1109/TASC.2014.2378059. arXiv: 1412.2372.

Coppolecchia, A, G Amico, E.S. Battistelli, P De Bernardis, A Cruciani, and A. D'addabbo. 2013. "OLIMPO: A 4-bands imaging spectro-photometer for balloon-

borne observations of the Sunyaev-Zel-dovich effect." In *Int. Sch. Phys. "Enrico Fermi",* 257–264. doi:10.3254/978-1-61499-476-3-257.

Coumou, P. C J J, E. F C Driessen, J. Bueno, C. Chapelier, and T. M. Klapwijk. 2013. "Electrodynamic response and local tunneling spectroscopy of strongly disordered superconducting TiN films." *Phys. Rev. B - Condens. Matter Mater. Phys.* 88 (18): 1–5. doi:10.1103/PhysRevB.88.180505. arXiv: 1310.3176.

Coumou, P. C J J, M. R. Zuiddam, E. F C Driessen, P. J. De Visser, J. J A Baselmans, and T. M. Klapwijk. 2013. "Microwave properties of superconducting atomic-layer deposited TiN films." *IEEE Trans. Appl. Supercond.* 23 (3): 1–4. doi:10.1109/TASC.2012.2236603. arXiv: 1212.4434.

Cowen, R. 2015. "Gravitational waves discovery now officially dead." *Nature* (January). https://www.nature.com/news/gravitational-waves-discovery-now-officially-dead-1.16830.

Cryogenic Properties of Copper. 2017. Accessed December 1. https://www.copper.org/resources/properties/cryogenic/.

Cuadrado-Calle, David, Danielle George, Gary A. Fuller, Kieran Cleary, Lorene Samoska, Pekka Kangaslahti, Jacob W. Kooi, et al. 2017. "Broadband MMIC LNAs for ALMA Band 2+3 with Noise Temperature below 28 K." *IEEE Trans. Microw. Theory Tech.* 65 (5): 1589–1597. doi:10.1109/TMTT.2016.2639018.

Datta, R., J. Hubmayr, C. Munson, J. Austermann, J. Beall, D. Becker, H. M. Cho, et al. 2014. "Horn coupled multichroic polarimeters for the atacama cosmology telescope polarization experiment." *J. Low Temp. Phys.* 176 (5-6): 670–676. doi:10.1007/s10909-014-1134-4. arXiv: arXiv:1401.8029v1.

Day, Peter K., Henry G. Leduc, Benjamin A. Mazin, Anastasios Vayonakis, and Jonas Zmuidzinas. 2003. "A broadband superconducting detector suitable for use in large arrays." *Nature* 425 (October): 817–821. doi:10.1038/nature01981.1..

De Visser, P. J., J. J.A. Baselmans, P. Diener, S. J.C. Yates, A. Endo, and T. M. Klapwijk. 2012. "Generation-recombination noise: The fundamental sensitivity limit for kinetic inductance detectors." *J. Low Temp. Phys.* 167 (3-4): 335–340. doi:10.1007/s10909-012-0519-5.

Denis, Kevin L., Ari David Brown, Meng Ping Chang, Ron Hu, Karwan Rostem, Kongpop U-Yen, and Edward J. Wollack. 2017. "Fabrication of Superconducting Vacuum-Gap Crossovers for High Performance Microwave Applications." *IEEE*

Trans. Appl. Supercond. 27 (4): 4–7. doi:10.1109/TASC.2016.2646917. arXiv: 1610.01197.

Devlin, Mark J., Peter A.R. Ade, Itziar Aretxaga, James J. Bock, Edward L. Chapin, Matthew Griffin, Joshua O. Gundersen, et al. 2009. "Over half of the far-infrared background light comes from galaxies." *Nature* 458 (7239): 737–739. doi:10.1038/nature07918. arXiv: 0904.1201.

Dober, B., J. A. Austermann, J. A. Beall, D. Becker, G. Che, H. M. Cho, M. Devlin, et al. 2016. "Optical Demonstration of THz, Dual-Polarization Sensitive Microwave Kinetic Inductance Detectors." *J. Low Temp. Phys.* 184 (1-2): 173–179. doi:10.1007/s10909-015-1434-3. arXiv: 1603.02963.

Doyle, Simon. 2008. "Lumped Element Kinetic Inductance Detectors." PhD Dissertation, Cardiff University.

Earle, L., P. Ade, J. Aguirre, R. Aikin, J. Battle, J. Bock, C. M. Bradford, et al. 2006. "Z-Spec: a broadband direct-detection millimeter-wave spectrometer – instrument status and first results." In *Proc. SPIE,* 1:627510–627510–9. 626. doi:10.1117/12.672309.

Ediss, G a, N Horner, F Johnson, D Koller, and a R Kerr. 2005. *WR-10 Waveguide Vacuum Feedthrough for the ALMA Band-6 Cartridge.* Technical report. National Radio Astronomy Observatory. https://science.nrao.edu/facilities/alma/aboutALMA/Technology/ALMA%7B%5C_%7DMemo%7B%5C_%7DSeries/alma536/memo536.pdf.

Elmegreen, Bruce G., and John Scalo. 2004. "Interstellar Turbulence I: Observations and Processes." *Annu. Rev. Astron. Astrophys.* 42:211–273. doi:10.1146/annurev.astro.41.011802.094859. arXiv: 0404451 [astro-ph].

Endo, A., J. J. A. Baselmans, P. P. van der Werf, B. Knoors, S. M. H. Javadzadeh, S. J. C. Yates, D. J. Thoen, et al. 2012. "Development of DESHIMA: a redshift machine based on a superconducting on-chip filterbank." In *Proc. SPIE,* 84520X. September 2012. doi:10.1117/12.925637.

Essinger-Hileman, Thomas. 2011. "Probing Inflationary Cosmology: The Atacama B-Mode Search (ABS)." PhD Dissertation, Princeton University. http://adsabs.harvard.edu/cgi-bin/nph-data%7B%5C_%7Dquery?bibcode=2011PhDT.....44E%7B%5C&%7Dlink%7B%5C_%7Dtype=ABSTRACT%7B%5C%%7D5Cnpapers3://publication/uuid/10FFEF8E-8B42-42F8-9A67-EC8795C4C349.

Faber, T. E., and A. B. Pippard. 1955. "The Penetration Depth and High-Frequency Resistance of Superconducting Aluminium." *Proc. R. Soc. A Math. Phys. Eng. Sci.* 231 (1186): 336–353. doi:10.1098/rspa.1955.0178.

Fan, L., M.-Y. Li, and K. Chang. 1995. "Circular waveguide-to-microstrip transitions." *Electron. Lett.* 31 (4): 294. doi:10.1049/el:19950171.

Faoro, Lara, and Lev B. Ioffe. 2015. "Interacting tunneling model for two-level systems in amorphous materials and its predictions for their dephasing and noise in superconducting microresonators." *Phys. Rev. B - Condens. Matter Mater. Phys.* 91 (1): 1–11. doi:10.1103/PhysRevB.91.014201. arXiv: 1404.2410.

Ferkinhoff, Carl, Thomas Nikola, Stephen C. Parshley, Gordon J. Stacey, Kent D. Irwin, Hsiao-Mei Cho, and Mark Halpern. 2010. "ZEUS-2: a second generation submillimeter grating spectrometer for exploring distant galaxies." In *Proc. SPIE,* vol. 7741, 77410Y–77410Y–14. 607. doi:10.1117/12.857018. arXiv: 1010.1439.

Fissel, Laura M., Peter A. R. Ade, Francesco E. Angilè, Peter Ashton, Steven Benton, Mark J. Devlin, Bradley Dober, et al. 2015. "Balloon-Borne Submillimeter Polarimetry of the Vela C Molecular Cloud: Systematic Dependence of Polarization Fraction on Column Density and Local Polarization-Angle Dispersion." *Astrophys. J.* 824 (134): 1–21. doi:10.3847/0004-637X/824/2/134. arXiv: 1509.05298.

Fissel, Laura M., Peter a. R. Ade, Francesco E. Angile, Steven J. Benton, Edward L. Chapin, Mark J. Devlin, Natalie N. Gandilo, et al. 2010. "The balloon-borne large-aperture submillimeter telescope for polarimetry: BLAST-Pol," 14. doi:10.1117/12.788413. arXiv: 1007.1390.

Flanigan, D., H. McCarrick, G. Jones, B. R. Johnson, M. H. Abitbol, P. Ade, D. Araujo, et al. 2016. "Photon noise from chaotic and coherent millimeter-wave sources measured with horn-coupled, aluminum lumped-element kinetic inductance detectors." *Appl. Phys. Lett.* 108 (8). doi:10.1063/1.4942804. arXiv: 1510.06609.

Frieman, Joshua, Michael Turner, and Dragan Huterer. 2008. "Dark Energy and the Accelerating Universe." *Annu. Rev. Astron. Astrophys.* 46:385–434. doi:10.1146/annurev.astro.46.060407.145243. arXiv: 0803.0982.

Galitzki, Nicholas, Peter a. R. Ade, Fe Angilè, Peter Ashton, James Beall, and Dan Becker. 2014. "The Next Generation BLAST Experiment." *J. Astron. Instrum.* 3 (215): 1–19. doi:10.1142/S2251171714400017. arXiv: 1409.7084.

Gao, J, M R Vissers, M O Sandberg, F C S Silva, S W Nam, and D P Pappas. 2013. "A titanium-nitride near-infrared kinetic inductance photon-counting detector and its anomalous electrodynamics." *Appl. Phys. Lett.* 2 (2012): 4.

Gao, Jiansong. 2008. "The physics of superconducting microwave resonators." PhD Dissertation, California Institute of Technology. http://www.submm.caltech.edu/%7B~%7Djonas/Theses/Jiansong%7B%5C_%7DGao%7B%5C_%7D08.pdf.

Gao, Jiansong, Miguel Daal, John M. Martinis, Anastasios Vayonakis, Jonas Zmuidzinas, Bernard Sadoulet, Benjamin A. Mazin, Peter K. Day, and Henry G. Leduc. 2008. "A semiempirical model for two-level system noise in superconducting microresonators." *Appl. Phys. Lett.* 92 (21): 1–4. doi:10.1063/1.2937855. arXiv: 0804.0467.

Gao, Jiansong, Miguel Daal, Anastasios Vayonakis, Shwetank Kumar, Jonas Zmuidzinas, Bernard Sadoulet, Benjamin A. Mazin, Peter K. Day, and Henry G. Leduc. 2008. "Experimental evidence for a surface distribution of two-level systems in superconducting lithographed microwave resonators." *Appl. Phys. Lett.* 92 (15). doi:10.1063/1.2906373. arXiv: 0802.4457.

Garg, Ramesh, Prakash Bhartia, Inder Bahl, and Apisak Ittipiboon. 2001. *Microstrip Antenna Design Handbook.* Norwood, MA: Artech House.

Goddard, D. E., and D. K. Milne. 1994. *Parkes: Thirty Years of Radio Astronomy.* Collingwood: Commonwealth Scientific / Industrial Research Organization.

Goldie, D. J., and S. Withington. 2012. "Non-equilibrium superconductivity in quantum-sensing superconducting resonators." *Supercond. Sci. Technol.* 26 (1). doi:10.1088/0953-2048/26/1/015004. arXiv: 1208.0685 [cond-mat.supr-con].

Göppl, M., A. Fragner, M. Baur, R. Bianchetti, S. Filipp, J. M. Fink, P. J. Leek, G. Puebla, L. Steffen, and A. Wallraff. 2008. "Coplanar waveguide resonators for circuit quantum electrodynamics." *J. Appl. Phys.* 104 (11). doi:10.1063/1.3010859. arXiv: 0807.4094.

Gordon, Samuel, Brad Dober, Adrian Sinclair, Samuel Rowe, Sean Bryan, Philip Mauskopf, Jason Austermann, et al. 2016. "An Open Source, FPGA-Based LeKID Readout for BLAST-TNG: Pre-Flight Results." *J. Astron. Instrum.* 05 (04): 1641003. doi:10.1142/S2251171716410038. arXiv: 1611.05400.

Grayson, J. A., P. A. R. Ade, Z. Ahmed, K. D. Alexander, M. Amiri, D. Barkats, S. J. Benton, et al. 2016. "BICEP3 performance overview and planned Keck Array upgrade." In *Proc. SPIE,* 99140S. doi:10.1117/12.2233894. arXiv: 1607.04668.

Griffin, Matthew J, James J Bock, and Walter K Gear. 2002. "Relative performance of filled and feedhorn-coupled focal-plane architectures." *Appl. Opt.* 41, no. 31 (November): 6543–54. http://www.ncbi.nlm.nih.gov/pubmed/12412645.

Guruswamy, T., C. N. Thomas, S. Withington, and D. J. Goldie. 2017. "Electrothermal feedback in kinetic inductance detectors." *Supercond. Sci. Technol.* 30 (6). doi:10.1088/1361-6668/aa68ab. arXiv: 1701.09145.

Guth, Alan H., David I. Kaiser, and Yasunori Nomura. 2014. "Inflationary paradigm after Planck 2013." *Phys. Lett. Sect. B Nucl. Elem. Part. High-Energy Phys.* 733:112–119. doi:10.1016/j.physletb.2014.03.020. arXiv: 1312.7619.

Hailey-Dunsheath, S., P. S. Barry, C. M. Bradford, G. Chattopadhyay, P. Day, S. Doyle, M. Hollister, et al. 2014. "Optical measurements of SuperSpec: A millimeter-wave on-chip spectrometer." *J. Low Temp. Phys.* 176 (5-6): 841–847. doi:10.1007/s10909-013-1068-2.

Hailey-Dunsheath, S., T. Nikola, G. J. Stacey, T. E. Oberst, S. C. Parshley, C. M. Bradford, P. a. R. Ade, and C. E. Tucker. 2008. "Detection of the 13CO(J=6-5) Transition in the Starburst Galaxy NGC 253." *Astrophys. J.* 4. doi:10.1086/595840. arXiv: 0810.4514.

Hailey-Dunsheath, S., E. Shirokoff, P. S. Barry, C. M. Bradford, S. Chapman, G. Che, J. Glenn, et al. 2016. "Low Noise Titanium Nitride KIDs for SuperSpec: A Millimeter-Wave On-Chip Spectrometer." *J. Low Temp. Phys.* 184 (1-2): 180–187. doi:10.1007/s10909-015-1375-x. arXiv: 1511.04488.

Hailey-Dunsheath, Steve. 2017. *Photon Noise and Optical Response.* Technical report. Pasadena, CA: California Institute of Technology.

Hailey-Dunsheath, Steven. 2009. "Probing star formation at low and high redshift with ZEUS, a new submillimeter grating spectrometer." PhD Dissertation, Cornell University. http://adsabs.harvard.edu/abs/2009PhDT.....4H.

———. 2016. *Log-Spaced Filter Bank Optimization.* Technical report. Pasadena, CA: California Institute of Technology.

———. 2017. *Log-Spaced Filter Bank Optimization Update.* Technical report. Pasadena, CA: California Institute of Technology.

Hansryd, Jonas, Peter A. Andrekson, Mathias Westlund, Jie Li, and Per Olof Hedekvist. 2002. "Fiber-based optical parametric amplifiers and their applications." *IEEE J. Sel. Top. Quantum Electron.* 8 (3): 506–520. doi:10.1109/JSTQE.2002.1016354.

Ho Eom, Byeong, Peter K. Day, Henry G. Leduc, and Jonas Zmuidzinas. 2012. "A wideband, low-noise superconducting amplifier with high dynamic range." *Nat. Phys. Suppl. Inf.* doi:10.1038/nphys2356. arXiv: 1201.2392.

Ho Eom, Byeong, Peter K. Day, Henry G. LeDuc, and Jonas Zmuidzinas. 2012. "A wideband, low-noise superconducting amplifier with high dynamic range." *Nat. Phys.* 8 (8): 623–627. doi:10.1038/nphys2356. arXiv: 1201.2392.

Holland, W. S., D. Bintley, E. L. Chapin, A. Chrysostomou, G. R. Davis, J. T. Dempsey, W. D. Duncan, et al. 2013. "SCUBA-2: The 10 000 pixel bolometer camera on the James Clerk Maxwell Telescope." *Mon. Not. R. Astron. Soc.* 430 (4): 2513–2533. doi:10.1093/mnras/sts612. arXiv: 1301.3650.

Hubmayr, J, J Beall, D Becker, H.-M Cho, M Devlin, B Dober, C Groppi, et al. 2015. "Photon-noise limited sensitivity in titanium nitride kinetic inductance detectors." *Cit. Appl. Phys. Lett.* 106 (2015). doi:10.1063/1.4913418.

Jones, Glenn, Bradley R. Johnson, Heather McCarrick, Daniel Flanigan, Kristi Bradford, Amber Miller, Michele Limon, et al. 2015. "A cryogenic millimeter wavelength test facility." *26th Int. Symp. Sp. Terahertz Technol. ISSTT 2015:* 16–18. http://www.scopus.com/inward/record.url?eid=2-s2.0-84947292782%7B%5C&%7DpartnerID=tZOtx3y1.

Kaplan, S. B., C. C. Chi, D. N. Langenberg, J. J. Chang, S. Jafarey, and D. J. Scalapino. 1976. "Quasiparticle and phonon lifetimes in superconductors." *Phys. Rev. B* 14 (11): 4854–4873. doi:10.1103/PhysRevB.14.4209. arXiv: arXiv:1011.1669v3.

Kenyon, M., P. K. Day, C. M. Bradford, J. J. Bock, and H. G. Leduc. 2006. "Background-limited membrane-isolated TES bolometers for far-IR/submillimeter direct-detection spectroscopy." *Nucl. Instruments Methods Phys. Res. Sect. A Accel. Spectrometers, Detect. Assoc. Equip.* 559 (2): 456–458. doi:10.1016/j.nima.2005.12.036.

Kovács, Attila, Peter S. Barry, Charles M. Bradford, Goutam Chattopadhyay, Peter Day, Simon Doyle, Steve Hailey-Dunsheath, et al. 2012. "SuperSpec: design concept and circuit simulations." In *Proc. SPIE,* 84522G. doi:10.1117/12.927160. arXiv: 1211.0934.

Lamarre, Jean Michael, J. L. Puget, F. Bouchet, P. A.R. Ade, A. Benoit, J. P. Bernard, J. Bock, et al. 2003. "The Planck High Frequency Instrument, a third generation CMB experiment, and a full sky submillimeter survey." *New Astron. Rev.* 47 (11-12): 1017–1024. doi:10.1016/j.newar.2003.09.006. arXiv: 0308075 [astro-ph].

Leong, Yoke-Choy, and S. Weinreb. 1999. "Full band waveguide-to-microstrip probe transitions." *Microw. Symp. Dig. 1999 IEEE MTT-S Int.* 4:1435–1438. doi:10.1109/MWSYM.1999.780219.

Loeb, A., and R. Barkana. 2001. "The Reionization of the University by the First Stars and Quasars." *Annu. Rev. Astron. Astrophys.* 39:19–66.

Lowitz, A. E., E. M. Barrentine, S. R. Golwala, and P. T. Timbie. 2014. "A comparison of fundamental noise in kinetic inductance detectors and transition edge sensors for millimeter-wave applications." *J. Low Temp. Phys.* 176 (3-4): 504–510. doi:10.1007/s10909-014-1133-5. arXiv: 1402.3601.

Malin, C. 2012. *The Atacama Large Millimeter/submillimeter Array (ALMA) by night, under the Magellanic Clouds.* https://www.eso.org/public/images/ann12092a/.

Mani, Hamdi, and Philip Mauskopf. 2014. "A single-stage cryogenic LNA with low power consumption using a commercial SiGe HBT." In *11th Int. Work. Low Temp. Electron. Grenoble,* 17–20. doi:10.1109/WOLTE.2014.6881015.

Marquardt, E D, J P Le, and Ray Radebaugh. 2000. "Cryogenic Material Properties Database." In *11th Int. Cryocooler Conf.* 12:1–7. 6. doi:10.1016/0142-1123(90)90249-E.

Mattis, D. C., and J. Bardeen. 1958. "Theory of the anomalous skin effect in normal and superconducting metals." *Phys. Rev.* 111 (2): 412–417. doi:10.1103/PhysRev.111.412.

Mauskopf, P D. 2017. "Transition Edge Sensors and Kinetic Inductance Detectors in Astronomical Instruments." *Publ. Astron. Scoeity Pacific:* to appear in.

Mauskopf, P. D., S. Doyle, P. Barry, S. Rowe, A. Bidead, P. A R Ade, C. Tucker, et al. 2014. "Photon-noise limited performance in aluminum LEKIDs." *J. Low Temp. Phys.* 176 (3-4): 545–552. doi:10.1007/s10909-013-1069-1.

McCarrick, H, D Flanigan, G Jones, B R Johnson, P Ade, D Araujo, K Bradford, et al. 2014. "Horn-Coupled, Commercially-Fabricated Aluminum Lumped-Element Kinetic Inductance Detectors for Millimeter Wavelengths." *Rev. Sci. Instrum.* 85.

McCarrick, H., G. Jones, B. R. Johnson, M. H. Abitbol, P. A. R. Ade, S. Bryan, P. Day, et al. 2017. "Design and performance of dual-polarization lumped-element kinetic inductance detectors for millimeter-wave polarimetry": 1–11. arXiv: 1710.02239. http://arxiv.org/abs/1710.02239.

McCarrick, Heather, Maximilian H. Abitbol, Peter A. R. Ade, Peter Barry, Sean Bryan, George Che, Peter Day, et al. 2016. "Development of dual-polarization LEKIDs for CMB observations." In *Proc. SPIE,* 99140O. doi:10.1117/12.2231830. arXiv: 1607.03448.

McGeehan, R., P. S. Barry, E. Shirokoff, C. M. Bradford, S. Chapman, G. Che, J. Glenn, et al. 2017. "Noise Performance of SuperSpec: An on-chip, TiN KIP based mm-wave spectrometer." *J. Low Temp. Phys.* Submitted.

McKee, Christopher F., and Eve C. Ostriker. 2007. "Theory of Star Formation." *Annu. Rev. Astron. Astrophys.* 45:565–688. doi:10.1146/annurev.astro.45.051806.110602. arXiv: 0707.3514.

Melhuish, S. J., M. A. McCulloch, L. Piccirillo, and C. Stott. 2016. "A high-performance wave guide cryogenic thermal break." *Rev. Sci. Instrum.* 87 (10): –7. doi:10.1063/1.4964475.

Monfardini, A., A. Benoit, A. Bideaud, L. Swenson, A. Cruciani, P. Camus, C. Hoffmann, et al. 2011. "A DUAL-BAND MILLIMETER-WAVE KINETIC INDUCTANCE CAMERA FOR THE IRAM 30 m TELESCOPE." *Astrophys. J. Suppl. Ser.* 194, no. 2 (June): 24. doi:10.1088/0067-0049/194/2/24.

Monfardini, A., L. J. Swenson, A. Bideaud, F. X. Désert, S. J. C. Yates, A. Benoit, a. M. Baryshev, et al. 2010. "NIKA: A millimeter-wave kinetic inductance camera." *Astron. Astrophys.* 521 (October): A29. doi:10.1051/0004-6361/201014727.

Morata, Oscar, and Ted Huang. 2017. "ALMA's long look." *Nat. Astron.* 1 (6): 0156. doi:10.1038/s41550-017-0156.

Neill, C., A. Megrant, R. Barends, Yu Chen, B. Chiaro, J. Kelly, J. Y. Mutus, et al. 2013. "Fluctuations from edge defects in superconducting resonators." *Appl. Phys. Lett.* 103 (7): 1–5. doi:10.1063/1.4818710. arXiv: 1306.3718.

Netterfield, Calvin B., Peter A.R. Ade, James J. Bock, Edward L. Chapin, Mark J. Devlin, Matthew Griffin, Joshua O. Gundersen, et al. 2009. "Blast: The mass function, lifetimes, and properties of intermediate mass cores from a 50 deg2Submillimeter galactic survey in vela." *Astrophys. J.* 707 (2): 1824–1835. doi:10.1088/0004-637X/707/2/1824. arXiv: 0904.1207.

Niemack, M. D., P. A. R. Ade, J. Aguirre, F. Barrientos, J. A. Beall, J. R. Bond, J. Britton, et al. 2010. "ACTPol: A polarization-sensitive receiver for the Atacama Cosmology Telescope." In *Proc. SPIE.* doi:10.1117/12.857464. arXiv: 1006.5049.

Noroozian, Omid. 2012. "Superconducting microwave resonator arrays for submillimeter/far-infrared imaging." PhD Dissertation, California Institute of Technology. http://adsabs.harvard.edu/abs/2012PhDT.....26N.

Phillips, Thomas G, and Jocelyn Keene. 1992. "Submillimeter Astronomy." In *Proc. IEEE,* 80:1662–1678. 11.

Pippard, AB B. 1953. "An Experimental and Theoretical Study of the Relation between Magnetic Field and Current in a Superconductor." *Proc. R. Soc. London. Ser. A. Math. Phys. Sci.* 216 (1127): 547–568. doi:10.1098/rspa.1953.0040.

Posada, C. M., P. A.R. Ade, Z. Ahmed, K. Arnold, J. E. Austermann, A. N. Bender, L. E. Bleem, et al. 2015. "Fabrication of large dual-polarized multichroic TES bolometer arrays for CMB measurements with the SPT-3G camera." *Supercond. Sci. Technol.* 28 (9). doi:10.1088/0953-2048/28/9/094002.

Pospieszalski, Marian W. 2012. "Cryogenic Amplifier for Jansky Very Large Array Receivers." In *MIKON,* 7–10.

Samoska, L., M. Varonen, R. Reeves, K. Cleary, R. Gawande, P. Kangaslahti, T. Gaier, R. Lai, and S. Sarkozy. 2012. "W-Band cryogenic InP MMIC LNAs with noise below 30K." *IEEE MTT-S Int. Microw. Symp. Dig.* 30–32. doi:10.1109/MWSYM.2012.6258356.

Schlaerth, James, A. Vayonakis, P. Day, J. Glenn, J. Gao, S. Golwala, S. Kumar, et al. 2008. "A millimeter and submillimeter kinetic inductance detector camera." *J. Low Temp. Phys.* 151 (3-4 PART 2): 684–689. doi:10.1007/s10909-008-9728-3.

Sergeev, A V, and M Yu Reizer. 1996. "Photoresponse Mechanisms of Thin Superconducting Films and Superconducting Detectors." *Int. J. Mod. Phys. B* 10 (06): 635.

Shih, Yi-Chi, Thuy-Nhung Ton, and Long Q. Bui. 1988. "Waveguide-to-Microstrip Transitions for Millimeter-Wave Applications." *Microw. Symp. Dig. 1988 IEEE MTT-S Int.* 1988:473–475.

Shiu, Corwin. 2015. "Design considerations to improving sensitivity in SuperSpec : an onchip KID-based , mm-wave spectrometer Thesis by." Senior Thesis, California Institute of Technology.

Stacey, Gordon J, Steven Hailey-Dunsheath, Thomas Nikola, Thomas E Oberst, Stephen C Parshley, Dominic J Benford, Johanes G Staguhn, S Harvey Moseley, and Carole Tucker. 2007. "ZEUS : The Redshift (z) and Early Universe Spec-

trometer." In *From Z-Machines to ALMA (sub)millim. Spectrosc. Galaxies ASP Conf. Ser.* 52–61. doi:10.1117/12.552013.

Surdi, Harshad. 2016. "Applications of Kinetic Inductance: Parametric Amplifier & Phase Shifter, 2DEG Coupled Co-planar Structures & Microstrip to Slotline Transition at RF Frequencies." Master Thesis, Arizona State University.

Suzuki, T., P. Khosropanah, M. L. Ridder, R. A. Hijmering, J. R. Gao, H. Akamatsu, L. Gottardi, J. van der Kuur, and B. D. Jackson. 2016. "Development of Ultra-Low-Noise TES Bolometer Arrays." *J. Low Temp. Phys.* 184 (1-2): 52–59. doi:10.1007/s10909-015-1401-z.

Swenson, L. J., P. K. Day, B. H. Eom, H. G. Leduc, N. Llombart, C. M. McKenney, O. Noroozian, and J. Zmuidzinas. 2013. "Operation of a titanium nitride superconducting microresonator detector in the nonlinear regime." *J. Appl. Phys.* 113 (10). doi:10.1063/1.4794808. arXiv: 1305.4281.

Tang, Yulung, Niklas Wadefalk, Jacob W. Kooi, Joel Schleeh, Giuseppe Moschetti, Per Ake Nilsson, Arsalan Pourkabirian, Eunjung Cha, Silvia Tuzi, and Jan Grahn. 2017. "Cryogenic W-band LNA for ALMA band 2+3 with average noise temperature of 24 K." *IEEE MTT-S Int. Microw. Symp. Dig.* 176–179. doi:10.1109/MWSYM.2017.8058981.

Testi, Leonardo. 2009. "The atacama large millimeter/submillimeter array." *Astrophys. Sp. Sci. Proc.* 97 (202459): 289–294. doi:10.1007/978-1-4020-9190-2_48. arXiv: 0904.3739 [astro-ph.IM].

Tong, Z., C. Lundström, P. A. Andrekson, C. J. McKinstrie, M. Karlsson, D. J. Blessing, E. Tipsuwannakul, B. J. Puttnam, H. Toda, and L. Grüner-Nielsen. 2011. "Towards ultrasensitive optical links enabled by low-noise phase-sensitive amplifiers." *Nat. Photonics* 5 (7): 430–436. doi:10.1038/nphoton.2011.79.

Vissers, M. R., R. P. Erickson, H. S. Ku, Leila Vale, Xian Wu, G. C. Hilton, and D. P. Pappas. 2016. "Low-noise kinetic inductance traveling-wave amplifier using three-wave mixing." *Appl. Phys. Lett.* 108 (1). doi:10.1063/1.4937922. arXiv: 1509.09280.

Weinreb, S., J. Bardin, H. Mani, and G. Jones. 2009. "Matched wideband low-noise amplifiers for radio astronomy." *Rev. Sci. Instrum.* 80 (4). doi:10.1063/1.3103939.

Westig, M. P., S. Selig, K. Jacobs, T. M. Klapwijk, and C. E. Honingh. 2013. "Improved Nb SIS devices for heterodyne mixers between 700 GHz and 1.3 THz with NbTiN

transmission lines using a normal metal energy relaxation layer." *J. Appl. Phys.* 114 (12). doi:10.1063/1.4822167. arXiv: 1306.6797.

Wheeler, Caleb Henry. 2016. "Advancement of Heterodyne Focal Plane Arrays for Terahertz Astronomy." PhD Dissertation, Arizona State University.

Wheeler, J., S. Hailey-Dunsheath, E. Shirokoff, P. S. Barry, C. M. Bradford, S. Chapman, G. Che, et al. 2016. "SuperSpec: development towards a full-scale filter bank." In *Proc. SPIE,* vol. 9914, 99143K. doi:10.1117/12.2233798.

Wheeler, J., S. Hailey-Dunsheath, E. Shirokoff, P. Barry, C. M. Bradford, S. Chapman, G. Che, et al. 2017. "SuperSpec, The On-Chip Spectrometer: Improved NEP and Antenna Performance." *J. Low Temp. Phys.* Submitted.

Wilson, C. M., and D. E. Prober. 2003. "Quasiparticle number fluctuations in superconductors." *Phys. Rev. B* 69 (9): 35. doi:10.1103/PhysRevB.69.094524. arXiv: 0310525 [cond-mat].

Zaroubi, Saleem. 2012. "The Epoch of Reionization": 1–59. doi:10.1007/978-3-642-32362-1_2. arXiv: 1206.0267.

Žemlička, M., P. Neilinger, M. Trgala, M. Rehák, D. Manca, M. Grajcar, P. Szabó, et al. 2015. "Finite quasiparticle lifetime in disordered superconductors." *Phys. Rev. B - Condens. Matter Mater. Phys.* 92 (22): 1–7. doi:10.1103/PhysRevB.92.224506. arXiv: 1407.2402.

Zmuidzinas, Jonas. 2012. "Superconducting Microresonators: Physics and Applications." *Annu. Rev. Condens. Matter Phys.* 3 (1): 169–214. doi:10.1146/annurev-conmatphys-020911-125022.

APPENDIX A

MICROWAVE NETWORK MODEL FOR SUPERSPEC

Written in Python using its scikit-rf module, the following functions implement our lumped element microwave network model for SuperSpec filter banks. These functions assemble filter banks with different configurations by cascading their constituent spectral channels and interconnecting transmission lines, calculate the response of broadband channels, calculate instrument noise equivalent power (NEP) as a function of design parameters, and implement the hybrid simulation scheme that cascades full wave simulation results for individual channels.

```
import numpy as np
import skrf as rf
from matplotlib import pyplot as plt

# physical constants
c = 3.0e8 # speed of light in vacuum in m/s
h = 6.626e-34 # Planck's constant in Js
kB = 1.38e-23 # Boltzmann's constant in J/K

'''
Function to convert ABCD-matrix to S-matrix.

Arguments: A, B, C, D, Z0.
Returns: 2x2xf array S-matrix.

Notes: Transposition to fxnxn format is done externally.
'''
def ABCD2S(A,B,C,D, Z0):
    S11 = (1.0*A+B/Z0-C*Z0-D)/(A+B/Z0+C*Z0+D)
    S12 = 2.0*(A*D-B*C)/(A+B/Z0+C*Z0+D)
    S21 = 2.0/(A+B/Z0+C*Z0+D)
    S22 = (-1.0*A+B/Z0-C*Z0+D)/(A+B/Z0+C*Z0+D)
    return np.array([[S11, S12],[S21, S22]])


'''
Function to convert S-matrix to ABCD-matrix.

Arguments: S11, S12, S21, S22, Z0.
Returns: 2x2xf array ABCD-matrix.

Notes: Transposition for fxnxn format is done externally.
'''
def S2ABCD(S11, S12, S21, S22, Z0):
```

```
    A = ((1.0+S11)*(1.0-S22)+S12*S21)/(2.0*S21)
    B = Z0*((1.0+S11)*(1.0+S22)-S12*S21)/(2.0*S21)
    C = 1.0/Z0*((1.0-S11)*(1.0-S22)-S12*S21)/(2.0*S21)
    D = ((1.0-S11)*(1.0+S22)+S12*S21)/(2.0*S21)
    return np.array([[A,B],[C,D]])


'''
Function to convert 2-port S-matrix with arbitrary port
impedances Z01 and Z02 to Z-matrix.

Arguments: S (fx2x2 S-matrix), Z01 (fx1 Z0 vector),
Z02 (fx1 Z0 vector)
Returns: Z (fx2x2 Z-matrix)
'''
def S2Z(S, Z01, Z02):
    S11=S[:,0,0]; S12=S[:,0,1]; S21=S[:,1,0]; S22=S[:,1,1]
    Z11=((np.conj(Z01)+S11*Z01)*(1.0-S22)+S12*S21*Z01) \
        /((1.0-S11)*(1.0-S22)-S12*S21)
    Z12=2.0*S12*np.sqrt(np.real(Z01)*np.real(Z02)) \
        /((1.0-S11)*(1.0-S22)-S12*S21)
    Z21=2.0*S21*np.sqrt(np.real(Z01)*np.real(Z02)) \
        /((1.0-S11)*(1.0-S22)-S12*S21)
    Z22=((1.0-S11)*(np.conj(Z02)+S22*Z02)+S12*S21*Z02) \
        /((1.0-S11)*(1.0-S22)-S12*S21)
    Z=np.array([[Z11, Z12], [Z21, Z22]]).transpose(2, 0, 1)
    return Z


'''
Function to convert 2-port Z-matrix to S-matrix with arbitrary
port impedances Z01 and Z02.

Arguments: Z (fx2x2 S-matrix), Z01 (fx1 Z0 vector),
Z02 (fx1 Z0 vector)
Returns S (fx2x2 S-matrix)
'''
def Z2S(Z, Z01, Z02):
    Z11=Z[:,0,0]; Z12=Z[:,0,1]; Z21=Z[:,1,0]; Z22=Z[:,1,1]
    S11=((Z11-np.conj(Z01))*(Z22+Z02)-Z12*Z21)/((Z11+Z01) \
        *(Z22+Z02)-Z12*Z21)
    S12=2.0*Z12*np.sqrt(np.real(Z01)*np.real(Z02)) \
```

```
        /((Z11+Z01)*(Z22+Z02)-Z12*Z21)
    S21=2.0*Z21*np.sqrt(np.real(Z01)*np.real(Z02)) \
        /((Z11+Z01)*(Z22+Z02)-Z12*Z21)
    S22=((Z11+np.conj(Z01))*(Z22-np.conj(Z02)) \
        -Z12*Z21)/((Z11+Z01)*(Z22+Z02)-Z12*Z21)
    S=np.array([[S11, S12],[S21, S22]]).transpose(2, 0, 1)
    return S


'''
Function to create a network object representing a lossy
transmission line.

Arguments: frequency band, physical length, char. impedance,
propagation speed, relative permittivity of dielectric,
loss tangent of dielectric, # of ports.
Returns: transmission line network object
Note: we assume that loss is dominated by dielectric loss
'''
def TransmissionLineLossy(Band, l, Z0, v, epsr=11.7, \
        lossTan=0.0, nPorts=2):

    beta = 2.0*np.pi*Band.f/v # real propagation constant
    alpha = np.pi*Band.f/v*lossTan
    gamma = alpha + 1j*beta # complex propagation constant

    # construct ABCD matrix of the lossy line
    A = np.cosh(gamma*l)
    B = Z0*np.sinh(gamma*l)
    C = 1/Z0*np.sinh(gamma*l)
    D = np.cosh(gamma*l)

    # convert lossy line ABCD to S-parameters
    S_2port = ABCD2S(A, B, C, D, Z0)
    S11=S_2port[0,0]; S12=S_2port[0,1]; S21=S_2port[1,0]
    S22=S_2port[1, 1];

    if nPorts==2:
        S_2port = np.array([[S11, S12],[S21, \
                S22]]).transpose(2, 0, 1)
        return rf.Network(frequency=Band, s=S_2port, z0=Z0)
    elif nPorts==3:
```

```
        S13 = np.sqrt(1-np.conj(S11)*S11-np.conj(S12)*S12)
        S31 = S13
        theta23 = np.pi/2-beta*l
        S23 = np.abs(S13)*np.exp(1j*theta23)
        S32 = S23
        S33 = np.zeros(np.size(Band.f))
        S_3port = np.array([[S11, S12, S13],[S21, S22, \
                S23], [S31, S32, S33]]).transpose(2, 0, 1)
        return rf.Network(frequency = Band, s = S_3port, \
                z0 = Z0)


'''
Function to create a network object representing a spectral
channel as either a 2-port or 3-port network. Incorporates
lossy dielectric as Qloss.

Arguments: freq. band, char. impedance, resonant freq.,
coupling Q, internal Q, loss Q, approach ("1" for 3-port
representation all referenced to Z0 and terminated in ZL,
"2" for 3-port representation with port 2 referenced to ZL,
"3" for 2-port representation).
Returns: spectral channel network object
'''
def SpectralChannelLossy(Band, Z0, fres, Qc, Qdet, Qloss, \
        approach=1):

    x = (Band.f-fres)/fres

    # shunt impedance of the entire resonator
    ZL = Z0/2*Qc*(1/Qdet+1/Qloss)+1j*Z0*Qc*x

    # 3-port network with all ports referenced to 50 Ohm;
    # terminate port 2 with ZL
    if approach==1:
        S_3port = np.ones((np.size(x), 3, 3))

        # create 3-port S-matrix for the 50 Ohm matched
        # network
        S_3port[:,0, 0]=-1.0/3; S_3port[:,0, 1]=2.0/3
        S_3port[:,0, 2]=2.0/3
        S_3port[:,1, 0]=2.0/3; S_3port[:,1, 1]=-1.0/3
```

```
        S_3port[:,1, 2]=2.0/3
        S_3port[:,2, 0]=2.0/3; S_3port[:,2, 1]=2.0/3
        S_3port[:,2, 2]=-1.0/3

        # create a network object for the 50 Ohm matched
        # network
        MatchedNtwk = rf.Network(frequency = Band, \
                s = S_3port, z0 = Z0)

        # create 1-port S-matrix for the resonator load
        S11_L=(ZL-Z0)/(ZL+Z0)
        Resonator = rf.Network(frequency = Band, \
                s = S11_L, z0 = Z0)
        Ntwk = rf.connect(MatchedNtwk, 2, Resonator, 0)
        return Ntwk

    # 3-port network with all ports referenced to 50 Ohm;
    # renormalize so port 2 is referenced to ZL
    elif approach==2:
        S_3port = np.ones((np.size(x), 3, 3))

        # create 3-port S-matrix for the 50 Ohm matched
        # network
        S_3port[:,0, 0]=-1.0/3; S_3port[:,0, 1]=2.0/3
        S_3port[:,0, 2]=2.0/3
        S_3port[:,1, 0]=2.0/3; S_3port[:,1, 1]=-1.0/3
        S_3port[:,1, 2]=2.0/3
        S_3port[:,2, 0]=2.0/3; S_3port[:,2, 1]=2.0/3
        S_3port[:,2, 2]=-1.0/3

        # create a network object for the 50 Ohm matched
        # network
        Ntwk = rf.Network(frequency = Band, s = S_3port, \
                z0 = Z0)

        # create port reference impedance matrix
        Zmatrix = np.empty([len(Band.f),3], dtype=complex)
        Zmatrix[:,2]=Z0; Zmatrix[:,0]=Z0; Zmatrix[:,1]=ZL

        Ntwk.renormalize(Zmatrix, powerwave=True)
        return Ntwk
```

```
    elif approach==3:
        # create 2-port S-matrix for the network
        S11=-Z0/(2*ZL+Z0); S22=S11; S12=2*ZL/(2*ZL+Z0)
        S21=S12
        S_2port=np.array([[S11, S12],[S21, \
                S22]]).transpose(2, 0, 1)

        return rf.Network(frequency = Band, s = S_2port, \
        z0=Z0)


'''
Function to create an unterminated network object for a
filter bank with an arbitrary # of channels taking into
account possible dielectric loss and optionally plot the
reflected power, thru power, and power absorbed by each
channel. User input determines whether or not to plot, plot
title, start/stop frequency, whether or not to save, and file
name.

Arguments: freq. band, design data for all channels, char.
impedance, propagation speed on feedline, physical
separation between channels (in wavelengths), transmission
line attenuation, spectral channel approach, to plot or not
to plot.
Returns: filter bank network object

Notes: Physical separation refers to the wavelength
corresponding to the resonant frequency of left channel
in each pair of channels.
'''
def FilterBankLossy(Band, Data, Z0=50.0, v=c, physSep=0.25, \
        epsr=11.7, lossTan=0.0, approach=3, doPlot=False):

    # initialize current network to the first spectral
    # channel
    CurrentNtwk = SpectralChannelLossy(Band, Z0, Data[0,0], \
        Data[1,0], Data[2,0], Data[3,0], approach)

    # loop to create filter bank with arbitrary # of \
    # channels and create network
    for i in np.arange(np.shape(Data)[1]):
```

```
    if i < np.shape(Data)[1]-1:
        # resonant frequencies and quality factors for
        # current and next SCs
        fres_current = Data[0,i]
        fres_nxt = Data[0,i+1]; Qc_nxt = Data[1,i+1];
        Qdet_nxt = Data[2,i+1]; Qloss_nxt = Data[3,i+1]

        # create Network object for next SC
        NextSC = SpectralChannelLossy(Band, Z0, \
            fres_nxt, Qc_nxt, Qdet_nxt, Qloss_nxt, \
                approach)

        # create interconnecting transmission line
        lambda_current = v/fres_current
        # lambda_nxt = v/fres_nxt
        lineLength = physSep*lambda_current
        # lineLength = physSep*(lambda_current+ \
            lambda_nxt)/2.0
        TLine = TransmissionLineLossy(Band, \
            lineLength, Z0, v, epsr, lossTan)

        # connect current network to the transmission
        # line
        N = CurrentNtwk.nports
        InterNtwk = rf.connect(CurrentNtwk, N-1, \
            TLine, 0)

        # connect current network to the next SC
        N = InterNtwk.nports
        CurrentNtwk = rf.connect(InterNtwk, N-1, \
            NextSC, 0)

# code to do plotting if doPlot is True
if doPlot:
    # full filter bank S-Matrix with correct
    # port ordering
    nPorts = CurrentNtwk.number_of_ports

    # plots for arbitrary number of channels
    plt.figure(1); plt.clf()
    plt.rc('legend', fontsize = 12)
```

```
plt.plot(Band.f/1.0e9, \
        np.conj(CurrentNtwk.s[:,nPorts-1,0]) \
    *CurrentNtwk.s[:,nPorts-1,0], \
    linewidth = '2', label = 'Thru')

plt.plot(Band.f/1.0e9, \
        np.conj(CurrentNtwk.s[:,0,0]) \
        *CurrentNtwk.s[:,0,0], linewidth = '2', \
    label = 'Reflected')

# plot absorbed powers if using 3-port approach for
# spectral channels
if approach == 2:
    # if there are 5 or less channels, each channel
    # is different color
    if np.shape(Data)[1] <= 5:
        for i in xrange(1, nPorts-1):
            plt.plot(Band.f/1.0e9, \
                        np.conj(CurrentNtwk.s[:,i,0]) \
                        *CurrentNtwk.s[:,i,0], \
                '--', linewidth = '2', \
                label = 'Ch ' + str(i-1))

        plt.plot(Band.f/1.0e9, \
                np.conj(CurrentNtwk.s[:,nPorts- \
                1,0])*CurrentNtwk.s[:,nPorts-1,0], \
                '--', linewidth = '2', \
                label = 'Ch ' + str(nPorts-2))

    # otherwise plot all channels in black with no
    # legend entries
    else:
        for i in xrange(1, nPorts-1):
            # PowerS[:,i]=CurrentNtwk.s[:,i-1,0] \
                plt.plot(Band.f/1.0e9, \
                np.conj(CurrentNtwk.s[:,i,0]) \
                *CurrentNtwk.s[:,i,0], 'k:', \
                linewidth = '3')

        #PowerS[:,nPorts-1] \
                = CurrentNtwk.s[:,nPorts-1,0] \
                plt.plot(Band.f/1.0e9, \
```

```
                        np.conj(CurrentNtwk.s[:,nPorts-1,0]) \
                        *CurrentNtwk.s[:,nPorts-1,0], 'k:', \
                        linewidth = '3')

        # prompt user to enter plot title and start/stop
        # frequencies
        plotTitle = raw_input('What would you like to title \
        your plot? ')
        start = raw_input('Start frequency (GHz): ')
        stop = raw_input('Stop frequency (GHz): ')

        plt.title(plotTitle)
        plt.legend(loc='best')
        plt.xlabel('Frequency (GHz)')
        plt.ylabel('Power')
        plt.xlim(float(start), float(stop))
        plt.ylim(0, 1)
        plt.ion()
        plt.show()

        # prompt user about whether or not to save plot
        while True:
            isSave = raw_input('Would you like to save the \
            plot? Y or N ')
            if isSave in ('y', 'n', 'Y', 'N'):
                break
            else:
                print """You must enter 'Y' or 'N'! """

        # if yes, prompt for file name and save as .png file
        if isSave in ('y', 'Y'):
            plotFileName = raw_input('What name would you \
            like to save your plot as? ')
            plt.savefig('PythonPlots/' + plotFileName \
                + '.png')
    return CurrentNtwk


'''
Function to create a network object for a filter bank
terminated in an arbitrary load. Also connects length of
transmission line between the final channel and termination.
```

```
Arguments: same as for FilterBank + length of line preceding
filter bank, length of line after filter bank, impedance of
termination

Returns: terminated filter bank network object
'''
def TerminatedFilterBank(Band, Data, lBack, ZT, Z0=50.0, \
        n=1.0, physSep=0.25, approachFB=3, approachT=1):

    UnterminatedFB = FilterBank(Band, Data, Z0, n, physSep, \
        approachFB)

    # transmission line between final channel and termination
    TLine = TransmissionLine(Band, lBack, Z0, n)

    # convert Z-matrix to S-matrix with port 2 referenced to
    # termination impedance resulting in a 2-port Ntwk; used
    # for computing response of BB detector after the spectral
    # channels; only works if SC is represented by 2-port
    # network
    if approachT==1:
        # 2-port network with FB connected to end
        # transmission line
        InterNtwk = rf.connect(UnterminatedFB, 1, TLine, 0)

        # InterNtwk port 1 ref. impedance
        Z01=Z0*np.ones(Band.npoints)

        # InterNtwk port 2 ref. impedance
        Z02=ZT*np.ones(Band.npoints)
        Z0Matrix=np.vstack((Z01, Z02)).transpose(1,0)
        TermS=Z2S(InterNtwk.z, Z01, Z02)
        Ntwk=rf.Network(frequency=Band, s=TermS, z0=Z0Matrix)

    # create 1-port network for termination and connect to
    # unterminated FB resulting in a 1-port Ntwk
    elif approachT==2:
        # create 1-port S-matrix for the termination
        S11_T=(ZT*np.ones(Band.npoints)- \
                Z0)/(ZT*np.ones(Band.npoints)+Z0)
```

```
        Term=rf.Network(frequency=Band, s=S11_T, z0=Z0)

        # 3-port representation of spectral channels
        if approachFB==2:
            InterNtwk = rf.connect(UnterminatedFB, \
                UnterminatedFB.nports-1, TLine, 0)
            # terminate filter bank
            Ntwk = rf.connect(InterNtwk, \
                InterNtwk.nports-1, Term, 0)

        # 2-port representation of spectral channels
        elif approachFB==3:
            InterNtwk = rf.connect(UnterminatedFB, 1, TLine, 0)
            # terminate filter bank
            Ntwk = rf.connect(InterNtwk, 1, Term, 0)

    return Ntwk


'''
Function to create a network object for a filter bank
terminated in an arbitrary load taking in account possible
dielectric loss. Also connects length of transmission line
between the final channel and termination.

Arguments: same as for FilterBankLossy + length of line after
filter bank, impedance of termination

Returns: terminated filter bank network object
'''
def TerminatedFilterBankLossy(Band, Data, lBack, ZT, \
        Z0=50.0, v=c, physSep=0.25, epsr=11.7, lossTan=0.0, \
    approachFB=3, approachT=1):

    UnterminatedFB = FilterBankLossy(Band, Data, Z0, v, \
        physSep, epsr, lossTan, approachFB)

    # transmission line between final channel and termination
    TLine = TransmissionLineLossy(Band, lBack, Z0, v, epsr, \
        lossTan)

    # convert Z-matrix to S-matrix with port 2 referenced to
```

```
# termination impedance resulting in a 2-port Ntwk; used
# for computing response of BB detector after the spectral
# channels; only works if SC is represented by 2-port
# network
if approachT==1:
    # 2-port network with FB connected to end
    # transmission line

    InterNtwk = rf.connect(UnterminatedFB, 1, TLine, 0)

    # InterNtwk port 1 ref. impedance
    Z01=Z0*np.ones(Band.npoints)

     # InterNtwk port 2 ref. impedance
    Z02=ZT*np.ones(Band.npoints)
    Z0Matrix=np.vstack((Z01, Z02)).transpose(1,0)
    TermS=Z2S(InterNtwk.z, Z01, Z02)
    Ntwk=rf.Network(frequency=Band, s=TermS, z0=Z0Matrix)

# create 1-port network for termination and connect to
# unterminated FB resulting in a 1-port Ntwk
elif approachT==2:
    # create 1-port S-matrix for the termination
    S11_T=(ZT*np.ones(Band.npoints)-Z0) \
            /(ZT*np.ones(Band.npoints)+Z0)
    Term=rf.Network(frequency=Band, s=S11_T, z0=Z0)

    # 3-port representation of spectral channels
    if approachFB==2:
        InterNtwk = rf.connect(UnterminatedFB, \
            UnterminatedFB.nports-1, TLine, 0)
        # terminate filter bank
        Ntwk = rf.connect(InterNtwk, InterNtwk.nports-1, \
            Term, 0)

    # 2-port representation of spectral channels
    elif approachFB==3:
        InterNtwk = rf.connect(UnterminatedFB, 1, TLine, 0)
        # terminate filter bank
        Ntwk = rf.connect(InterNtwk, 1, Term, 0)

return Ntwk
```

```
'''
Function to create a network object for a filter bank
terminated in an arbitrary load taking in account possible
dielectric loss. Also connects length of transmission line
between the final channel and termination. Used to calculate
response of BB1, a broadband absorber placed before the
spectral channels.

Arguments: same as for FilterBankLossy + length of line
after filter bank, impedance of termination

Returns: terminated filter bank network object
'''
def TerminatedFBLossyEnd(Band, Data, lBack, ZT, Z0=50.0, \
        v=c, physSep=0.25, epsr=11.7, lossTan=0.0, \
    approachFB=3, approachT=1):

    UnterminatedFB = FilterBankLossy(Band, Data, Z0, v, \
        physSep, epsr, lossTan, approachFB)

    # transmission line between final channel and termination
    TLine = TransmissionLineLossy(Band, lBack, Z0, v, epsr, \
        lossTan)

    # convert Z-matrix to S-matrix with port 2 referenced to
    # termination impedance resulting in a 2-port Ntwk; used
    # for computing response of BB detector after the
    # spectral channels; only works if SC is represented by
    # 2-port network
    if approachT==1:
        # 2-port network with FB connected to end
        # transmission line

        InterNtwk = rf.connect(UnterminatedFB, 1, TLine, 0)

        # InterNtwk port 1 ref. impedance
        Z01=Z0*np.ones(Band.npoints)
        # InterNtwk port 2 ref. impedance
        Z02=ZT*np.ones(Band.npoints)
```

```
        Z0Matrix=np.vstack((Z01, Z02)).transpose(1,0)
        TermS=Z2S(InterNtwk.z, Z01, Z02)
        Ntwk=rf.Network(frequency=Band, s=TermS, z0=Z0Matrix)

    # create 1-port network for termination and connect to
    # unterminated FB resulting in a 1-port Ntwk
    elif approachT==2:
        # create 1-port S-matrix for the termination
        S11_T=(ZT*np.ones(Band.npoints)-Z0) \
                /(ZT*np.ones(Band.npoints)+Z0)
        Term=rf.Network(frequency=Band, s=S11_T, z0=Z0)

        # 3-port representation of spectral channels
        if approachFB==2:
            InterNtwk = rf.connect(UnterminatedFB, \
                UnterminatedFB.nports-1, TLine, 0)

            # terminate filter bank
            Ntwk = rf.connect(InterNtwk, \
                InterNtwk.nports-1, Term, 0)

        # 2-port representation of spectral channels
        elif approachFB==3:
            InterNtwk = rf.connect(UnterminatedFB, 1, TLine, 0)
            # terminate filter bank
            Ntwk = rf.connect(InterNtwk, 1, Term, 0)

    # same as approachT = 1, but using renormalize function
    # instead of converting between S and Z parameters
    elif approachT==3:
        Ntwk = rf.connect(UnterminatedFB, \
                nterminatedFB.nports-1, TLine, 0)

        NewPortZ = np.empty([Band.npoints, Ntwk.nports], \
                dtype=complex)
        NewPortZ[:,Ntwk.nports-1]=ZT
        for i in xrange(0, Ntwk.nports-1):
            NewPortZ[:,i] = Ntwk.z0[:,i]
        Ntwk.renormalize(NewPortZ)
    return Ntwk
```

```
'''
Function to create a network object for a filter bank
preceded by an antenna with arbitrary impedance taking into
account possible dielectric loss. Also connects length of
transmission line between the antenna and first channel.
Used to calculate response of BB2, a broadband absorber
placed after the spectral channels.

Arguments: same as for FilterBankLossy + length of line
preceding filter bank, impedance of antenna

Returns: terminated filter bank network object
'''
def TerminatedFBLossyBegin(Band, Data, lFront, ZA, \
        Z0=50.0, v=c, physSep=0.25, epsr=11.7, lossTan=0.0, \
    approachFB=3, approachT=1):

    UnterminatedFB = FilterBankLossy(Band, Data, Z0, v, \
        physSep, epsr, lossTan, approachFB)

    # transmission line between antenna and first channel
    TLine = TransmissionLineLossy(Band, lFront, Z0, v, \
        epsr, lossTan)

    # convert Z-matrix to S-matrix with port 2 referenced
    # to termination impedance resulting in a 2-port Ntwk;
    # used for computing response of BB detector after the
    # spectral channels; only works if SC is represented
    # by 2-port network
    if approachT==1:
        # 2-port network with FB connected to end
        # transmission line

        InterNtwk = rf.connect(TLine, 1, UnterminatedFB, 0)
        # InterNtwk port 1 ref. impedance
        Z01=ZA*np.ones(Band.npoints)
        # InterNtwk port 2 ref. impedance
        Z02=Z0*np.ones(Band.npoints)

        Z0Matrix=np.vstack((Z01, Z02)).transpose(1,0)
        TermS=Z2S(InterNtwk.z, Z01, Z02)
        Ntwk=rf.Network(frequency=Band, s=TermS, z0=Z0Matrix)
```

```
    # same as approachT = 1, but using renormalize instead
    # of converting between S and Z parameters. If using
    # 3-port SC representation, the through S-parameter is
    # S[nports-1,0]

    elif approachT==2:
        # for 2-port and 3-port representations of spectral
        # channels
        Ntwk = rf.connect(TLine, 1, UnterminatedFB, 0)
        NewPortZ = np.empty([Band.npoints, Ntwk.nports], \
                dtype=complex)
        NewPortZ[:,0]=ZA
        for i in xrange(1, Ntwk.nports):
            NewPortZ[:,i] = Ntwk.z0[:,i]
        Ntwk.renormalize(NewPortZ)
    return Ntwk


'''
Function to create a network object for a filter bank
preceded by an antenna with arbitrary impedance AND
terminated in an arbitrary load taking into account
possible dielectric loss. Lengths of transmission line
connect antenna to first channel and final channel to
termination. Used to calculate response of each spectral
channel under realistic input and output port termination
conditions.

Arguments: same as for FilterBankLossy + length of line
preceding filter bank, impedance of antenna, length of line
following filter bank, impedance of termination

Returns: terminated filter bank network object
'''
def TerminatedFBLossyBoth(Band, Data, lFront, lBack, ZA, \
        ZT, Z0=50.0, v=c, physSep=0.25, epsr=11.7, lossTan=0.0, \
    approachFB=3, approachT=1):

    UnterminatedFB = FilterBankLossy(Band, Data, Z0, v, \
        physSep, epsr, lossTan, approachFB)
```

```
# transmission line between antenna and first channel
TLineBegin = TransmissionLineLossy(Band, lFront, Z0, \
    v, epsr, lossTan)
# transmission line between final channel and termination
TLineEnd = TransmissionLineLossy(Band, lBack, Z0, v, \
    epsr, lossTan)

# convert Z-matrix to S-matrix with port 2 referenced
# to termination impedance resulting in a 2-port Ntwk;
# only works if SC is represented by 2-port network
if approachT==1:
    # 2-port network with FB connected to end
    # transmission line
    InterNtwk1 = rf.connect(TLineBegin, 1, \
            UnterminatedFB, 0)
    InterNtwk2 = rf.connect(InterNtwk1, 1, TLineEnd, 0)

    # InterNtwk port 1 ref. impedance
    Z01=ZA*np.ones(Band.npoints)
    # InterNtwk port 2 ref. impedance
    Z02=ZT*np.ones(Band.npoints)
    Z0Matrix=np.vstack((Z01, Z02)).transpose(1,0)
    TermS=Z2S(InterNtwk2.z, Z01, Z02)
    Ntwk=rf.Network(frequency=Band, s=TermS, z0=Z0Matrix)

# same as approachT = 1, but using renormalize instead
# of converting between S and Z parameters. If using
# 3-port SC representation, the through S-parameter is
# S[nports-1,0]
elif approachT==2:
    # for 2-port and 3-port representations of spectral
    # channels
    InterNtwk = rf.connect(TLineBegin, 1, \
            UnterminatedFB, 0)
    Ntwk = rf.connect(InterNtwk, InterNtwk.nports-1, \
            TLineEnd, 0)

    NewPortZ = np.empty([Band.npoints, Ntwk.nports], \
            dtype=complex)
    NewPortZ[:,0]=ZA
    NewPortZ[:,Ntwk.nports-1]=ZT
    for i in xrange(1, Ntwk.nports-1):
```

```
            NewPortZ[:,i] = Ntwk.z0[:,i]
        Ntwk.renormalize(NewPortZ)
    return Ntwk


'''
Function to calculate response of BB1, a broadband absorber
placed inline with the transmission line in front of a
terminated filter bank.

Arguments: coupling constant of BB1, frequency band,
transmission line length, coupling length, center position,
characteristic impedance of transmission line, antenna
impedance, propagation speed on transmission line,
dielectric constant, loss tangent of dielectric layer,
reflection coefficient at input of terminated filter bank
(assuming matched impedance), approach (1 normalizes
response to V at antenna, 2 normalizes response to V after
antenna)

Returns: an array of BB1 response at each frequency point
in the band
'''
def BroadbandChannelBefore(epsilon1, Band, lLine, \
lCoupling, zc, Z0, ZA, v, epsr, lossTan, GammaFB, \
approach=1):
    beta = 2.0*np.pi*Band.f/v # real propogation constant
    # attenuation constant in Np/m
    alpha = np.pi*np.sqrt(epsr)*Band.f/v*lossTan
    gamma = alpha + 1j*beta # complex propagation constant

    # input impedance immediately after antenna looking
    # toward termination
    Zin = Z0*(1.0+GammaFB*np.exp(-2.0*gamma*lLine)) \
        /(1.0-GammaFB*np.exp(-2.0*gamma*lLine))

    # incident voltage at end of transmission line
    V0plus = Zin/((ZA+Zin)*(np.exp(gamma*lLine) \
        +GammaFB*np.exp(-gamma*lLine)))

    # power coupled to BB1 normalized to power immediately
    # after antenna
```

```
    BB1 = epsilon1*(np.sinc(1j*alpha*lCoupling) \
        *np.exp(-2*alpha*zc) + 2.0*np.abs(GammaFB) \
        *np.cos(2.0*beta*zc+np.angle(GammaFB)) \
        *np.sinc(beta*lCoupling) \
        + np.conj(GammaFB)*GammaFB \
        *np.sinc(1j*alpha*lCoupling) \
        *np.exp(2.0*alpha*zc))

    # unity is Voc at antenna
    if approach==1:
        return np.conj(V0plus)*V0plus*BB1
    # unity is at end of transmission line, immediately
    # before the first channel
    elif approach==2:
        return BB1


'''
Function to calculate response of BB2, a broadband absorber
placed inline with the transmission line behind of a
terminated filter bank.

Arguments: coupling constant of BB2, frequency band,
coupling length, center position, propagation speed on
transmission line, dielectric constant, loss tangent of
dielectric layer, transmission coefficient (S21) at
termination of filter bank (filter bank object used must
contain end transmission line with load port referenced to
termination impedance)

Returns: an array of BB2 response at each frequency point
in the band
'''
def BroadbandChannelAfter(epsilon2, Band, lCoupling, zc, \
v, epsr, lossTan, TFB):
        # attenuation constant in Np/m
    alpha = np.pi*np.sqrt(epsr)*Band.f/v*lossTan

    # calculate response of BB2
    BB2 = epsilon2*np.conj(TFB)*TFB \
        *np.sinc(1j*alpha*lCoupling) \
        *np.exp(-2.0*alpha*zc)
```

```
    return BB2

'''
Function to calculate the response of individual channels
of arbitrary filter bank using the "adjacent subtraction
method."
'''
def ChannelResponse(Band, Data, lback, ZT, Z0=50.0, \
        n=1.0, physSep = 0.25, approachFB=3, approachT=1):
    v = c/n # wavespeed
    # create nChannels x f array to store the response of
    # all channels
    Response = np.empty([np.shape(Data)[1], Band.npoints], \
        dtype=complex)

    # array to store aggregate response of channels up
    # to current-1
    PreviousResponse = np.zeros(Band.npoints, \
        dtype = complex)
    for i in xrange(np.shape(Data)[1]):
        # data for FB up to and including channel i and
        # line after channel i
        DataBefore = Data[:, 0:i+1]

        if i<np.shape(Data)[1]-1:
            # create transmission line after channel i
            lineLength = physSep*v/DataBefore[0, i]
            TLine = TransmissionLine(Band, lineLength, Z0, n)
            # FB up to and including channel i and line
            # after channel i
            FBBefore = rf.connect(FilterBank(Band, \
                DataBefore, Z0, n, physSep, approachFB), \
                1, TLine, 0)

            # create FB of the remaining channels
            DataAfter = Data[:, i+1:np.shape(Data)[1]]
            FBAfter = TerminatedFilterBank(Band, \
                DataAfter, lback, ZT, Z0, n, physSep, \
                approachFB)

            # input impedance looking toward load at port 1
            # of FBAfter
```

```
            ZinAfter = Z0*(1.0+FBAfter.s[:,0,0]) \
                /(1.0-FBAfter.s[:,0,0])
        else:
            # transmission line after final channel before \
            # termination
            TLine = TransmissionLine(Band, lback, Z0, n)
            FBBefore = rf.connect(FilterBank(Band, \
                DataBefore, Z0, n, physSep, approachFB), \
                1, TLine, 0)
            ZinAfter = ZT*np.ones(Band.npoints)

        # port reference impedances for FBBefore
        Z01 = Z0*np.ones(Band.npoints)
        Z02 = ZinAfter

        # convert to S-parameters with port 2 referenced
        # to ZinAfter
        S11 = Z2S(FBBefore.z, Z01, Z02)[:,0,0]
        S21 = Z2S(FBBefore.z, Z01, Z02)[:,1,0]

        # aggregate response of channels up to and
        # including channel i
        CurrentResponse = 1.0-np.conj(S11)*S11- \
                np.conj(S21)*S21

        # calculate channel i response and store in Response
        CurChannelResponse = CurrentResponse-PreviousResponse
        Response[i,:]=CurChannelResponse

        PreviousResponse = CurrentResponse

    return Response


'''
Function to calculate the channel center frequencies of a
band.

Arguments: lowest frequency, highest frequency, spectral
resolution, oversampling ratio
Returns: # of channels, array of channel frequencies
'''
```

```
def ChannelFrequencies(fl, fu, R, Sigma):
        # number of channels, rounded down
    Nc = np.int(np.floor(Sigma*R*np.log(fu/fl)))

    # frequency scaling of channels
    x = np.exp(-(np.log(fu)-np.log(fl))/(Nc-1))
    # array to hold all the spectral channel frequencies
    Channels = np.ones(Nc)
    Channels[0] = fu # initialize the first channel
    for i in xrange(1, Nc):
        Channels[i]=x*Channels[i-1]
    return Nc, Channels


'''
Function to calculate S11 and S21 of an isolated channel.

Arguments: freq. band, coupling Q, internal Q
Returns: S11, S21 as a tuple.
'''
def IsolatedChannel(Band, fres, Qc, Qi):
    Qr = 1.0/(1.0/Qi+1.0/Qc)
    x = (Band.f-fres)/fres
    S21 = 1.0-(Qr/Qc)/(1.0+2.0j*Qr*x)
    S11 = S21-1.0
    return np.array([S11, S21])


'''
Function to calculate filter bank sensitivity assuming
matched antenna and termination

Arguments: frequency band, characteristic impedance of
transmission line, propagation speed on transmission line,
physical separation between channels, dielectric constant,
coupling quality factor, internal quality factor, loss
quality factor, detector NEP, and oversampling factor

Returns: the tuple (NEPsysmean, NEPsys, Qch, Nch)
'''
def FilterBankSensitivity(Band, Z0, v, physSep, epsr, \
        Qfeed, Qdet, Qloss, NEPdet = 0.0, oversampling=1.0, \
```

```
emissivity=0.1, Tsky=260, etaSys=0.5):

# channel quality factor and spectral resolving power
Qch = 1.0/(1.0/Qfeed + 1.0/Qdet + 1.0/Qloss)

# data for filter bank
Channels = ChannelFrequencies(Band.start, Band.stop, \
    Qch, oversampling)
Nch = Channels[0]
ResonantFrequency = Channels[1]
CouplingQ = Qfeed*np.ones(Nch)
InternalQ = Qdet*np.ones(Nch)
LossQ = Qloss*np.ones(Nch)
Data = np.vstack((ResonantFrequency, CouplingQ, \
    InternalQ, LossQ))

# filter bank network object
FB = FilterBankLossy(Band, Data, Z0, v, physSep, \
    epsr, 1.0/Qloss, 2)

# fraction of power coupled to resonator that is
# actually detected
detFactor = (1.0/Qdet)/(1.0/Qdet+1.0/Qloss)

# occupation number in source
n0 = 1.0/(np.exp(h*Band.f/(kB*Tsky))-1.0)

# recombination coefficient
kRecomb = 1.0

NEPSys = np.empty((Band.npoints,FB.nports-2))

for i in xrange(1, FB.nports-1):
    # occupation number in detector
    n = n0*emissivity*etaSys*detFactor
    *np.conj(FB.s[:,i,0])*FB.s[:,i,0]

    # shot noise NEP
    NEPshot = np.sqrt(np.sum(2.0*(h*Band.f)**2 \
            *n*Band.step))
    # wave noise NEP
    NEPwave = np.sqrt(np.sum(2.0*(h*Band.f)**2*n**2 \
```

```
                *Band.step))

        # add in recombination and detector noise to
        # compute total NEP at detector
        NEPtot = np.sqrt(NEPshot**2*(1.0 + kRecomb) + \
                NEPwave**2 + NEPdet**2)

        # compute NEP referenced to front of the system
        # and assign to column of NEPSys
        NEPsys = NEPtot/(etaSys*detFactor \
                *np.conj(FB.s[:,i,0])*FB.s[:,i,0])
        NEPSys[:,i-1] = NEPsys

# sum NEP of all channels (function of frequency)
NEPSysNet = 1.0/np.sqrt(np.sum(np.reciprocal(NEPSys)**2 \
    , axis=1))

# tuple of average NEP, NEP at each frequency, Qch,
# and number of channels
return np.mean(NEPSysNet), NEPSysNet, Qch, Nch
```